

VIDEO IMAGE TRANSMISSION VIA MOBILE SATELLITE CHANNELS

by

WENDY XIAOHONG WANG

A thesis submitted to the
Department of Electrical and Computer Engineering
in conformity with the requirements
for the degree of Master of Science (Engineering)

Queen's University
Kingston, Ontario, Canada
September 1995

Copyright © WENDY XIAOHONG WANG, 1995

Abstract

As the demand for wireless image transmission and videoconferencing continues to grow, low-bit-rate video compression that has robust behavior over lossy channels is of increasing interest. In this application, signal processing algorithm complexity is limited by the practical considerations of low-cost portable terminal equipment with low power consumption. This requires a comprehensive system design philosophy that jointly considers the source coding, channel coding, and modulation.

This thesis proposes two different systems for the transmission of low-bit-rate video over mobile satellite channels and tests each approach through detailed bit-level simulation and subjective picture quality assessment. The first approach utilizes concatenated coding of existing video source coding standards H.261 and H.263. System design includes trellis-coded modulation (TCM), inner and outer interleaving, forward error correction (FEC), as well as channel signal-to-noise ratio (SNR), bandwidth and delay requirements. In the first part of the thesis, concatenated channel coding is used to combat channel errors and lower the channel SNR requirement.

The second approach employs three-dimensional (3-D) subband coding. Subband coding, with pyramid vector quantization, is a form of joint source and channel coding, and eliminates the need for forward error correction and interleaving required by the H.261 and H.263 source coding standards. This simplifies system implementation and minimizes delay and channel error propagation.

Coherent modulation is used in the system design. In order to improve system performance, this thesis compares a variety of new and existing channel estimation algorithms in flat (frequency non-selective) fading that are needed for soft Viterbi

decoding. These algorithms are referred to as (1) symbol aided, (2) symbol aided and decision directed, (3) decision feedback and adaptive linear prediction, (4) Kalman filtering, and (5) multiple model. From system simulation results and an assessment of practical considerations, the symbol aided algorithm is found to be the preferred method for the shadowed mobile satellite channel.

In addition to the shadowed mobile satellite channel, the video transmission system is applied to other channels such as Rayleigh, Rician and two-ray frequency-selective channels. A new two-ray channel estimation algorithm is developed and evaluated for channel estimation in frequency selective fading.

Acknowledgements

I would like to thank my thesis supervisor Dr. Steven Blostein for his financial support, research advice, and superb supervision. Without Dr. Blostein's knowledgeable guidance and constructive suggestions, this research would not have been successfully completed. I am grateful to Mr. Mark Earnshaw who proofread my thesis, and taught me a lot about \LaTeX and Unix.

To my labmates and companions at graduate school, I wish to thank everyone for their friendship and support over the years. I will treasure my memories from Queen's for the rest of my life.

I would like to thank Joubin Karimi of Queen's University for providing the Viterbi decoder for the simulation.

The faculty and staff of the Department of Electrical Engineering are thanked for their help during my studies at Queen's University.

Finally, I would also like to express appreciation to my husband, my parents, and my parents-in-law for their help and continuous encouragement.

This work was supported by the Telecommunications Research Institute of Ontario and the School of Graduate Studies and Research at Queen's University.

Contents

Abstract	ii
Acknowledgements	iv
List of Tables	viii
List of Figures	ix
1 Introduction	1
1.1 Introduction	1
1.2 Summary of Contributions	2
1.3 Outline of the thesis	3
2 Background	4
2.1 Multipath Fading Channel Models	4
2.1.1 Introduction	4
2.1.2 Characterization of Multipath Fading	6
2.1.3 Channel Correlation Functions	9
2.1.4 Signalling Rate Considerations	14
2.2 Mobile Satellite and Terrestrial Channel Models	15
2.2.1 GEO Satellite Channel Model - Shadowed Rician Flat Fading	17
2.2.2 LEO/MEO Satellite Channel Model - Rician Flat Fading . . .	19
2.2.3 Cellular Mobile Channel Model 1 - Frequency Nonselective Rayleigh Fading	20

2.2.4	Cellular Mobile Channel Model 2 - Frequency Selective Rayleigh Fading	20
2.2.5	Simulation of Mobile Channels	21
2.3	Modulation and Coding for Satellite Channels	24
2.4	Low bitrate Video Compression	25
2.4.1	Hybrid source coding - H.261	25
2.4.2	Hybrid source coding - H.263	29
2.4.3	Subband source coding	31
2.4.4	Vector Quantization	32
2.5	Error correcting codes and interleaving	34
3	Design of a Video Coded Modem for Mobile Channels	37
3.1	Motivation for concatenated coding scheme	37
3.1.1	Source coding and channel coding	37
3.1.2	Concatenated channel coding	38
3.2	Design of channel estimator for flat fading	40
3.2.1	Symbol Aided algorithm	40
3.2.2	Symbol Aided plus Decision Directed algorithm	41
3.2.3	Decision Feedback and Adaptive Linear Prediction	43
3.2.4	Kalman filter	46
3.2.5	Multiple model algorithm	48
3.2.6	Conclusion	49
3.3	Interleaving	52
3.4	Design of inner code and inner interleaver	56
3.5	Design of Outer codes and outer interleaver	61
3.6	Results on Video Test Sequences	62
3.6.1	Simulation Parameters	62
3.6.2	Results and Discussion	62
3.6.3	Conclusion	67
3.7	Application of video transmission to other channels	77

3.7.1	Application to Rician channels	77
3.7.2	Application to Rayleigh channels	77
3.7.3	Application to 2-Ray frequency-selective Rayleigh fading channels	80
4	3-D Subband Video Transmission through Mobile Channels	94
4.1	Subband coding	94
4.1.1	Frequency spectrum of sample images	95
4.1.2	Analysis and Synthesis Filters	95
4.1.3	Optimum Bit Allocation For Frequency Bands	102
4.2	Pyramid Lattice Vector Quantizer (PVQ)	103
4.2.1	A Product Code PVQ	107
4.3	3-D Subband Coding Using PVQ	109
4.3.1	Introduction	109
4.3.2	3-D subband codec design	112
4.3.3	Results on video test sequences	113
4.3.4	Conclusions	116
5	Summary and Conclusions	119
5.1	Summary of Contributions	119
5.2	Suggestions for Further Research	121
	Bibliography	123
	Vita	128

List of Tables

2.1	Partial List of Satellite Frequency Allocations (Frequencies in GHz)	16
2.2	Shadowed Rician Model Parameters	18
2.3	CCITT Recommendation H.261 Video Coding Standard	26
3.1	Delay for different schemes	66
4.1	Example of 9-tap quadrature mirror filter coefficients	111
4.2	Optimal PR QMF filter coefficients based on energy compaction with zero mean high-pass filter	111
4.3	Example of integer coefficient PR QMF filter	111
4.4	PSNR performance using different filters	113
4.5	PSNR performance at 0.6bpp and 0.47bpp for subband coding and performance of H.263 average over the sequences	115

List of Figures

2.1	Wireless Mobile Satellite Channel	5
2.2	Multipath intensity profile	10
2.3	Doppler power spectrum	12
2.4	Relationships among the channel correlation functions and power spectra	13
2.5	Shadowed Rician Fading Simulator	21
2.6	Rician and Rayleigh Fading Simulator	22
2.7	Conceptual algorithm from the source encoder and decoder for the p64 system	28
2.8	A simplified Data Structure of the Video Multiplex Coder	30
3.1	The DFALP algorithm for tracking phase and amplitude of frequency nonselective fading channels	42
3.2	BER for SA, SADD, DFALP using Jake's Rician ($K=4$) fading model, a normalized fading bandwidth at 0.046, $k_t = 5$ using uncoded QPSK modulation.	45
3.3	BER for SA, SADD, DFALP, Kalman filtering, multiple model algorithm in light shadowed Rician fading, normalized fading bandwidth at 0.05, pilot symbol rate at 5, uncoded QPSK modulation.	50
3.4	BER for SA, SADD, DFALP, Kalman filtering, multiple model algorithm in average shadowed Rician fading, normalized fading bandwidth at 0.05, pilot symbol rate at 5, uncoded QPSK modulation.	51
3.5	System Block Diagram	53

3.6	Concept of convolutional interleaving	54
3.7	Concept of block interleaving	55
3.8	Set partition of an 8-PSK constellation	57
3.9	8-state 8-PSK TCM encoder	58
3.10	Bits to symbol mapping rule for 8-state 8-PSK TCM	58
3.11	Trellis diagram and minimum distance error event for an 8-state 8-PSK TCM	60
3.12	Inner TCM code performance for 24 kbit/s and 64 kbit/s video, nor- malized fading bandwidth at 0.0154 and 0.0057 respectively, pilot sym- bol rate k_t at 10.	63
3.13	System performance for 24 kbit/s video, normalized fading bandwidth at 0.0154, pilot symbol rate k_t at 10.	64
3.14	System performance for 64 kbit/s video, normalized fading bandwidth at 0.0057, pilot symbol rate k_t at 10.	65
3.15	Transmitted video through average shadowed mobile satellite channel, channel SNR=10.0dB, RS & TCM coding, one of 200 error frames in a total 15000 video frames	66
3.16	Original Miss America at 9.1 Mbits/sec showing frames 117, 126, 135, and 144 from top left to bottom right.	68
3.17	H.263 compressed Miss America at 24 kbits/sec, showing frames 117, 126, 135, and 144 from top left to bottom right.	69
3.18	H.263 compressed Miss America at 24 kbits/sec in average shadowed fading channel, 10 dB SNR, 15 kBd, 145 msec delay, showing frames 117, 126, 135, and 144 from top left to bottom right.	70
3.19	Original Salesman at 9.1 Mbits/sec, showing frames 108, 116, 124, and 132 from top left to bottom right.	71
3.20	H.263 compressed Salesman at 24 kbits/sec, showing frames 108, 116, 124, and 132 from top left to bottom right.	72

3.21	H.263 compressed Salesman at 24 kbits/sec in average shadowed fading channel, 10 dB SNR, 15 kBd, 145 msec delay, showing frames 108, 116, 124, and 132 from top left to bottom right.	73
3.22	Original Susie at 9.1 Mbits/sec, showing frames 108, 120, 132, and 144 from top left to bottom right	74
3.23	H.263 compressed Susie at 24 kbits/sec, showing frames 108, 120, 132, and 144 from top left to bottom right	75
3.24	H.263 compressed Susie at 24 kbits/sec in average shadowed fading channel, 10 dB SNR, 15 kBd, 145 msec delay, showing frames 108, 120, 132, and 144 from top left to bottom right	76
3.25	Inner TCM code performance for 24 kbit/s and 64 kbit/s video over a Rician channel, K=10 dB, normalized fading bandwidth at 0.0154 and 0.0057 respectively, pilot symbol rate k_t at 10.	78
3.26	Inner TCM code performance for 24 kbit/s and 64 kbit/s video over a Rayleigh channel, normalized fading bandwidth at 0.0154 and 0.0057 respectively, pilot symbol rate k_t at 10.	79
3.27	Tapped delay line model for frequency-selective fading channel	80
3.28	Uncoded QPSK performance for 24kbit/s and 64kbit/s video over two-ray Rayleigh frequency-selective fading channel, perfect channel state information	83
3.29	Uncoded QPSK performance for 24kbit/s and 64kbit/s video over two-ray Rayleigh frequency-selective fading channel, pilot channel state estimation	84
3.30	Coded TCM performance for 24 kbit/s and 64 kbit/s video over two-ray Rayleigh frequency-selective fading channel, perfect channel state information	85
3.31	Coded TCM performance for 24 kbit/s and 64 kbit/s video over two-ray Rayleigh frequency-selective fading channel, pilot channel state estimation	86

3.32	Uncoded QPSK performance for 24 kbit/s and 64 kbit/s video over two-ray Rayleigh frequency-selective fading channel with perfect channel state information and with pilot channel state estimation	87
3.33	Coded TCM performance for 24kbit/s and 64kbit/s video over two-ray Rayleigh frequency-selective fading channel with perfect channel state information and with pilot channel state estimation	88
3.34	Uncoded QPSK and coded TCM performance for 24kbit/s and 64kbit/s video over two-ray Rayleigh frequency-selective fading channel with perfect channel state information	89
3.35	Uncoded QPSK and coded TCM performance for 24kbit/s and 64kbit/s video over two-ray Rayleigh frequency-selective fading channel with pilot channel state estimation	90
3.36	Two-ray receiver (Uncoded QPSK) and one-ray receiver (coded TCM with interleaving) performance over two-ray Rayleigh frequency-selective fading channel with pilot channel state estimation	92
3.37	Two-ray receiver (Uncoded QPSK) and one-ray receiver (Uncoded QPSK without interleaving) performance over two-ray Rayleigh frequency-selective fading channel with pilot channel state estimation	93
4.1	Original images (a) Lenna (b) Susie	95
4.2	Frequency spectra of sample images (a) Lenna (b) Susie. Notice the lowpass nature of the spectra.	96
4.3	(a) Quadrature Mirror Filter (b) Subband Analysis and Synthesis Filterbanks	97
4.4	3-D subband analysis tree	98
4.5	3-D subband synthesis tree	99
4.6	Multilevel subbands	99
4.7	Integer lattice points on a 3-D pyramid of “radius” $K=4$	106
4.8	The distribution of information in the product enumerated PVQ index	108
4.9	System block diagram for 3-dimensional subband scheme	110

4.10	Temporal and Spatial Subband Decomposition	114
4.11	Original (left) and 2-D subband PVQ coded Mark at 0.6 bpp (right), PSNR=31.3 dB, recovered from average shadowed mobile satellite chan- nel, channel SNR=10.5 dB, BER= 10^{-3}	117
4.12	3-D subband PVQ coding video sequences at PSNR=32.2 dB, 0.6 bpp, recovered from average shadowed mobile satellite channel during deep fading, channel SNR=10.5 dB, BER= 10^{-3}	118

Chapter 1

Introduction

1.1 Introduction

The near future will witness the integration of computation and communication in the form of highly intelligent portable multi-media communicators. These devices will be well-endowed with computing power, memory and networking facilities, and will serve business as well as individuals worldwide. As a result, users will not be tethered to a single physical location. There are still many competing visions of how these portable devices and services will evolve and integrate in the next few years. A common theme is that users may want a multimedia terminal, capable of wireless access to a global network which can transport communications, video, and databases to the user in an on-demand, interactive fashion. Some elements of the system, such as portable personal computers or personal mobile radio voice and data communicators are already commercially available. Visual services such as video-on-demand will drastically increase the load on the networks. The rapid adoption of the newly created compression standards such as JPEG, MPEG, H.261 and H.263 reflect the current demand for data compression. The forthcoming multimedia world will transform telephones into multimedia terminals. The 1995 specification of the first international standard for bit-rate video below 64 kbits/s, the new H.263 standard, allows transmission of reasonable quality motion pictures through the existing telephone network and, hence, is an important step into this future. As these new services become

available, the demand of multimedia services through mobile systems will increase. The technology for these services is available but suitable standards have yet to be defined. This is due to the nature of mobile radio channels which are more limited in terms of bandwidth and bit error rates as compared to the public telephone network. Therefore new, robust and highly efficient coding algorithms will be necessary.

This vision of a “wireless multimedia future” motivated us to investigate possible video schemes to transmit very low bit rate video. The following thesis suggests several video coding schemes for bit rates in the range of 24 kbits/s to 200 kbits/s, which are specially derived for the requirements of mobile channels. The performance and robustness are discussed and evaluated for different applications.

Our investigation focuses on a dual mode mobile terminal, which can switch to either a satellite channel or a terrestrial wireless channel. As a result, we consider several different channel models involved in our evaluation: shadowed Rician flat-fading, Rician flat-fading, Rayleigh flat-fading, and two-ray frequency selective Rayleigh fading. We will apply on-line channel state estimation specialized to these different channel models. The results are discussed in chapter 3 and chapter 4.

1.2 Summary of Contributions

This thesis makes the following contributions:

1. A novel system design is proposed for the transmission of video over mobile satellite communication channels including trellis coded modulation (TCM), interleaving, forward error correction (FEC), channel signal-to-noise ratio (SNR), bandwidth and delay requirements. In the process of the design, a bit-level simulation of the entire transceiver was produced, which is valuable for future researchers in this area.
2. A variety of new and existing channel estimation schemes in flat (frequency non-selective) fading are proposed and compared.

3. A new two ray algorithm for channel estimation in frequency selective fading is proposed and evaluated.
4. A new 3-D subband video codec that employs pyramid vector quantization is proposed, and its performance is compared to hybrid coding at low bit rates.

1.3 Outline of the thesis

The thesis is organized as follows. Background material on mobile channel models, video compression, modulation, and coding used for mobile channels is presented in Chapter 2. Chapter 3 describes the design of a video coded modem for mobile channels using standard video compression algorithms and concatenated inner/outer error correction codes. Five different fading channel estimation algorithms are introduced and applied to different channel models in this chapter. The video transmission system is also applied to Rayleigh, Rician and frequency selective channels. Chapter 4 discusses a new three-dimensional subband codec with lattice pyramid vector quantization coding to minimize system delay and system complexity. Finally, Chapter 5 summarizes the results and conclusions of the thesis and makes suggestions for future investigation.

Chapter 2

Background

2.1 Multipath Fading Channel Models

2.1.1 Introduction

The multipath fading channel is a harsh environment for reliable digital communications. To develop practical receiver structures with acceptable error rate performance over this channel, a fundamental understanding of the fading process is necessary. In this section, models frequently cited in the literature to describe the dynamics of multipath fading are reviewed.

The nature of the multipath fading channel is dynamic, with both short term and long term fluctuations in its propagation characteristics. Short term fading phenomena directly determine the received signal structure and distribution of error symbols within a transmitted message. Much investigation into these effects has led to sophisticated modelling and analytical tools which can be used to design practical receivers and choose suitable modulation schemes for digital signaling over these channels [19][34]. The models are statistical in nature and assume the statistics can be considered locally stationary over the transmission interval. The actual model parameters vary according to the long term propagation characteristics of the channel.

Long term fading effects represent changes in the actual structure and attenuation

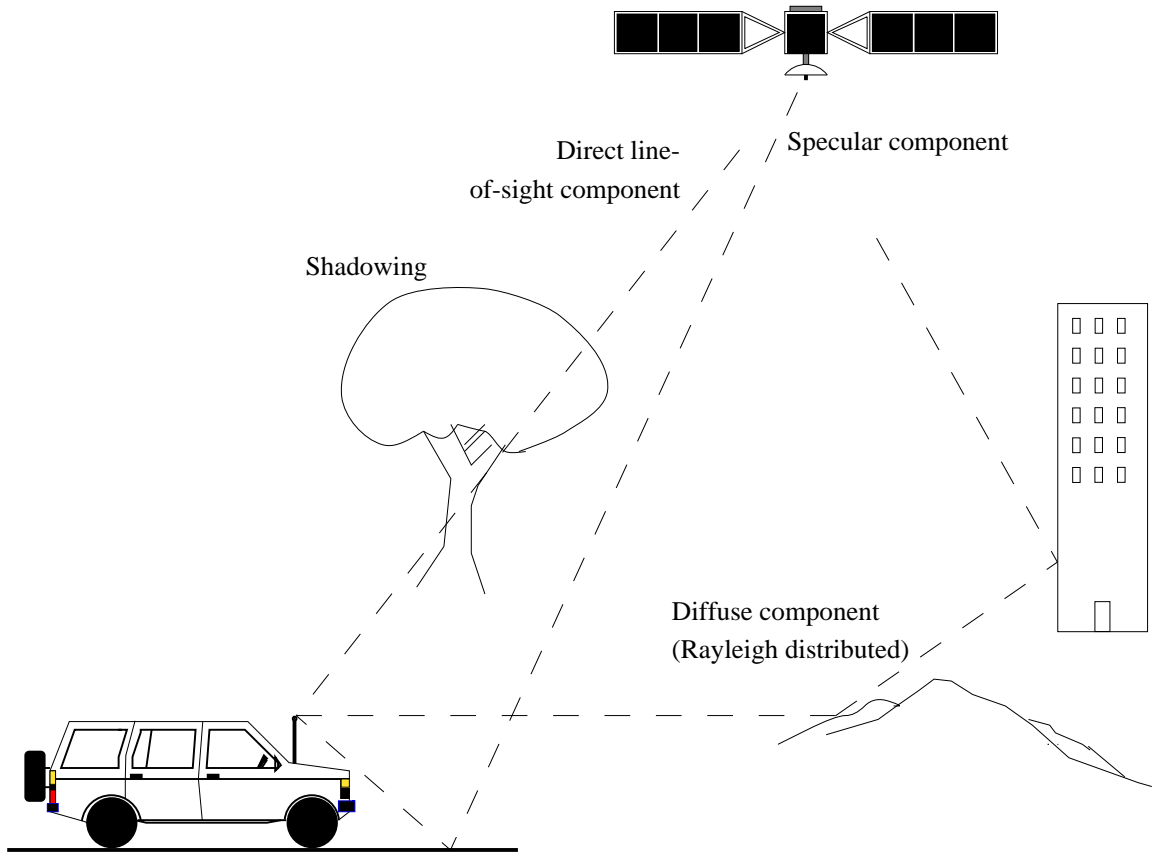


Figure 2.1: Wireless Mobile Satellite Channel

of the channel which occur naturally in daily, seasonal or annual cycles due to meteorological or solar influences. These effects determine the availability of the link over longer periods. Models for these effects are empirical in nature and usually arise from the accumulation of statistics over several long periods. These models are typically used only to choose the “worst-case” design parameters for the stationary short term channel model.

The typical scenario for wireless digital communications in a mobile satellite environment is depicted in Figure 2.1. The satellite or fixed base station antenna broadcasts the signal to the entire cell using an omnidirectional antenna. The transmitted signal is reflected, scattered and shadowed by the surrounding environment. Signal energy arrives at the mobile receiver antenna over several paths. Such a channel is

referred to as a multipath channel. The individual transmission paths exhibit different propagation delays and attenuation factors. Motion of the mobile and continuous physical changes in the medium lead to small changes in the path length. At carrier frequencies, these fluctuations can cause large phase changes in the received multipath components. The resulting constructive and destructive interference translates into large fluctuations in the received signal energy at the mobile. This phenomenon is referred to as multipath fading and is a result of the time-varying nature of the channel. Multipath fading can cause a severe performance impairment. Often sophisticated detection schemes must be employed to achieve an acceptable error rate performance.

2.1.2 Characterization of Multipath Fading

To determine a model for the multipath fading channel, consider the transmission of the bandpass signal $s(t)$ given by

$$s(t) = R\{u(t)e^{j2\pi f_c t}\}, \quad (2.1)$$

where $u(t)$ is the equivalent baseband signal and $R\{\cdot\}$ denotes the real part of a function of a complex-valued variable. Assume a multipath channel with n distinct components, each with attenuation factor $\alpha_n(t)$ and propagation delay $\tau_n(t)$. Both parameters vary with t to reflect the time-varying nature of the medium. At the mobile antenna, the received bandpass signal $x(t)$ is given by:

$$x(t) = \sum_n \alpha_n(t)s(t - \tau_n(t)) \quad (2.2)$$

Substitution for $s(t)$ from (2.1) into (2.2) gives:

$$x(t) = R\left\{\left(\sum_n \alpha_n(t)e^{-j2\pi f_c \tau_n(t)}u(t - \tau_n(t))\right)e^{j2\pi f_c t}\right\}. \quad (2.3)$$

From (2.3), the baseband equivalent received signal $r(t)$ is readily identified as:

$$r(t) = \sum_n \alpha_n(t)e^{-j2\pi f_c \tau_n(t)}u(t - \tau_n(t)). \quad (2.4)$$

The baseband signal $r(t)$ is the response of the channel to the baseband input signal $u(t)$. It follows that the baseband equivalent channel is characterized by the linear time-varying impulse response:

$$c(\tau; t) = \sum_n \alpha_n(t) e^{-2\pi f_c \tau_n(t)} \delta(\tau - \tau_n(t)) \quad (2.5)$$

The function $c(\tau; t)$ in (2.5) represents the complex baseband channel output at time t due to an impulse applied to the channel at time $t - \tau$.

The model for $c(\tau; t)$ in (2.5) represents a channel with discrete multipath components and is often used for modelling microwave line-of-sight and ionospheric skywave channels [37]. For wireless channels, the received signal can be modeled as being composed of a continuum of multipath components. Then, an integral formulation for the received bandpass signal $x(t)$ is required, given by:

$$x(t) = \int_{-\infty}^{+\infty} \alpha(t - \tau; t) s(t - \tau) d\tau \quad (2.6)$$

where $\alpha(t - \tau; t)$ represents the attenuation at time t of the signal components applied to the channel at time $t - \tau$. Inserting (2.1) for $s(t)$ in (2.6) gives:

$$x(t) = R \left\{ \left[\int_{-\infty}^{+\infty} \alpha(t - \tau; t) e^{-j2\pi f_c \tau} u(t - \tau) d\tau \right] e^{j2\pi f_c t} \right\} \quad (2.7)$$

From the convolution integral in (2.7), the baseband equivalent time-varying impulse response of the channel in this case is given by:

$$c(\tau; t) = \alpha(t - \tau; t) e^{-j2\pi f_c \tau} \quad (2.8)$$

The definition in (2.8) applies for channels which exhibit a continuum of multipath components.

A statistical model for multipath fading arises from considering the effect of the channel on an unmodulated carrier of frequency f_c . Consider the discrete multipath model. For a simple carrier the baseband signal is $u(t) = 1$, so the baseband received signal in (2.4) becomes:

$$\begin{aligned} r(t) &= \sum_n \alpha_n(t) e^{-j2\pi f_c \tau_n(t)} \\ &= \sum_n \alpha_n(t) e^{-j\theta_n(t)} \end{aligned} \quad (2.9)$$

where the phases of the received multipath components are given by $\theta_n(t) = 2\pi f_c \tau_n(t)$. In general, the path attenuation $\alpha_n(t)$ is largely unaffected by small variations in the medium; however, for relatively minor changes in the propagation delay $\tau_n(t)$, the phase $\theta_n(t)$ can change dramatically. Since the delays vary at different rates for each multipath, the phase for each delay path can be modeled as a random process. In fact, for a large number of paths Central Limit Theorem arguments imply that the phase is distributed uniformly on $[0, 2\pi)$ and the received signal $r(t)$ can be modeled as a complex-valued Gaussian random process. It follows that the time-varying impulse response $c(t - \tau; t)$ of the channel is also a complex Gaussian process in the time variable t .

Two models are frequently used in the literature to describe the distribution of the fading statistics. In the first model, the impulse response $c(\tau; t)$ is assumed to be a zero mean complex Gaussian process. In this case, the envelope $|c(\tau; t)|$ is Rayleigh distributed. This is the Rayleigh fading channel model that describes the most severe fading environment. The second type of fading occurs when a single nonfaded component, usually due to the presence of a fixed scatterer or line-of-sight signal component, is received along with the Rayleigh scattered components. In this case, the phase is no longer distributed uniformly but is somewhat localized around this non-faded component, so the impulse response $c(\tau; t)$ exhibits a non-zero mean. Its envelope $|c(\tau; t)|$ is now modeled using a Rician distribution and the resulting model is known as the Rician fading channel. Due to the presence of the non-faded component, signal degradation due to multipath fading is usually less severe for Rician channels than for their Rayleigh counterparts. For this reason, Rayleigh fading is generally considered to be a worst-case scenario. In this thesis, Rician, Rayleigh and shadowed Rician fading channel models are investigated. The two-ray Rayleigh fading channel model, which is an extension of the Rayleigh fading channel, is also considered.

Given the baseband impulse response $c(\tau; t)$, a time-varying baseband transfer function $C(f; t)$ of the channel can be defined. Using the Fourier transform, $C(f; t)$

is given by:

$$C(f; t) = \int_{-\infty}^{+\infty} c(\tau; t) e^{-j2\pi f\tau} d\tau \quad (2.10)$$

Again, because of the Central Limit Theorem, $C(f; t)$ is characterized as a complex Gaussian process as shown above.

2.1.3 Channel Correlation Functions

From the previous section, the distribution of the multipath components is complex Gaussian. We now describe the dynamics of the fading process. The dynamic behavior of the impulse response $c(\tau; t)$ is described by its correlation function or its power spectral density. In determining these functions, $c(\tau; t)$ is assumed to be wide-sense stationary (WSS). It follows that these functions model the effects of short-term fading only and ignore any long-term variations in the medium.

The autocorrelation function of the channel impulse response is defined by:

$$\phi_c(\tau_1, \tau_2; \Delta t) = E\{c(\tau_1; t)c^*(\tau_2; t + \Delta t)\} \quad (2.11)$$

where the expectation in (2.11) is over the time variable t . Note that the channel autocorrelation depends only on the time difference Δt due to the WSS assumption. For most wireless channels, the multipath component received along delay path τ_1 is uncorrelated with the one received along delay path τ_2 due to the large fluctuations in phase discussed earlier. This uncorrelated scattering (US) assumption leads to a simplification of the channel autocorrelation:

$$\phi_c(\tau_1, \tau_2; \Delta t) = \phi_c(\tau_1, \Delta t)\delta(\tau_1 - \tau_2) \quad (2.12)$$

At a specific observation time $\Delta t = 0$, the autocorrelation function $\phi_c(\tau; 0) \equiv \phi_c(\tau)$ gives the average power output of the channel at each propagation delay τ . For this reason, $\phi_c(\tau)$ is commonly referred to as the *multipath intensity profile* (MIP) or *delay power profile* (DPP) of the channel. An example of an exponential DPP is shown in Figure 2.2. Typically the DPP is non-zero only for a range of delay values less than

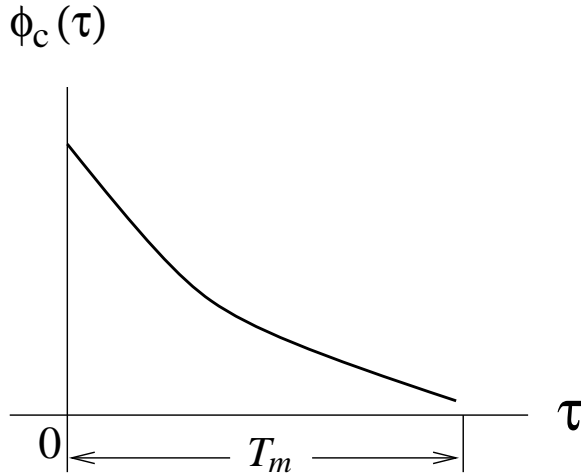


Figure 2.2: Multipath intensity profile

the *multipath spread* T_m of the channel; negligible power is received along delay paths larger than T_m .

The multipath spread parameter defines the time spread of the channel. As the signaling rate is increased, the symbol period T becomes shorter than T_m and significant energy from the current symbol period begins to “spill-over” into the next one causing inter-symbol interference (ISI). This ISI is time-varying due to channel effects, and must be accounted for in the receiver design. If ignored, ISI causes a severe performance impairment.

Since the transfer function $C(f;t)$ is also a complex-valued Gaussian process, a spaced-tone covariance can be defined as:

$$\phi_C(f_1, f_2; \Delta t) = E\{C(f_1; t)C^*(f_2; t + \Delta t)\} \quad (2.13)$$

Due to the WSS assumption, the covariance in (2.13) is only a function of the difference Δt in observation times. The previous assumption concerning uncorrelated scatterers translates to an equivalent WSS assumption in frequency: $\phi_C(f_1, f_2; \Delta t) \equiv \phi_C(\Delta f; \Delta t)$ only depends on the difference $\Delta f = f_2 - f_1$. For this reason, $\phi_C(\Delta f; \Delta t)$ is known as the *spaced-frequency spaced-time correlation function*. Its properties determine the nature of the fading distortion experienced at different signaling rates.

When $\Delta t = 0$ in (2.13), $\phi_C(\Delta f; 0)$ becomes the *spaced-frequency autocorrelation*

function $\phi_C(\Delta f)$. It can be readily shown that $\phi_C(\Delta f)$ and $\phi_c(\tau)$ are related via the Fourier transform:

$$\phi_C(\Delta f) = \int_{-\infty}^{+\infty} \phi_c(\tau) e^{-j2\pi\Delta f\tau} d\tau \quad (2.14)$$

The function $\phi_C(\Delta f)$ gives a measure of the frequency coherence of the channel. The range of frequencies over which the correlation is close to unity is referred to as the *coherence bandwidth* $F_m \sim 1/T_m$. Over this range, the individual frequencies all experience a similar multiplicative fading distortion. The channel acts as an all-pass filter as all signal components fade together [37]. This type of fading is known as *flat fading* or *frequency non-selective fading*. In terms of signaling rate, flat fading occurs for $T \gg T_m$. Conversely, over the bandwidth where $\phi_C(\Delta f)$ is small, individual frequencies each experience a fade that is different from and uncorrelated with the fades at other frequencies. As a result, the signal is severely distorted by the channel. This type of fading is called *frequency-selective fading* and occurs when $T \ll T_m$. The consequence of frequency-selectivity is ISI which must be dealt with by some sort of equalizer at the receiver.

The phenomenon that remains to be characterized is the time variation of the channel. The dynamics of the fading process can be modeled using a power spectral density that results from a transformation of the Δt variable in $\phi_C(\Delta f; \Delta t)$:

$$S_C(\Delta f; \lambda) = \int_{-\infty}^{+\infty} \phi_C(\Delta f; \Delta t) e^{-j2\pi\lambda\Delta t} d\Delta t \quad (2.15)$$

The time variations in the channel result in a spectral broadening of the transmitted signal. Setting $\Delta f = 0$ in (2.15) yields $S_C(\Delta f, \lambda) \equiv S_C(\lambda)$, the *Doppler power spectrum* of the channel which gives the extent of this broadening as a function of the Doppler frequency λ . Typically $S_C(\lambda)$ is non-zero over a finite range of frequencies B_D called the *Doppler spread* of the channel. Figure 2.3 shows a graph of a Doppler spectrum. The parameter B_D represents the maximum amount of frequency spread introduced by the channel. In mobile radio applications, B_D is calculated from the carrier frequency f_c and the vehicle speed V by [21]:

$$B_D = \frac{V \cdot f_c}{c} (\text{Hz}) \quad (2.16)$$

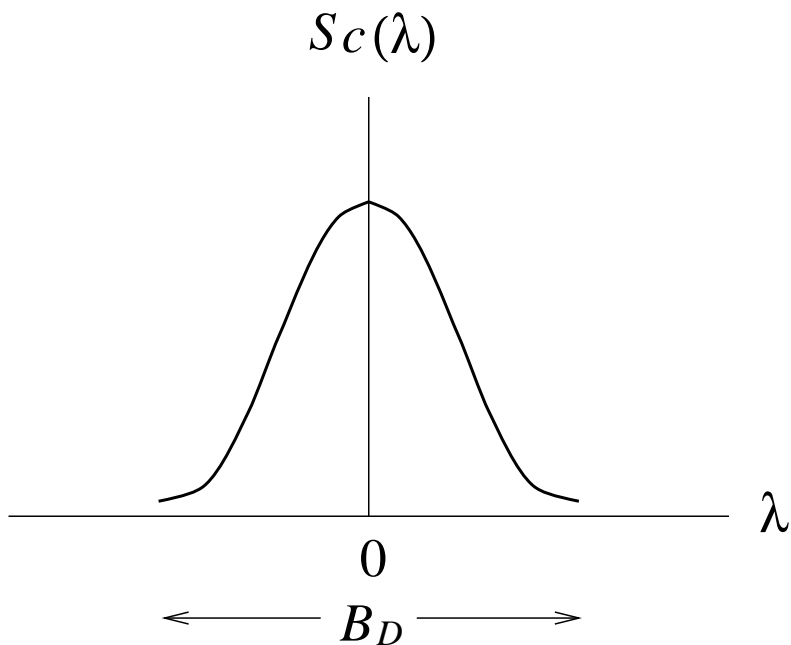


Figure 2.3: Doppler power spectrum

where c is the speed of light in free space. For large B_D , the channel introduces rapid time fluctuations in the signal due to the large spreading in frequency. For small spread values, the channel varies more slowly. These effects are described by the coherence time $T_D \sim 1/B_D$ of the channel.

Finally, the time dynamics of the channel expressed by the Δt variable in the correlation functions in (2.13) and (2.14) can also be expressed in terms of a power spectral density. Taking the Fourier transform of (2.13) with respect to Δt yields

$$S(\tau; \lambda) = \int_{-\infty}^{+\infty} \phi_c(\tau; \Delta t) e^{-j2\pi\lambda\Delta t} d\Delta t \quad (2.17)$$

The *scattering function* $S(\tau; \lambda)$ gives the average power at delay τ of all the scatterers that experience a Doppler shift of λ , and can be measured for several practical channels of interest [37]. In terms of $\phi_C(\Delta f; \Delta t)$, $S(\tau; \lambda)$ is given by the two-dimensional Fourier transform:

$$S(\tau; \lambda) = \int_{-\infty}^{+\infty} \int_{-\infty}^{+\infty} \phi_C(\Delta f; \Delta t) e^{-j2\pi\lambda\Delta t} e^{j2\pi\tau\Delta f} d\Delta t d\Delta f \quad (2.18)$$

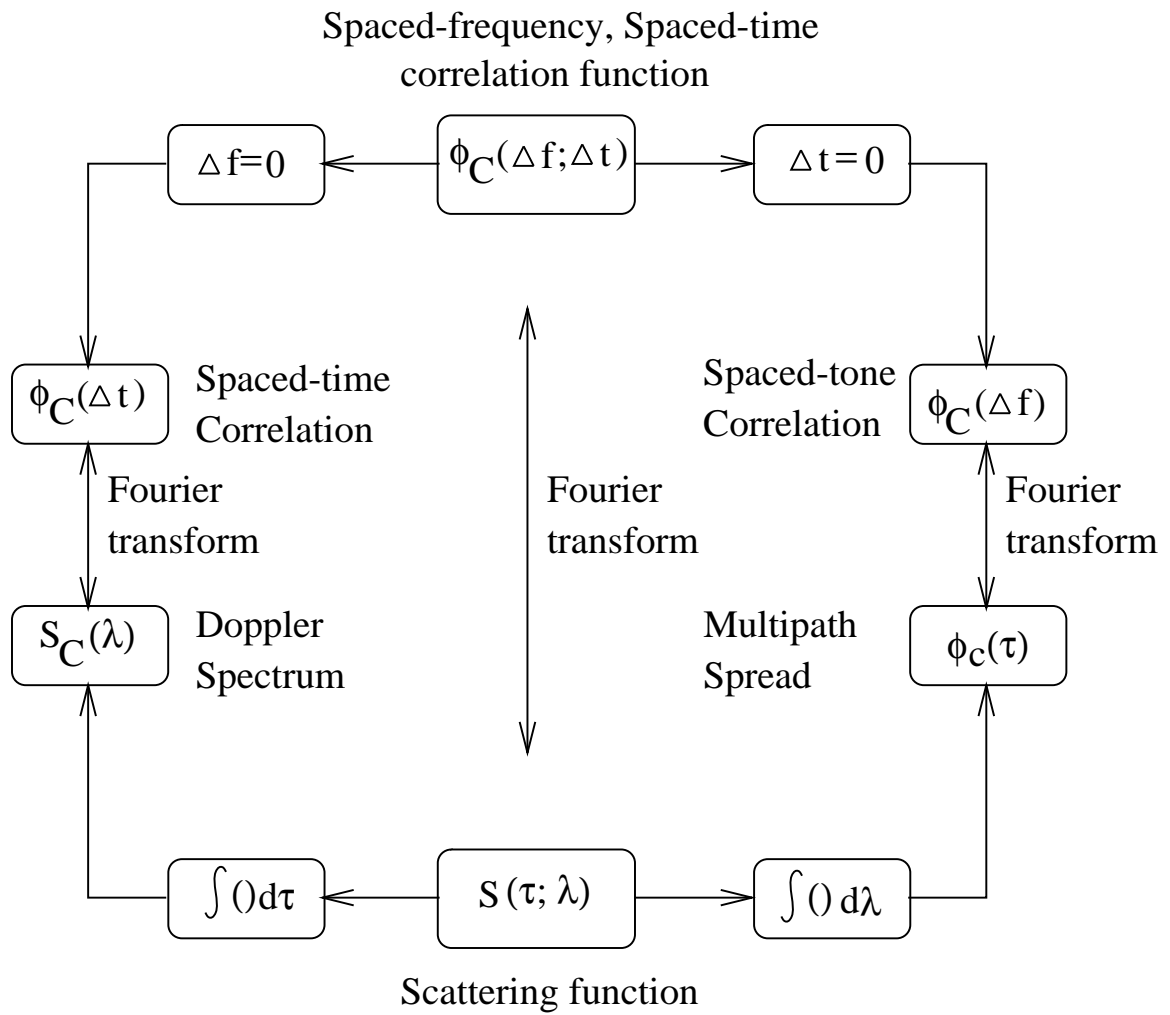


Figure 2.4: Relationships among the channel correlation functions and power spectra

The relationship between the various channel correlation functions and spectra are shown in Figure 2.4 [34]. Since $S(\tau; \lambda)$ and $\phi_C(\Delta f; \Delta t)$ are related through a two-dimensional Fourier transform, they convey equivalent statistical channel information.

2.1.4 Signalling Rate Considerations

The choice of channel model is influenced not only by the correlation and power spectrum of the channel, but also by the characteristics of the transmitted signal. For optimal coherent symbol-by-symbol detection, there must be no frequency selective distortion and no loss of time coherence over the duration of the signaling waveform. As shown previously, these two conditions are satisfied when:

$$T_m \ll T \ll \frac{1}{B_D} \quad (2.19)$$

To satisfy both inequalities in (2.19) simultaneously, the spread factor $T_m B_D$ must be $\ll 1$. For such an underspread channel, there is no ISI and the multiplicative fading distortion varies slowly enough that it can be tracked.

At higher signaling rates when the channel becomes overspread, frequency selective distortion produces severe ISI. In addition, channel coherence is lost by the time the signal waveform has propagated through the channel. In this case, equalization of ISI and tracking of the channel state become difficult problems due to these rapid fluctuations in the channel. Conventional approaches to adaptive equalization exhibit poor error-rate performance in this case. The receiver presented in Chapter 3 is designed to solve both the equalization and tracking problems with a single practical structure. Commonly, the following terminology is used to distinguish these cases:

frequency selective fading channel: $T \ll T_m$

frequency nonselective fading channel: $T \gg T_m$

fast fading channel: $T \gg \frac{1}{B_D}$

slow fading channel: $T \ll \frac{1}{B_D}$

2.2 Mobile Satellite and Terrestrial Channel Models

Satellites form an essential part of telecommunications systems worldwide, carrying large amounts of data and telephone traffic. Satellites offer a number of features not readily available with other means of communications. Because very large areas of the earth are visible from a satellite, it can form the star point of a communications net linking together many users simultaneously, users who may be widely separated geographically. The same feature enables satellites to provide communication links to remote communities. This is especially valuable for communities in sparsely populated areas that are difficult to access by other means.

There are several different kinds of satellite system: LEO (Low Earth Orbit), MEO (Medium Earth Orbit), HEO (Highly Elliptical Orbit) and GEO (Geostationary Orbit). The altitudes of these satellites above the earth are $<1,500$ km, 5,000 km to 13,000 km, 20,000 km to 35,786 km, and 35,786 km respectively.

One Mobile Satellite Service System currently in operation is the MSAT system, which is composed of geostationary satellites that provide mobile satellite service to the United States, Canada, and the Caribbean basin. The satellites operate near 1645 MHz (earth-to-space) and 1545 MHz (space-to-earth) for connection to and from the mobile terminals. *Ku*-band frequencies (11 and 13 GHz) are used for connections to and from the gateway stations, which provide the interface to the terrestrial telephone network. LEO systems include LEOSAT and STARNET, and will begin operation in 1995. The nonvoice, nongeostationary services are allocated frequencies 148-150.05 MHz (earth-to-space) and 137-148 MHz (space-to-earth) [48].

Some other satellite service systems (IRIDIUM, ODYSSEY, GLOBALSTAR) are proposed and planned to begin operation after 1997. Frequency allocations at 1600-1626.5 MHz (earth-to-space) and 2483.5-2500 MHz (space-to-earth) have been made to provide for mobile services. Table 2.1 shows a partial list of satellite frequency allocations.

Table 2.1: Partial List of Satellite Frequency Allocations (Frequencies in GHz)

Band	Uplink	Downlink	Satellite Service
VHF		0.137-0.138	Mobile
VHF	0.3120-0.315	0.387-0.390	Mobile
	0.8210-0.825	0.866-0.870	Mobile
	0.8450-0.851	0.890-0.896	Mobile
L-band	1.610-1.6138		Mobile, Radio Astronomy
	1.6138-1.6265	1.6138-1.6265	Mobile LEO
	1.6265-1.6605	1.525-1.535	Mobile
		1.575	Global Positioning System
		1.227	GPS
S-band	2.110-2.120	2.290-2.300	Deep-space research
		2.4835-2.500	Mobile
C-band	5.9-6.4	3.7-4.2	Fixed (FSS)
X-band	7.9-9.4	7.25-7.75	Military (U.S.)
Ku-band	14.0-14.5	11.7-12.2	FSS
		12.2-12.7	Direct Broadcast (BSS)
Ka-band	27-31	17-21	Unassigned
Q	50-51	40-41	Fixed
V		54-58 and 59-64	Intersatellite

The satellite system is intended to work with the existing public switched telephone network (PSTN). Calls are relayed through the satellite only when access cannot be made to the terrestrial network. The existing PSTN would be accessed via gateways and would be used for long distance connections including transoceanic calls.

The main difference between nongeostationary systems and the traditional geostationary systems is that, unlike the case of geostationary orbits, the relative geometry between a satellite and an earth station or among the satellites themselves is not fixed. This time-dependent geometry greatly increases the complexity of the system.

A significant problem with GEO satellites is propagation delay due to the great orbit distance which is 35,786 km. Thus, the one-way propagation delay, including the up-link and the down-link, is between 240 and 270 ms. The second fundamental problem with GEO is the lack of coverage at far northern and southern latitudes due to the equatorial orbit.

This section is organized as follows. Section 2.2.1 and 2.2.2 introduce GEO, LEO and MEO satellite channel models. Cellular mobile channel models are described in Sections 2.2.3 and 2.2.4. Finally, the fading channel simulator that uses a 3rd order Butterworth filter is presented in Section 2.2.5, which is used in most parts of this thesis. The Jakes fading model and high order FIR filter simulation methods are described briefly in Section 2.2.5.

2.2.1 GEO Satellite Channel Model - Shadowed Rician Flat Fading

Mobile satellite channels are distorted by multi-path fading, Doppler frequency shift, and attenuation of line-of-sight (LOS) from foliage. Rician and Shadowed Rician processes are used to mathematically model the distortion on the channel, which is often referred to simply as fading. This distortion is particularly severe in Canada where the angle between the LOS and the horizon is 15 - 20 degrees. The Rician process assumes a constant LOS, whereas in the shadowed Rician process the LOS

Table 2.2: Shadowed Rician Model Parameters

Parameter	Light	Average	Heavy
b_0	0.158	0.126	0.0631
μ_0	0.115	-0.115	-3.91
$\sqrt{d_0}$	0.115	0.161	0.806

is lognormally distributed. This model has been presented by Loo [26] and has been found to agree with measured data.

The shadowed Rician phasor can be expressed as:

$$r e^{j\phi} = u + v e^{j\varphi} \quad (2.20)$$

where u , the LOS, is lognormally distributed. The pdf of u is given as

$$p(u) = \frac{1}{u\sqrt{2\pi d_0}} e^{-(\ln u - \mu_0)^2 / 2d_0} \quad (2.21)$$

where μ_0 and d_0 are the mean and variance of u respectively. v is Rayleigh distributed, and φ is uniformly distributed between 0 and 2π . The average power of the scatter component, $v e^{j\varphi}$, is $2b_0$. The three parameters μ_0 , d_0 , b_0 , which uniquely characterize the shadowed Rician model, have been associated to the severity of the shadowing through studies from [25][26]. The parameters for three degrees of severity, light, average, and heavy shadowing, can be seen in Table 2.2. These results correspond to experimental values derived in [25][26]. Our investigation will concentrate on light and average shadowing indicative of a sparsely to medium forested area.

If u is temporarily kept constant in (2.20), the conditional distribution of r is:

$$p(r|u) = \frac{2r}{\alpha} e^{-(r^2+u^2)/\alpha} I_0\left(\frac{2ru}{\alpha}\right) \quad (2.22)$$

and the total probability of r is:

$$\begin{aligned} p(r) &= \int_0^{+\infty} p(r|u)p(u)du \\ &= \frac{2r}{\alpha\sqrt{2\pi d_0}} \int_0^{+\infty} \frac{1}{u} e^{-(\ln u - \mu_0)^2 / 2d_0 - (r^2+u^2)/\alpha} I_0\left(\frac{2ru}{\alpha}\right) du \end{aligned} \quad (2.23)$$

No exact expression has been found for the phase distribution $p(\phi)$ for the shadowed Rician process, but Loo has given the approximation:

$$p(\phi) \approx \frac{1}{\sigma\sqrt{2\pi}} e^{-(\phi-m_0)^2/2\sigma^2} \quad (2.24)$$

2.2.2 LEO/MEO Satellite Channel Model - Rician Flat Fading

We can express a Rician fading process with the following equation:

$$re^{j\phi} = a + ve^{j\varphi} \quad (2.25)$$

where a is a real constant representing the LOS, v is Rayleigh distributed, and φ is uniformly distributed between 0 and 2π . The real and imaginary components of the scatter component $ve^{j\varphi}$ have zero mean and variance $\alpha/2$, where α is the average power of the scatter component. The joint pdf of $p(r, \phi)$ is given by:

$$p(r, \phi) = \frac{r}{\pi\alpha} e^{-(r^2+a^2)/\alpha+(2ra\cos\phi)/\alpha} \quad (2.26)$$

The pdf of the amplitude can be obtained by applying the theorem of total probability:

$$p(r) = \frac{2r}{\alpha} e^{-(r^2+a^2)/\alpha} I_0\left(\frac{2ra}{\alpha}\right) \quad (2.27)$$

where $r \geq 0$ and I_0 is the modified Bessel function of the zeroth order.

Norton *et al.* originally defined the K-factor as:

$$K = \frac{\text{power in LOS}}{\text{power in scatter}} = \frac{a^2}{\alpha} \quad (2.28)$$

If we normalize $E[r^2]$ to 1, then the relations $a^2 = K/(K+1)$ and $\alpha = 1/(K+1)$ can be derived. In this manner the K-factor can be used to uniquely describe the Rician fading. We can further apply these relations to (2.27) yielding a more compact form of the pdf in terms of the K-factor:

$$p(r) = 2r(1+K)e^{-K-r^2(1+K)} I_0(2r\sqrt{K(1+K)}) \quad (2.29)$$

In a similar fashion the pdf of the phase is obtained as:

$$p(\phi) = \frac{1}{2\pi} e^{-K} [1 + G\sqrt{\pi} e^{G^2} (1 + \operatorname{erf}(G))] \quad (2.30)$$

where $G = \sqrt{K} \cos \phi$ and $0 \leq \phi \leq 2\pi$ and

$$\operatorname{erf}(x) = 1 - \frac{2}{\sqrt{\pi}} \int_x^\infty e^{-v^2} dv \quad (2.31)$$

2.2.3 Cellular Mobile Channel Model 1 - Frequency Nonselective Rayleigh Fading

When there is no direct signal to the receiver, that is, the constant a is zero for the Rician model, this turns out to be a Rayleigh fading model. The pdf's of the amplitude r and phase ϕ can be expressed as:

$$p_r(r) = \frac{2r}{\alpha} e^{-r^2/\alpha} \quad (2.32)$$

$$p_\phi(\phi) = \frac{1}{2\pi} \quad (2.33)$$

2.2.4 Cellular Mobile Channel Model 2 - Frequency Selective Rayleigh Fading

We now consider the symbol duration T to be not greater than the multipath spread T_m . This introduces a multiplicative, independent Rayleigh fading process on each delay path. This situation corresponds to the frequency selective fading. It is appropriate to represent the discrete time model of a frequency selective fading channel by a finite impulse response which can be represented by [34]:

$$c(\tau; t) = \sum_{j=0}^J c_j(t) \delta(\tau - \tau_j) \quad (2.34)$$

where the $c_j(t)$'s, the time-varying complex tap weights, are each a zero-mean complex Gaussian random process.

The length of the impulse response is determined by the multipath spread T_m . It has been found that the performance measures (bit error rate) depend on T_m , but

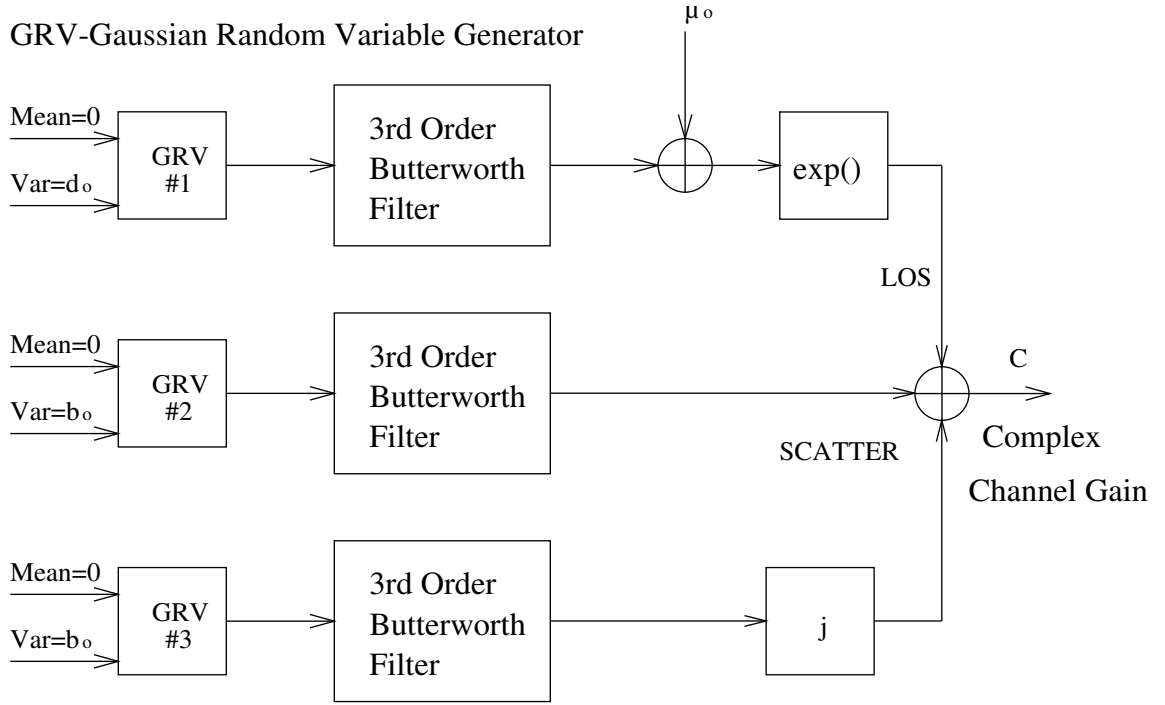


Figure 2.5: Shadowed Rician Fading Simulator

are generally not sensitive to the number of taps involved [5][37]. In this application, a two-tap delay line model is used, which leads to the two-beam fading channel [27]. In fact, a flat fading model is a special case of the delay line model with $J = 0$, as there is only one term in (2.34). The expression of the received signal $y(t)$ relates to the input signal $x(t)$ as:

$$y(t) = \sum_{j=0}^J x_j(t - \tau_j)c_j(t) + n(t) \quad (2.35)$$

where $n(t)$ is white Gaussian noise and $J + 1$ is the number of beams in the channel model.

2.2.5 Simulation of Mobile Channels

The mathematical model which best approximates the Canadian MSAT channel is the shadowed Rician model. It differs from the Rician model by having the LOS component undergo a lognormal transformation, whereas this amplitude is constant

GRV-Gaussian Random Variable Generator

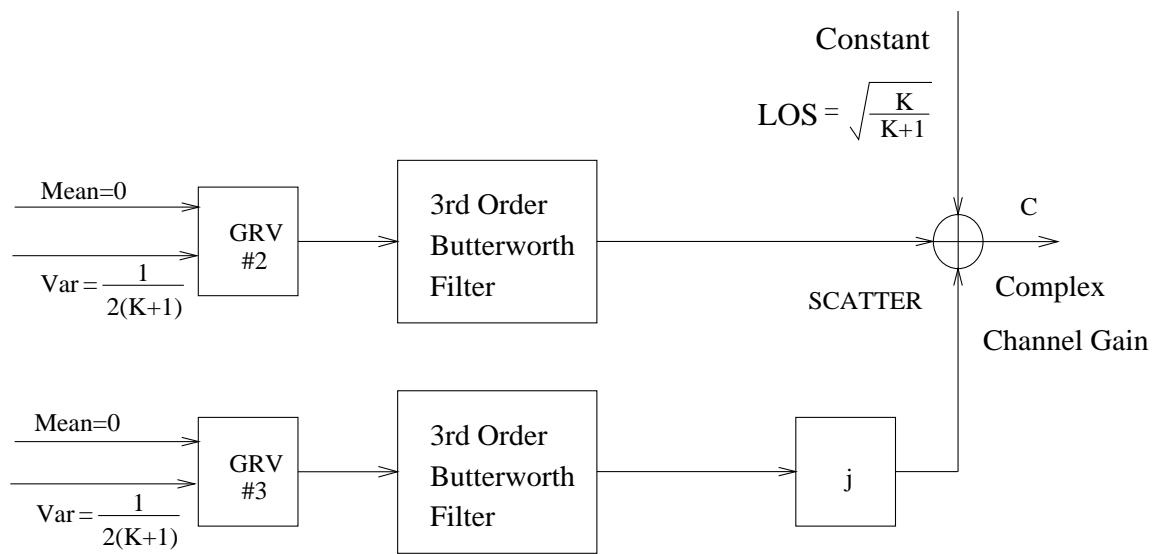


Figure 2.6: Rician and Rayleigh Fading Simulator

in the Rician model. The lognormal transformation accounts for foliage attenuation of the LOS which is more severe in Canada than in U.S. because of its more northerly latitude.

As in [18][10], third order Butterworth filters are used to simulate Rician, shadowed Rician, and Rayleigh dynamics. The cutoff frequency was set equal to the Doppler frequency due to vehicle motion and was normalized to the baud rate.

At time k , the received symbol y_k is related to the transmitted symbol x_k by:

$$y_k = c_k x_k + n_k \quad (2.36)$$

where c_k is the complex fading channel gain and n_k is complex additive white Gaussian noise. The random variables are generated by three independent random variable sequences. The 3dB cutoff frequency of the third-order Butterworth filters are equal to the normalized Doppler frequency f_0 . The filter transfer function of a third-order Butterworth filter is [31]:

$$|H(f)|^2 = \frac{3}{2\pi f_0} \frac{1}{1 + (\frac{f}{f_0})^6} \quad (2.37)$$

with

$$f_0 = \frac{B_D}{f_s} \quad (2.38)$$

where B_D is defined in (2.16), and f_s is symbol rate.

This filter spectrum has unit energy gain; that is, the total area under $|H(f)|^2$ is unity. Given the above fading spectrum, the output normalized autocorrelation is given by [31]:

$$\rho(\tau) = \frac{1}{2} [\exp(-2\vartheta) + \exp(-\vartheta)(\sqrt{3} \sin(\sqrt{3}\vartheta) + \cos(\sqrt{3}\vartheta))] \quad (2.39)$$

where $\vartheta = |\pi f_0 \tau|$. It can be shown that the complex channel gain in Figure 2.5 is:

$$\overline{|C|^2} = \exp(2\mu_0 + 2d_0) + 2b_0 \quad (2.40)$$

Thus, the channel gain is 2 dB for the light shadowing model. This factor will be adjusted in all signal-to-noise ratio calculations.

Figure 2.5 shows the shadowed Rician simulator. Figure 2.6 shows the Rician and Rayleigh fading simulator. In Figure 2.6, K is the K-factor of Rician fading, and K is 0 for Rayleigh fading.

Another widely-used Rician and Rayleigh channel model is the Jakes-Reudink fading channel [19] with channel autocorrelation function

$$r_n = r_0 J_0(2\pi f_0 n) = r_0 \frac{1}{2\pi} \int_{-\pi}^{\pi} e^{j2\pi f_0 n \sin \theta} d\theta \quad (2.41)$$

where $J_0()$ is the zeroth order Bessel function, f_0 is the normalized Doppler frequency. In this simulation, Gaussian random variables are passed through a FIR filter, with square root of channel power spectrum density as its transfer function. r_0 is the same as α in (2.28).

2.3 Modulation and Coding for Satellite Channels

The baseband modulation selected to operate over the mobile satellite channel is phase shift keying (PSK), which is bandwidth efficient while having a constant envelope. The constant envelope is desirable to allow travelling wave tube (TWT) amplifiers on the transponder to operate at the peak of their linear-region power output. Many studies have been carried out to determine the applicability of trellis-coded modulation (TCM) to shadowed Rician fading channel model [28][20][10]. Results show that trellis-coded modulation with soft Viterbi decoding can achieve a higher coding gain than equivalent bandwidth M-ary PSK.

It is well known that coherent detection of signals over fading channels is superior to non-coherent detection if accurate channel state information is available. To improve the performance of the system, it is necessary to track the phase and amplitude of the fading channel. Pilot symbol-aided techniques have been shown to be suitable for the transmission of digital signals over satellite mobile channels [30][8][18]. This thesis investigates five different algorithms to improve the system performance.

The issue of channel estimation will be discussed in Section 3.2.

2.4 Low bitrate Video Compression

2.4.1 Hybrid source coding - H.261

The H.261 standard was developed by the CCITT (International Telegraph and Telephone Consultative Committee) in December 1990 [9][23]. A slightly modified version of this recommendation was also adopted for use in North America [23]. H.261 is a coding specification for transmission of digital video sequences at $p \times 64$ kbit/s ($p=1,2,\dots,30$). The intended applications of this international standard are video-phone and videoconferencing services using the Integrated Services Digital Network (ISDN). The H.261 specification is already implemented in several telecommunication devices and is being integrated onto custom chips by several manufacturers. Its aim is two-way telecommunication at a rate as low as 64 kbit/s and with minimum delay. It is different from MPEG and JPEG. MPEG is defined for higher bit rates (0.9 Mbit/s to 1.5 Mbit/s) and consequently for higher quality. On the other hand, JPEG is used to compress still images.

2.4.1.1 Video Format

The CCITT has adopted the Common Intermediate Format (CIF) and Quarter-CIF (QCIF) as the video formats for visual telephony. The parameters for these formats are listed in Table 2.3. The maximum frame rate for both formats is 30 frames per second with the provision that either 1, 2, or 3 frames may be dropped at an encoder between transmitted frames. The uncompressed bit rates for transmitting CIF and QCIF at 30 frames/sec are 36.5 and 9.12 Mbit/s respectively. A bit-rate reduction of approximately 47.5 to 1 is needed to transport colour video with no audio signal at 64 kbit/s.

A picture is composed of one luminance and two chrominance components in a ratio of 4:1:1. The CIF and QCIF are divided into a hierarchical block structure

Parameters for Video Formats			
	NTSC	CIF	QCIF
	(Lines/Frame)x(Pixels/Line)		
Luminance(Y)	352x240	352x288	176x144
Chrominance(C _B)	176x120	176x144	88x72
Chrominance(C _G)	176x120	176x144	88x72

Blocks within
Macroblock

Y ₁	Y ₂
Y ₃	Y ₄
U ₅	V ₆

Macroblocks within GOB

1	2	3	4	5	6	7	8	9	10	11
12	13	14	15	16	17	18	19	20	21	22
23	24	25	26	27	28	29	30	31	32	33

GOB within CIF

1	2
3	4
5	6
7	8
9	10
11	12

GOB within NTSC

1	2
3	4
5	6
7	8
9	10

GOB within QCIF

1
2
3

6 blocks within macroblock(4 8x8 Y, 1 8x8 U, 1 8x8V)

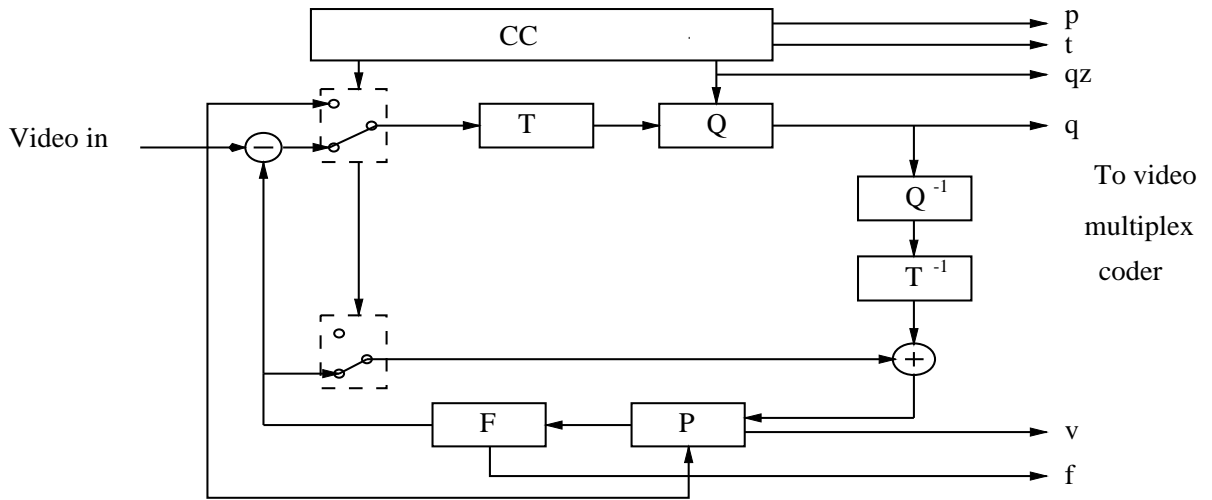
Table 2.3: CCITT Recommendation H.261 Video Coding Standard

consisting of Picture, Groups of Blocks (GOBs), Macro Blocks (MB), and Blocks. Each Macro Block is composed of four 8×8 luminance Blocks followed by two 8×8 chrominance Blocks. A Group of Blocks is composed of 3×11 Macro Blocks. A QCIF Picture has three GOBs, while a CIF Picture has twelve GOBs.

2.4.1.2 Video Coding Algorithm

Two major categories of source coding schemes are lossy coding and lossless coding. Lossy video source coding can be further divided into intraframe and interframe coding. Intraframe coding compresses video within a picture and removes only spatial redundancy. Interframe coding is for sequences of similar pictures. It reduces the temporal redundancy between pictures. Lossless coding achieves video compression by using statistical properties of the data. For example, H.261 uses lossless Huffman codes for entropy coding. H.261 is an hybrid source coding technique; that is, it uses interframe and intraframe coding to achieve a high compression ratio.

An H.261 encoder can be visualized as a serial transform and quantization structure with a feedback loop that models the decoder. The feed-back loop is required because the decoder reconstructs predicted images based on previously decoded images. Figure 2.7 illustrates the flow of 8×8 pixel blocks through an H.261 encoder. In intraframe mode, these blocks are fed directly into the forward DCT (Discrete Cosine Transform) and quantization sections to be encoded and sent to a video multiplex coder. They are also de-quantized, inverse-transformed, and stored in the picture memory for interframe coding. During the interframe coding mode, the prediction is based on motion estimation by comparing every Macro Block (luminance only) of the current frame with the Macro Blocks in the neighbourhood of the corresponding Macro Block in the previous frame. If the difference between the current and the predicted Macro Blocks is less than a certain threshold, motion compensation data is transformed for that Macro Block. Otherwise, the difference is DCT transformed, linearly quantized, and then sent to the video multiplex coder together with motion vector information. The video multiplex encoder has responsibility for calculating run



- | | |
|---|---------------------------------|
| T - Transform | p - Flag for INTRA/INTER |
| Q - Quantizer | t - Flag for transmitted or not |
| F - Loop filter | v - Motion vector |
| CC - Coding control | qz - Quantizer indication |
| f - Switching on/off of the loop filter | |
| q - Quantizing index for transform coefficients | |
| P - Picture memory with motion compensated variable delay | |

Figure 2.7: Conceptual algorithm from the source encoder and decoder for the p64 system

lengths and generating variable-length code symbols. Further details can be found in [9][23]. A simplified hierarchical structure with four layers of video data is shown in Figure 2.8.

2.4.2 Hybrid source coding - H.263

Based on H.261, H.263 was completed and approved by ITU's (International Telecommunication Union) expert group on very low bitrate visual telephony in April, 1995. H.263 is optimized and recommended for video coding for narrow telecommunication channels at $<64\text{bit/s}$ and QCIF format. As H.263 uses both integer pixel and half pixel motion estimation, the compressed video is less blocky compared to H.261 at very low bitrate. Another main difference between H.261 and H.263 is that H.263 uses four motion vectors per macroblock instead of one motion vector for H.261. Both H.261 and H.263 use forced updating to control the accumulation of inverse transform mismatch errors, a strategy that also prevents error propagation during the decoding of the interframe coded blocks. In forced updating, each Macro Block is coded in Intra mode at least once per 132 blocks of coefficients. There is a fast updating option [38]. H.263 also uses MPEG's notion of PB-frames mode to predict while H.261 only uses P frame mode to achieve high temporal compression. In MPEG, a complete image which is coded without reference to any other images is known as an *intrapicture* or *I frame*. An image that is coded relative to another image is called a *predicted* picture or *P frame*. Predicted frames can be generated relative to intraframes or other predicted frames. An image that is derived from *two* other images, one before and one after, is called a *bidirectional* picture or *B frame*. Bidirectional frames can be derived from intra or predicted frames but not other bidirectional frames. An arithmetic coding option for H.263 can achieve another 5% bitrate reduction over Huffman coding. In this thesis, a software implementation of H.263, available from Telenor Research [38], is used for experimental evaluation.

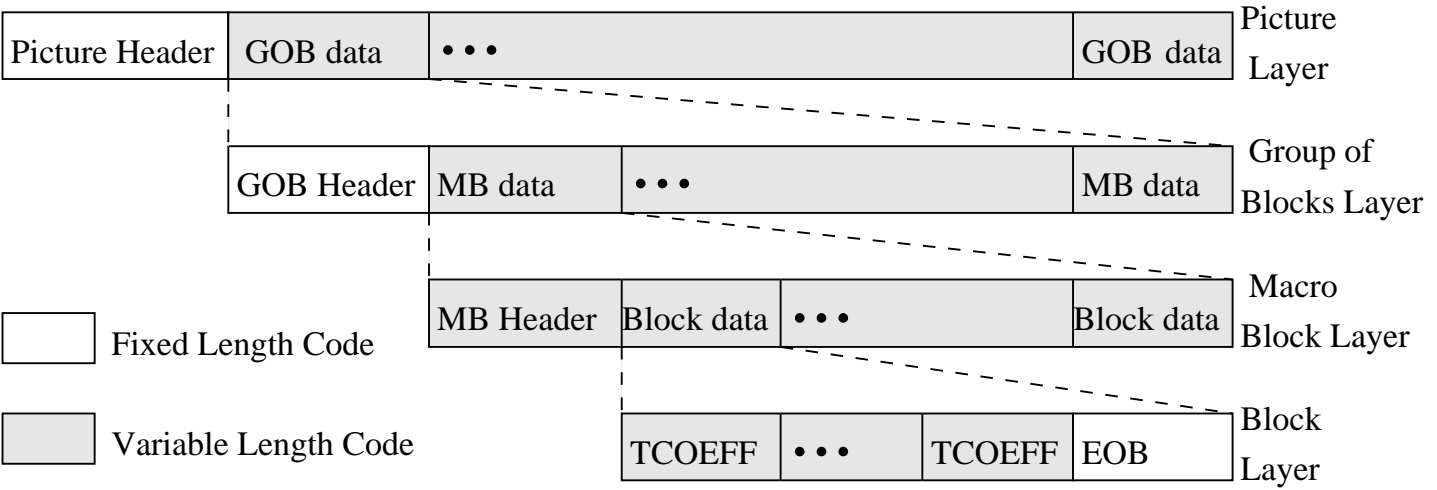


Figure 2.8: A simplified Data Structure of the Video Multiplex Coder

2.4.3 Subband source coding

In subband coding, the input video is treated as a multidimensional signal. The three-dimensional signals considered in this thesis come from the space (two-dimensional) and space-time (three-dimensional) data from the video. Subband coding divides the input signal into a number of separate frequency components and encodes each of these components separately [47]. This division into frequency components removes the redundancy in the input video and provides a set of uncorrelated inputs to the channel. The *frequency domain* coding techniques have the advantage that the number of bits used to encode each frequency component can be variable, so that the encoding accuracy is always placed where it is needed perceptually in the frequency domain. In fact, bands with little or no energy may not be encoded at all. The concept of subband coding of images consists of splitting up the frequency band of the image and then coding according to the statistics of this particular band. This means that the image is first split into subbands, which are then encoded, transmitted, and decoded. Finally, the reconstruction of the image takes place. The well-known quadrature mirror filter (QMF) is used to split the image into subbands.

Each subband can be encoded according to perceptual criteria that are specific to that band. Thus, information may be concentrated in the bands to which the human visual system is most sensitive. Some psychovisual properties of the human visual system are as follows: first, the eye's response to temporal stimuli is bimodal: it acts as an integrator at low frequencies and as a differentiator at high frequencies. Essentially, the transfer function for the human visual system is lowpass in both the temporal and spatial dimensions [32]. For this reason, dividing the video temporally increases efficiency; the signal may be divided into two or more temporal bands. High temporal subbands receive more quantization error than the corresponding low temporal components.

Furthermore, the human visual system has reduced acuity for detail at oblique orientations, while its response to vertical and horizontal edge detail (high-frequency information) is approximately equal. In addition, sensitivity to low-frequency spatial

information, where most of the energy in the signal is concentrated, is greater. In order to separate the energy in the image so that bit allocation may take advantage of the human visual system model, the image is divided into frequency subbands. By splitting the image into octave width separations in the frequency domain, energy content is successively separated into low and high frequency bands.

Encoding in subbands offers other advantages. By appropriately allocating the bits in different bands, the number of quantizer levels and hence reconstruction error variance can be separately controlled in each band, and the shape of the overall reconstruction error spectrum can be controlled as a function of frequency. In the lower frequency bands, a larger number of bits/sample can be used; whereas in upper frequency bands, fewer bits/sample can be used.

For some applications it is desirable that a low resolution version of a two-dimensional image become available quickly, and that higher resolutions become available as time goes on; this is known as progressive transmission. Subband image coding techniques can be modified to allow progressive transmission.

2.4.4 Vector Quantization

Quantization is a method for coding signals such that an approximate signal is constructed from a finite set of possible values. A given sample of the signal is specified by an index k into the finite set if it falls into the corresponding interval:

$$x_k < x < x_{k+1} \quad \text{where } k \in \{1, 2, \dots, N\} \quad (2.42)$$

The integer k is transmitted to the receiver to identify the particular value in the finite set that should be used to represent the signal's amplitude at that point. The value that k maps to is called the representative level, or reconstruction value, and the amplitudes x_k represent decision levels or thresholds. N denotes the number of elements in the finite set of reconstruction values. The mapping $y = Q(x)$, the quantizer characteristic, is a staircase-shaped function. A quantizer may be classified as either uniform or nonuniform. Uniform quantizers simply divide the domain into

equally spaced regions and usually use the mean of each region as the representative level; nonuniform quantizers, however, have variable-length representative level intervals which are functions of k . It should be noted that since the coded data is formed from a reduced set of values, irrecoverable information loss will occur.

Vector quantization expands the concepts employed in scalar quantization to the multidimensional case. A consequence of rate distortion theory is that a coder that better utilizes the redundancy in a set of data will yield a lower bit rate for a given distortion rate [16]. As a trivial example, consider a block of data consisting of all ones. Transmission of the data could be accomplished by sending each element separately, achieving a bit rate of 1 bit/sample. However, if the whole block is taken together and indexed to an identical block in a codebook, only the index need be transmitted; this would yield a bit rate of $1/xy$ bits/sample, where x is the horizontal size and y is the vertical size of the data. In general, a vector quantizer is a memoryless encoder since the mapping of input data to the output vectors is independent for each vector.

Using vector quantization, high compression ratios are possible with relatively small block sizes. Vector quantization is a mapping from an L -dimensional Euclidean space R^L to a finite subset of R^L . This finite set is called a vector quantization codebook or vector quantization table. By choosing the size of codebook, the transmission rate of a vector quantization coding process can be controlled. The objective is to select an optimal codebook of size N that results in the lowest possible distortion among all possible codebooks of the same size. $\log_2 N$ bits are needed to transmit the index i if fixed length coding is employed. The rate of an N element vector quantizer may be expressed as follows:

$$R = \frac{\log_2 N}{L} \text{bits/sample} \quad (2.43)$$

where L is the number of dimensions of the vector. An important feature of fixed-rate vector quantization is that fractional bit rates are achievable, unlike those achievable with scalar quantization.

The basis for quantization is grounded in the area of information theory. Data

compression, of which vector quantization is one type, attempts to reduce the bit rate by performing redundancy reduction. As such, vector quantization performs this reduction by focusing on four inter-related properties of vectors and signals:

- correlation
- nonlinear dependence
- probability density function (pdf) shape
- vector dimensionality

Vector quantization utilizes the above properties to determine appropriate placement of the vectors in the L -dimensional shape. There are two major groups of vector quantization codebook design methods. The first group of methods construct codebooks based on mathematical models. In this thesis, we use Pyramid Lattice Vector Quantization based on mathematical models in the first group. The second group designs the optimum (locally) codebook based on empirical data, which can achieve relatively small size codebooks but with more encoder and decoder complexity. One example from the second group is the LBG algorithm of Linde, Buzo, and Gray [16]. The LBG algorithm yields a minimum distortion quantizer for a given number of reproduction vectors, and thus the resulting code book is optimum for successive encoding with fixed code word length. The computation requirements for the LBG algorithm are large.

2.5 Error correcting codes and interleaving

The use of highly efficient video source encoding techniques greatly increases the need for near error-free communication. Transmission errors on wireless links such as satellite and terrestrial mobile radio are mainly caused by variations in received signal strength referred to as fading. To overcome severe power limitations due to fading and to satisfy bandwidth requirements, trellis-coded modulation (TCM) has been used.

TCM conserves bandwidth while achieving significant coding gains. There are some previous results showing that TCM is efficient for mobile satellite channels [18][10]. It should also be noted that on fading channels with TCM, errors tend to propagate during long fades or unreliable soft-decision information. An obvious alternative is to use powerful Reed-Solomon (RS) codes [22] with high rates, such as the standard NASA code (255, 223). Although RS codes perform very well on burst-error channels, their main drawback is that algebraic methods presently used for their decoding do not make full use of soft decision information. A possible solution is to apply coded modulation in a concatenated scheme with RS codes [7]. In this scheme the inner TCM codes work well in Gaussian noise, presenting to the outer code mostly residual burst errors which are ideally suited to RS codes. Error correcting codes combined with interleaving have been shown to be efficient in combating bursty errors [7]. This method aims to achieve both improved reliability and high efficiency in the use of communication resources in the presence of signal fading with acceptable coding complexity.

Because of the large block length of RS codes, interleaving generates large delays which are prohibitive for GEO satellite transmission. Another alternative is to use binary BCH codes [22] with different degrees of interleaving. The shorter length binary BCH codes involve less delay than the symbol-based RS codes. In this thesis, the results from these two schemes are compared. We show that significant coding gains relative to an uncoded system can be achieved with a small penalty in bandwidth by means of concatenated coding/modulation schemes.

Basically, a BCH code is described as follows:

For all positive integers $m \geq 3$ and $t < 2^{m-1}$ there exists a t -error correcting (n, k) BCH code C , with:

$$\text{length} \quad n = 2^m - 1 \tag{2.44}$$

$$\text{dimension} \quad k \geq n - mt \tag{2.45}$$

Note that the dimension k is the number of information bits that are protected by the code, and the number of check bits is $(n - k)$.

The best known nonbinary BCH codes are the *Reed-Solomon (RS) codes*. They are a popular class of codes for application in bursty error environments. A nonbinary block code consists of a set of fixed-length code words in which the elements of the code words are selected from an alphabet of q symbols, denoted as $0, 1, 2, \dots, q-1$. Usually, $q = 2^k$ so that k information bits are mapped into one of the q symbols. The length of the nonbinary code words is denoted as N and the number of information symbols encoded into a block of N symbols is denoted as K . The minimum distance of the nonbinary code is denoted as D_{min} . A systematic (N, K) block code consists of K information symbols and $N - K$ parity check symbols. The relationship of these parameters is [22]:

$$\begin{aligned}
 N &= q - 1 = 2^k - 1 \\
 K &= 1, 2, 3, \dots, N - 1 \\
 D_{min} &= N - K + 1 \\
 R_c &= \frac{K}{N}
 \end{aligned} \tag{2.46}$$

where R_c is the code rate. Such a RS code is guaranteed to correct up to:

$$\begin{aligned}
 t &= \left\lfloor \frac{D_{min} - 1}{2} \right\rfloor \\
 &= \left\lfloor \frac{N - K}{2} \right\rfloor
 \end{aligned} \tag{2.47}$$

symbol errors [22].

As the channel is subject to fading, an effective method for dealing with bursty error channels is to interleave the coded data in such a way that the bursty channel is transformed into a channel having independent errors. Two common structures are convolutional interleaving and block interleaving. They are chosen to minimize the system delay. Details governing the design of the interleaver are discussed in Chapter 3.

Chapter 3

Design of a Video Coded Modem for Mobile Channels

3.1 Motivation for concatenated coding scheme

3.1.1 Source coding and channel coding

As motivation, the source-channel coding theorem ([12], Theorem 8.13.1) which applies to any stationary source and for any discrete memoryless channel, states that the source code and channel codes can be designed separately and then concatenated to achieve optimal performance. That is, by integrating source and channel coding functions into a single mapping, overall coding performance will not be improved. There are two counter arguments to this approach. First, the theorem applies to sources and channels that are different from those encountered in our application. Second, from a practical viewpoint, joint source-channel coding could result in a decrease in system complexity, as will be shown in Chapter 4.

Unfortunately, a joint source-channel coding system is often inflexible with respect to different sources, channels, source coding techniques, and channel coding techniques. Wei [42] proposed an unequal error protection scheme for additive white Gaussian noise channels (AWGN) with a nonuniformly spaced signal constellation. In [42], the data from video source encoders are classified into different priority classes

and each class is treated differently. The unequal signal constellation scheme is not applicable for fading channels, because transmission of video over a radio-frequency (RF) link presents challenges that do not arise when a physical link such as a fiber optic cable or twisted pair is used. A “guaranteed channel” is often assumed when using a physical link, in which higher priority information experiences a much lower bit error rate than lower priority data. In an RF link that is subject to deep fades, all data is equally subject to loss. Secondly, when the source is highly compressed, the extra overhead in prioritizing the data streams becomes significant while channel errors are more catastrophic.

Because of this difference, layered coding for fault-tolerance is not effective in safeguarding high-priority data from loss. Alternatively, efficient forward error correction codes such as BCH and RS codes can be used to protect the transmitted video data. Another problem with unequal error protection is the lack of flexibility in allocating the proportion of high priority bits relative to lower priority bits. Thus, for the purposes of this Chapter, we are justified in considering separate source and channel coding.

It is always desirable to maintain communications in difficult situations, even though fewer messages can get across. For some point-to-point two-way communication links, this capability can be provided using a so-called Automatic Repeat Request (ARQ) method [22]. In this method, the receiver monitors the link condition. When that condition becomes unacceptable, the receiver sends a request to the transmitter, through its reverse link, to retransmit the data. This ARQ scheme will introduce delay. Because the delay of two-way transmission through geostationary mobile satellite channel (not including coding delay) is 250 ms, an ARQ scheme is not applicable here.

3.1.2 Concatenated channel coding

This chapter deals with transmitting ITU H.261 [9][23] and H.263 standard compressed moving images (< 64 kbits/sec) through shadowed mobile satellite channels.

The Canadian mobile satellite channel has been modeled as the sum of lognormal and Rayleigh components which is called shadowed Rician fading. The satellite channel is both power and bandwidth limited due to low mobile antenna gain and expensive transponder bandwidth allocation. Hybrid spatial/temporal video codecs such as H.261 and H.263 image codecs achieve high compression ratios to reduce the bandwidth occupancy. These codecs allow for a video stream communication at a rate as low as 24-64 kbit/s. However, these hybrid source codecs usually have high bit error sensitivities. Fading also severely degrades the digital signal transmission performance and a considerable amount of coding is needed to reduce the penalty in signal-to-noise ratio (SNR). Phase shift keying (PSK) is selected as the baseband modulation over the channel because it is bandwidth efficient and it has a constant envelope. The constant envelope is desirable for the mobile satellite channels to allow travelling wave tube (TWT) amplifiers on the transponder to operate at the peak of their linear-region power output. Many studies have been carried out to determine the applicability of trellis-coded modulation (TCM) to this channel model, some of them include [28][10]. Bit error rates of 10^{-3} to 10^{-4} at SNR in the range of 9-11 dB can be achieved. For video image transmission, much lower BER can be achieved by employing concatenated coding. Concatenated codes consisting of trellis inner codes and Reed-Solomon (or BCH) outer codes [7] are used to achieve large coding gains with small bandwidth expansion in the presence of frequency-nonselective Rician and Rayleigh fading channels. However, the results in [7] are limited to the case of perfect fading phase information. In this chapter, five different pilot-assisted fading tracking algorithms are tested and a computationally efficient pilot symbol-assisted algorithm is used to estimate fading channel state information. Monte Carlo simulations show that our 15 kBd and 40.5 kBd systems yield near error-free image transmission at average channel signal to noise ratio (E_b/N_0) between 9-12 dB over light-to-average shadowed Rician channels. The tradeoff between BER performance and delay due to interleaving is investigated.

3.2 Design of channel estimator for flat fading

It is well known that coherent detection of signals over fading channels is superior to non-coherent detection if accurate channel state information is available. To improve the performance of the system, it is necessary to track the phase and amplitude of the fading channel. Pilot symbol-aided techniques [30] have been shown to be suitable for the transmission of digital signals over satellite mobile channels [30][8][18]. Terrestrial Rician and Rayleigh fading models for dual-mode terminals are also investigated. Irvine and McLane developed a Symbol Aided and Decision Directed algorithm to estimate shadowed Rician fading channel gain [18]. Recently, Liu and Blostein [24] have developed an decision feedback and adaptive linear prediction (DFALP) algorithm to estimate the channel state information for the cases of Rayleigh and Rician fading channels without coding [24]. In this thesis, these algorithms and new algorithms involving Kalman filtering and multiple model methods are applied under the shadowed mobile satellite channel. Based on the testing results, one algorithm is chosen for the coded modulation and system simulation. The confidence in our BER simulation results is based on more than 200 bit errors [18] in each run of the Monte Carlo simulation, which corresponded to a 95% probability of the BER being within $\pm 20\%$ of its true value.

3.2.1 Symbol Aided algorithm

The symbol aided method (SA) sends symbols from the transmitter, which are known at the receiver, multiplexed with data symbols. The known pilot symbols are inserted every $k_t - 1$ data symbols. That is, one known symbol is sent out every $k_t - 1$ data symbols. Also, the pilot symbols are a pseudo-random sequence to avoid spectral harmonics at multiples of k_t/T . At the receiver, the known phase information of the pilot symbol is first rotated off from the output of the demodulator. After rotation, the residual phase, which has the information of the complex fading channel gain, is put through a front end filter to remove the white Gaussian noise. After the filter,

we have smoothed samples of the fading channel amplitude and phase information, spaced k_t symbols apart. The fading channel gain for the data symbols can be linearly interpolated between successive pairs of smoothed samples which are derived from the pilot symbols. If the delay for the front end filter is D_f , then the total delay to detect data symbols will be $k_t D_f$. The bandwidth expansion for this algorithm is a factor of $k_t/(k_t - 1)$. Using the Nyquist sampling theorem, the value of k_t is chosen according to:

$$k_t \leq \frac{1}{2 \times (\text{worst fading bandwidth})} \quad (3.1)$$

where worst fading bandwidth refers to the bandwidth that contains 98% power of the fading process spectrum.

3.2.2 Symbol Aided plus Decision Directed algorithm

To improve the Symbol Aided algorithm, Irvine and McLane proposed a Symbol Aided plus Decision Directed algorithm (SADD). The SADD algorithm is an extension of the SA phase tracker described in Section 3.2.1. An initial channel estimate from SA is used to make an initial decision on the received data symbols, which are in turn used to derive a decision-feedback channel estimate. A thresholding approach is then used to decide whether the decision-feedback estimate or interpolated estimate from the pilot symbols should be used. Finally, the estimated channel gain is passed through a second LPF to reduce the noise. A smoothed channel estimate is then obtained. The computational complexity of the algorithm is low compared to the Kalman filtering and multiple model approaches described in Sections 3.2.4 and 3.2.5, similar to the Decision Feedback and Adaptive Linear Prediction (DFALP) algorithm described in Section 3.2.3, but is higher than the SA algorithm. The total delay to estimate the fading channel gain is $(k_t + 1)D_f$.

There are two FIR filters used in the SADD algorithm. From simulations, we observe that SADD is very sensitive to the different windows for FIR filter and the bandwidth of these two filters. Basically, the filter bandwidth is chosen based on trial

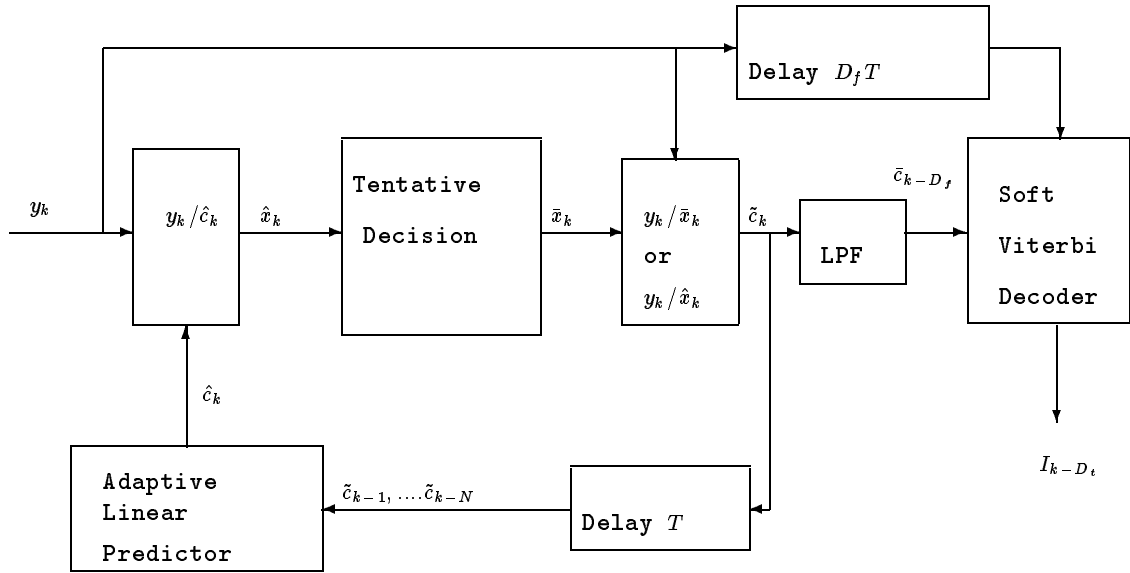


Figure 3.1: The DFALP algorithm for tracking phase and amplitude of frequency nonselective fading channels

and error. A mismatch of the filter bandwidth will result in a large degradation of bit-error-rate (BER) performance.

3.2.3 Decision Feedback and Adaptive Linear Prediction

The DFALP approach takes advantage of the time correlation of fading channels and uses tentative coherent detection and the least mean square (LMS) algorithm [44][45]. This allows for improved channel estimation during data transmission mode. To avoid run away mistrack, one training symbol is sent for every $k_t - 1$ data symbols. Figure 3.1 shows a block diagram for the DFALP algorithm, which is summarized by the following steps:

Repeat Steps 1-4:

- Step 1: If a training symbol x_k is available, set $\tilde{c}_k = y_k/x_k$.

Otherwise,

1.1 Predict channel gain: $\hat{c}_k = \sum_{i=1}^N b_i^* \tilde{c}_{k-i} = \vec{b}(k)^H \vec{c}(k)$

where H stands for Hermitian transpose;

1.2 Estimate data symbol: $\hat{x}_k = y_k/\hat{c}_k$;

1.3 Tentative decision: find \bar{x}_k such that $|\hat{x}_k - \bar{x}_k| = \min_{x_k \in D} |\hat{x}_k - x_k|$

D is the signal constellation of the modulated complex low-pass equivalent signal x_k ;

1.4 Correction:

If predicted gain agrees with decision feedback estimate, use the feedback estimate,

i.e., if $|\hat{c}_k - y_k/\bar{x}_k| < \beta$, then $\tilde{c}_k = y_k/\bar{x}_k$,

else use predicted gain only, i.e., if $|\hat{c}_k - y_k/\bar{x}_k| \geq \beta$, then $\tilde{c}_k = \hat{c}_k$;

- Step 2: Update linear predictor coefficients: $\vec{b}(k+1) = \vec{b}(k) + \mu(\tilde{c}_k - \hat{c}_k)^* \vec{c}(k)$
- Step 3: Low pass filter \tilde{c}_k : $\bar{c}_{k-D_f} = \sum_{i=0}^{2D_f} h_i \tilde{c}_{k-i}$
- Step 4: Output \bar{c}_{k-D_f} , increment k and go to Step 1.

The notations are:

\bar{c}_{k-D_f} = final (delayed) channel gain estimate

$\vec{b}(k) = (b_1, b_2, \dots, b_N)^T$ = filter coefficients at time kT

$\vec{c}(k) = (\tilde{c}_{k-1}, \tilde{c}_{k-1}, \dots, \tilde{c}_{k-N})^T$ = past corrected channel gain estimate

y_k = received signal plus noise at time kT

μ = step-size

\bar{x}_k = detected data symbol at time kT

β is the decision threshold

One training symbol is sent for transmitting every $k_t - 1$ data symbols.

The initial conditions for the filter coefficients \vec{b} are chosen to be:

$$\vec{b}(0) = (1, 0, \dots, 0)^T \quad (3.2)$$

The DFALP algorithm was first developed with uncoded coherent quadratic phase shift keying (QPSK) over Rician and Rayleigh channels using Jake's fading model [19]. Yong Liu [24] has provided the simulator of DFALP and Jake's fading model. The performance of the algorithm compares favorably with SADD [18] in terms of decision delay and bit-error-rate at high SNR under these coding and channel situations. Figure 3.2 shows results of a simulation comparing SA, SADD, DFALP for Rician fading ($K=4$). The number of bits used in the Monte Carlo simulation was 10^6 . Under the shadowed Rician fading model, however, DFALP performs worse than SA and SADD at low SNR, but outperforms SA and is close to SADD at high SNR.

On the other hand, the delay for DFALP is D_f , considerably lower than for SA or SADD. Another advantage of DFALP is lower sensitivity to parameters. For the SADD algorithm, performance is very sensitive to smoothing filter bandwidths and FIR filter windows. If there is any mismatch of these values, SADD's performance degrades significantly. In contrast, DFALP is less sensitive to mobile speed mismatch.

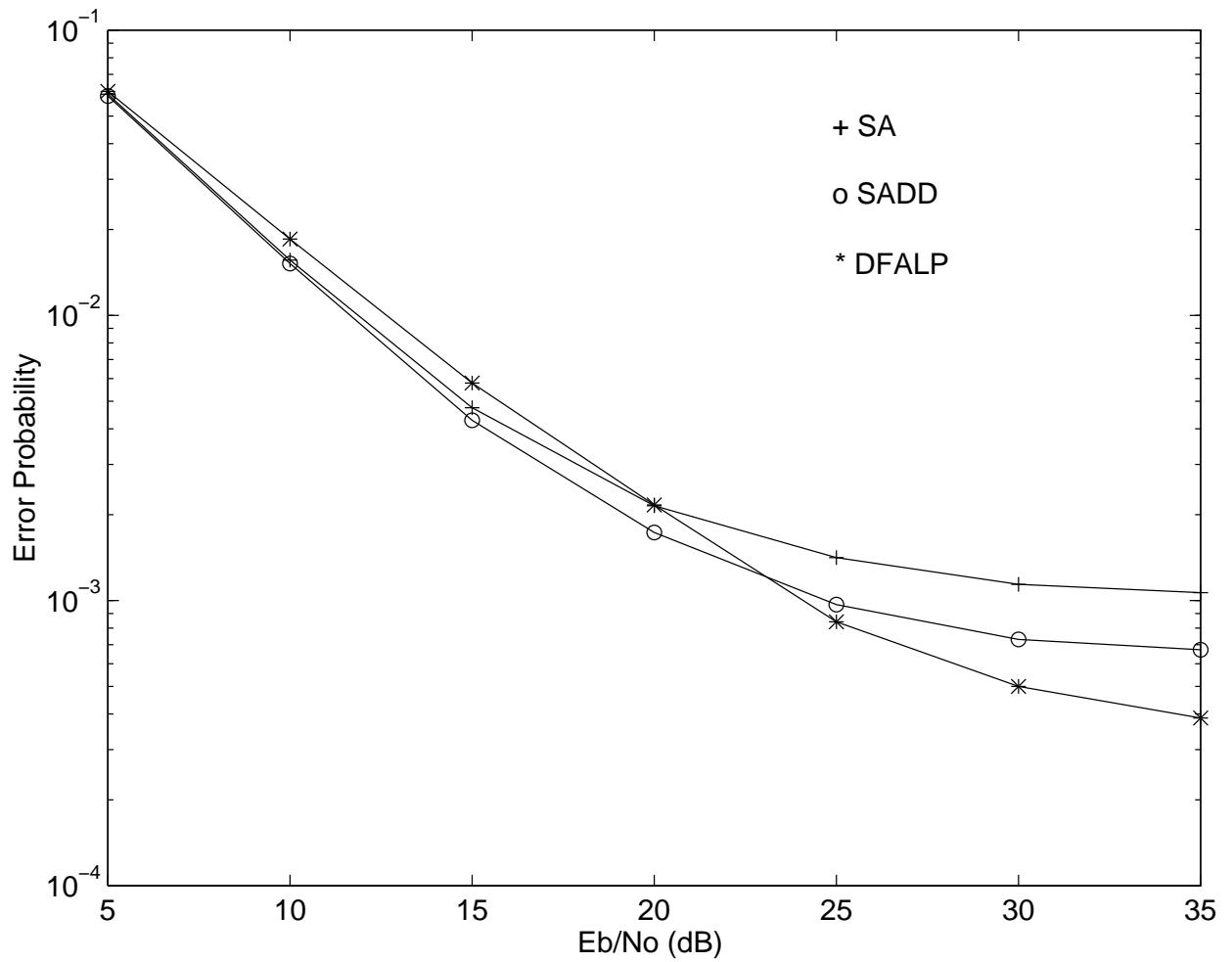


Figure 3.2: BER for SA, SADD, DFALP using Jake's Rician ($K=4$) fading model, a normalized fading bandwidth at 0.046, $k_t = 5$ using uncoded QPSK modulation.

3.2.4 Kalman filter

SADD and DFALP use thresholding results as decision feedback. The choice of a threshold value is based on empirical results. On the other hand, the following Kalman filter method optimally trades off the correlated complex channel model (a priori information) and received data [3]. A comparison between the Kalman filtering and hard thresholding of the SADD and DFALP algorithms is tested in this section.

The state equation of a flat fading process is

$$\underline{C}(k+1) = F(k)\underline{C}(k) + G(k)\underline{u}(k), \quad (3.3)$$

where $\underline{C}(k) = [c(k) \ c(k-1) \ \cdots \ c(k-N+1)]^T$ and $c(k)$ is the time-varying complex fading channel gain from shadowed Rician fading channels. The measurement equation is

$$\underline{Y}(k+1) = H(k+1)\underline{C}(k+1) + \underline{n}(k+1), \quad (3.4)$$

where $\underline{u}(k)$ and $\underline{n}(k)$ are white Gaussian noise, and $\underline{Y}(k+1)$ is the received signal vector at time t_{k+1} . The one-step prediction of the state at t_k is given by

$$\hat{\underline{C}}(k+1|k) = F(k)\hat{\underline{C}}(k|k) \quad (3.5)$$

State error covariance at t_k is $P(k|k)$, and the one-step state prediction covariance is

$$P(k+1|k) = F(k)P(k|k)F^T(k) + Q(k). \quad (3.6)$$

In QPSK, the measurement prediction equation at time t_k for symbol j , where $j \in \{1, 2, 3, 4\}$ is given by

$$\hat{\underline{Y}}_j(k+1|k) = H_j(k+1)\hat{\underline{C}}(k+1|k). \quad (3.7)$$

The innovation equation at time t_{k+1} is given by

$$\underline{v}_j(k+1) = \underline{Y}(k+1) - \hat{\underline{Y}}_j(k+1|k) \quad (3.8)$$

with innovation measurement prediction covariance

$$S_j(k+1) = H_j(k+1)P(k+1|k)H_j^T(k+1) + R(k+1). \quad (3.9)$$

where $R(k+1)$ is the covariance of $\underline{n}(k+1)$. The filter gain can be calculated via,

$$W_j(k+1) = P(k+1|k)H_j^T(k+1)S_j^{-1}(k+1) \quad (3.10)$$

and the covariance of the state at time t_{k+1} is

$$P_j(k+1|k+1) = P(k+1|k) - W_j(k+1)S_j(k+1)W_j^T(k+1), \quad (3.11)$$

and the updated state estimate is

$$\hat{\underline{C}}_j(k+1|k+1) = \hat{\underline{C}}(k+1|k) + W_j(k+1)\underline{v}_j(k+1) \quad (3.12)$$

where $H_j(k)$ is the output matrix for QPSK modulation symbol. The probability density function (pdf) of the innovation is Gaussian with mean 0 and variance $S_j(k+1)$. Let $p_j(k+1)$ denote the innovation pdf evaluated at $\underline{v}_j(k+1)$, i.e.,

$$p_j(k+1) = \mathcal{N}(\underline{v}_j(k+1); 0, S_j(k+1)) \quad (3.13)$$

For a symbol m such that $p_m(k+1) \geq p_j(k+1)$ for $j = 1, 2, 3, 4$, let

$$\hat{\underline{C}}(k+1|k+1) = \hat{\underline{C}}_m(k+1|k+1) \quad (3.14)$$

and

$$P(k+1|k+1) = P_m(k+1|k+1) \quad (3.15)$$

Using the method found in [13], we multiply both sides of equation (3.3) by $\underline{C}^T(k)$ and take expectations to yield:

$$E[\underline{C}(k+1)\underline{C}^T(k)] = FE[\underline{C}(k)\underline{C}^T(k)] + GE[\underline{u}(k)\underline{C}^T(k)] \quad (3.16)$$

From (3.16), the correlation coefficients of the complex channel gains are: $R_c(1) = E[\underline{C}(k+1)\underline{C}^T(k)]$, and $R_c(0) = E[\underline{C}(k)\underline{C}^T(k)]$. Therefore, from (3.16)

$$F = R_c(1)R_c^{-1}(0). \quad (3.17)$$

Multiplying the state-space equation by $\underline{C}^T(k+1)$ and taking expectations gives the remaining quantities needed:

$$E[\underline{C}(k+1)\underline{C}^T(k+1)] = FE[\underline{C}(k)\underline{C}^T(k+1)] + GE[\underline{u}(k)\underline{C}^T(k+1)]. \quad (3.18)$$

The above equation can be simplified as:

$$\begin{aligned} R_c(0) &= E[\underline{C}(k+1)\underline{C}^T(k+1)] \\ &= FR_c^T(1) + GE[\underline{u}(k)(F\underline{C}(k) + G\underline{u}(k))^T]. \end{aligned} \quad (3.19)$$

From the last equation, we may complete the calculation of the state prediction covariance matrix by noting that

$$Q(k) = GG^T = R_c(0) - FR_c^T(1) \quad (3.20)$$

We remark that equation (3.20) is slightly different from equation (A-7) in [13].

Figures 3.3 and 3.4 show the BER for the Kalman filtering algorithm in light and average shadowed Rician fading, normalized fading bandwidth at 0.05, pilot symbol rate at 5, and uncoded QPSK modulation.

3.2.5 Multiple model algorithm

As an alternative to making the hard decision of equations (3.14) and (3.15) in the previous section, a soft decision approach will now be described. The term “multiple model” [4] refers to recursively estimating the probability that each model is correct given the symbol probabilities. Based on the Kalman filter method described in Section 3.2.4 and using Bayes’ theorem, the posterior probability of model j being correct, given the measurement data up to time t_k , is obtained recursively as:

$$\mu_j(k+1) = \frac{p_j(k+1)\mu_j(k)}{\sum_{j=1}^4 p_j(k+1)\mu_j(k)} \quad (3.21)$$

where $j = 1, 2, 3, 4$. The finalized estimation of $\underline{C}(k+1)$ becomes:

$$\hat{\underline{C}}(k+1|k+1) = \sum_{j=1}^4 \mu_j(k+1)\hat{\underline{C}}_j(k+1|k+1) \quad (3.22)$$

and the covariance matrix estimate becomes:

$$\begin{aligned} P(k+1|k+1) &= \sum_{j=1}^4 \mu_j(k+1)\{P_j(k+1|k+1) + [\hat{\underline{C}}_j(k+1|k+1) \\ &\quad - \hat{\underline{C}}(k+1|k+1)] \times [\hat{\underline{C}}_j(k+1|k+1) - \hat{\underline{C}}(k+1|k+1)]^T\} \end{aligned} \quad (3.23)$$

In the simulation, a 6×6 F matrix (real and imaginary parts) is used to model the fading amplitude and phase. For a fair comparison between the five different algorithms, no Viterbi decoders are used in the Kalman filter and multiple model algorithms. The testing was under uncoded QPSK modulation, the normalized fading bandwidth was 0.05, and the pilot symbol rate k_t was 5. Figures 3.3 and 3.4 show BER comparison for SA, SADD, DFALP, Kalman filtering and multiple model algorithm over light and average shadowed Rician fading channels.

3.2.6 Conclusion

The test results in Figures 3.3 and 3.4 show that SADD performs the best out of these five algorithms. However, SADD has the highest delay $(k_t + 1)D_f$ and is also very sensitive to the front end filter and smoothing filter. The delays for SA and DFALP are $k_t D_f$ and D_f respectively. The Kalman filter and multiple model algorithms use one-step prediction; thus, they have no delay in estimating the complex channel gain but have the highest complexity. From Figures 3.3 and 3.4 we can see that Kalman filtering and the multiple model algorithm offer less improvement than the hard thresholding employed in the SADD and DFALP algorithms. The poorer performance of Kalman filtering with or without multiple model combining, can be attributed to the limited degree of filtering due to the single time-step delay constraint. Comparing the results of the Kalman filtering and multiple model algorithms, the multiple model algorithm is superior to Kalman filtering at low channel SNR, but inferior at high channel SNR. This can be explained by the fact that the multiple model algorithm permits the combination of low SNR estimates of channel state from different models. On the other hand, at high SNR, when channel estimation is much more accurate, there are unlikely to be channel bit errors, and the hard thresholding in SADD and DFALP permit direct noise reduction in the received signal, and therefore, in channel estimation.

At a channel SNR less than 15 dB under light and average shadowing, the performances of SA and SADD are very close, so we chose SA for our system simulation.

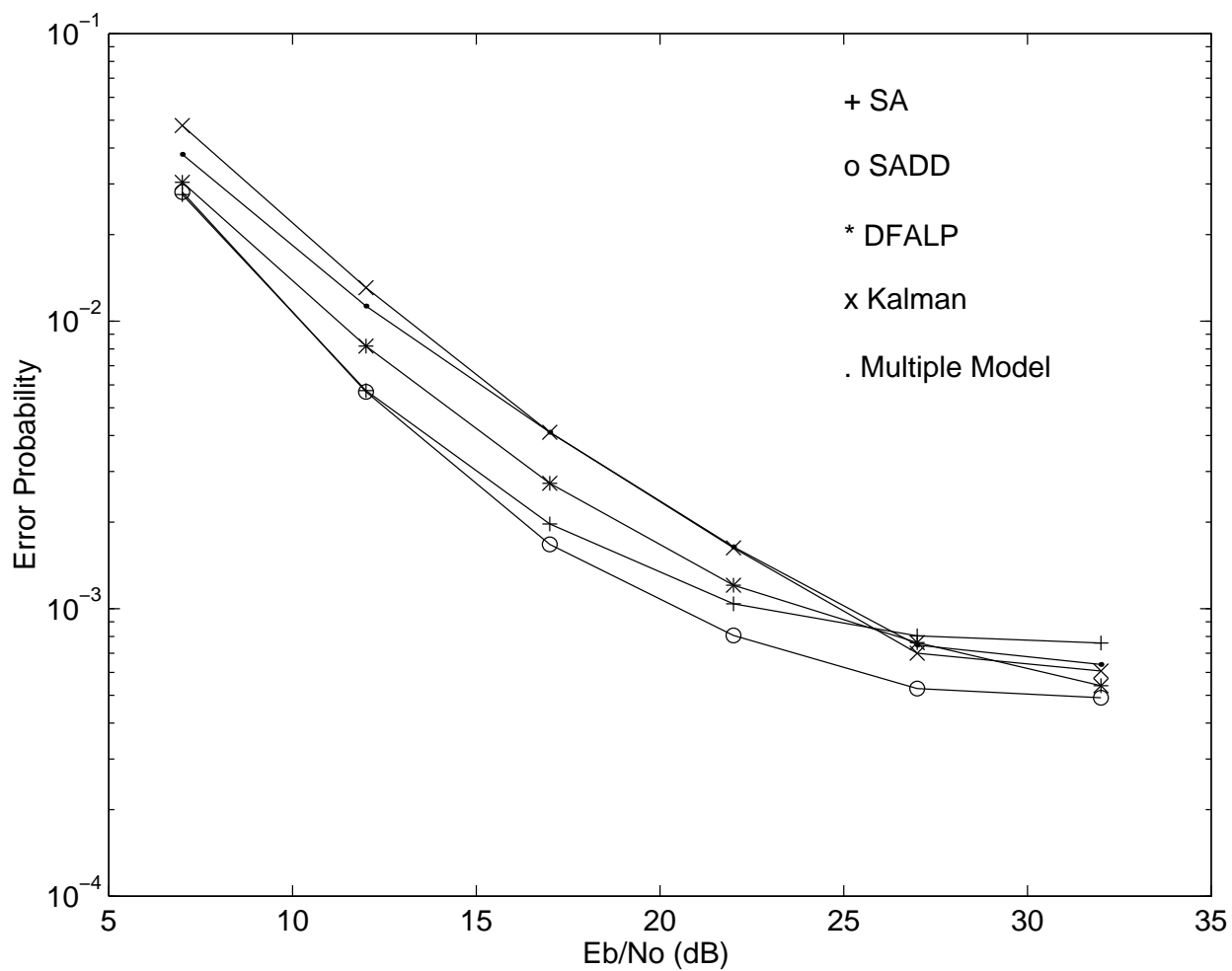


Figure 3.3: BER for SA, SADD, DFALP, Kalman filtering, multiple model algorithm in light shadowed Rician fading, normalized fading bandwidth at 0.05, pilot symbol rate at 5, uncoded QPSK modulation.

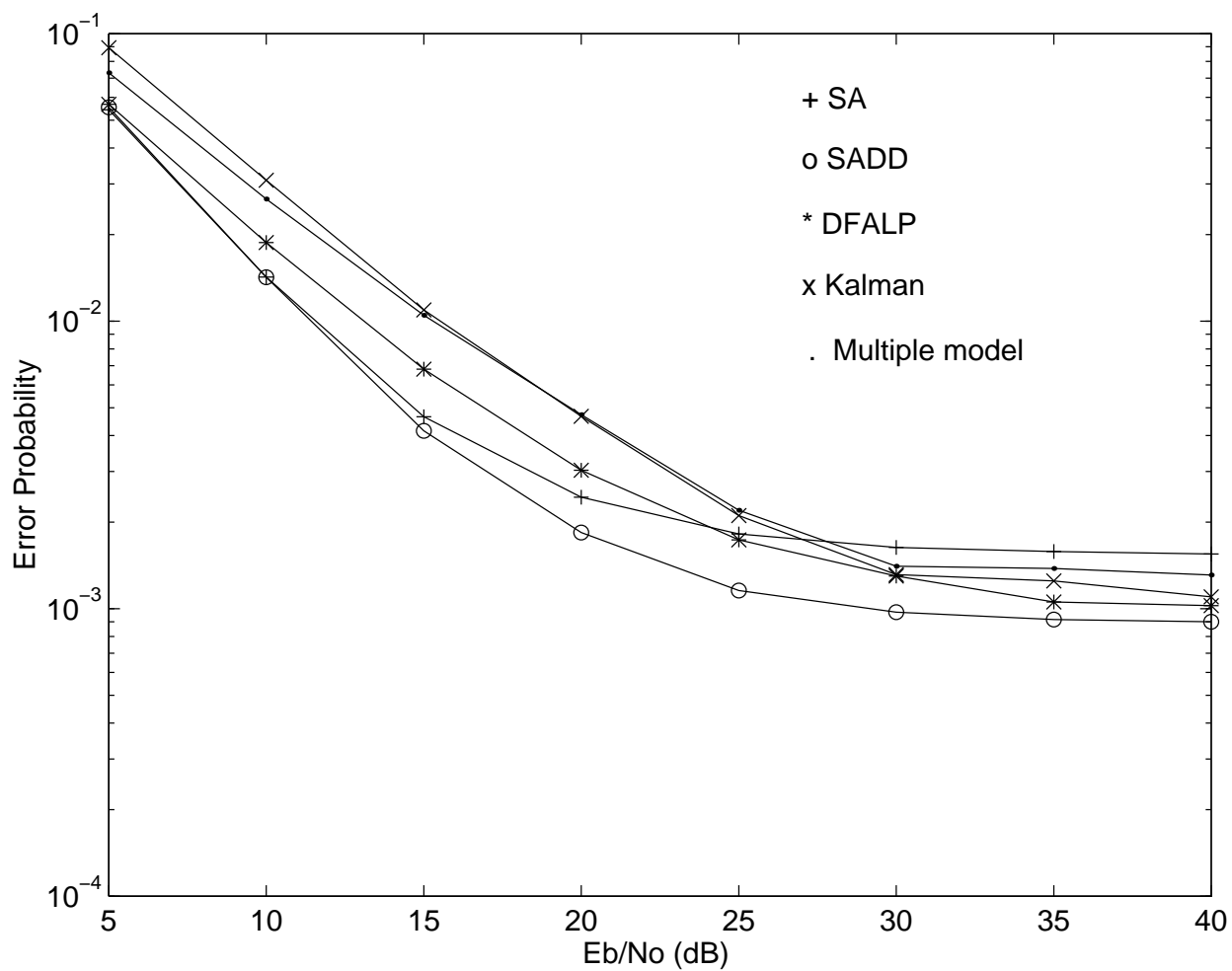


Figure 3.4: BER for SA, SADD, DFALP, Kalman filtering, multiple model algorithm in average shadowed Rician fading, normalized fading bandwidth at 0.05, pilot symbol rate at 5, uncoded QPSK modulation.

In the later part of this chapter, we apply the symbol-aided algorithm to shadowed Rician fading channels in coded modulation. One training symbol is sent for every $k_t - 1$ data symbols. We pass the pilot symbols through a third-order FIR filter, and then use linear interpolation to estimate the channel state information. This allows for improved channel estimation during data transmission mode and minimum complexity and delay for channel estimation.

3.3 Interleaving

Interleaving attempts to eliminate the burst error characteristic of a fading channel by separating symbols which are close to each other in time. The inner code used in the system design, trellis coded modulation (TCM), is designed for a random error channel and does not have optimal performance over bursty error fading channels [18]. When the channel is in a deep fade, errors tend to last for several symbols. Interleaving is a standard method for scrambling data and makes a burst-error channel appear to be a random-error channel at the receiver. The symbols are then descrambled at the receiver. Since the data from the inner TCM code has some residual bursty errors, RS or BCH codes are used to correct these errors. Figure 3.5 shows the inner and outer interleavers in the system. Outer interleaving can also be used to scramble the residual bursty errors and makes the outer error correcting codes more efficient.

From Figure 3.5 we can see there are two different interleavers that may possibly be used in our system, the outer interleaver is between the outer RS (or BCH) and inner TCM codes, as well as the inner interleaver for the TCM code.

There are two different kinds of interleavers that may possibly be used in our system: convolutional interleaving and block interleaving. Figure 3.6 shows the concept of convolutional interleaving. Block interleaving is shown in Figure 3.7. Each interleaving method has its own advantage. Block interleaving has two parameters to choose from: interleaving depth d , and interleaving span s . The total delay for block

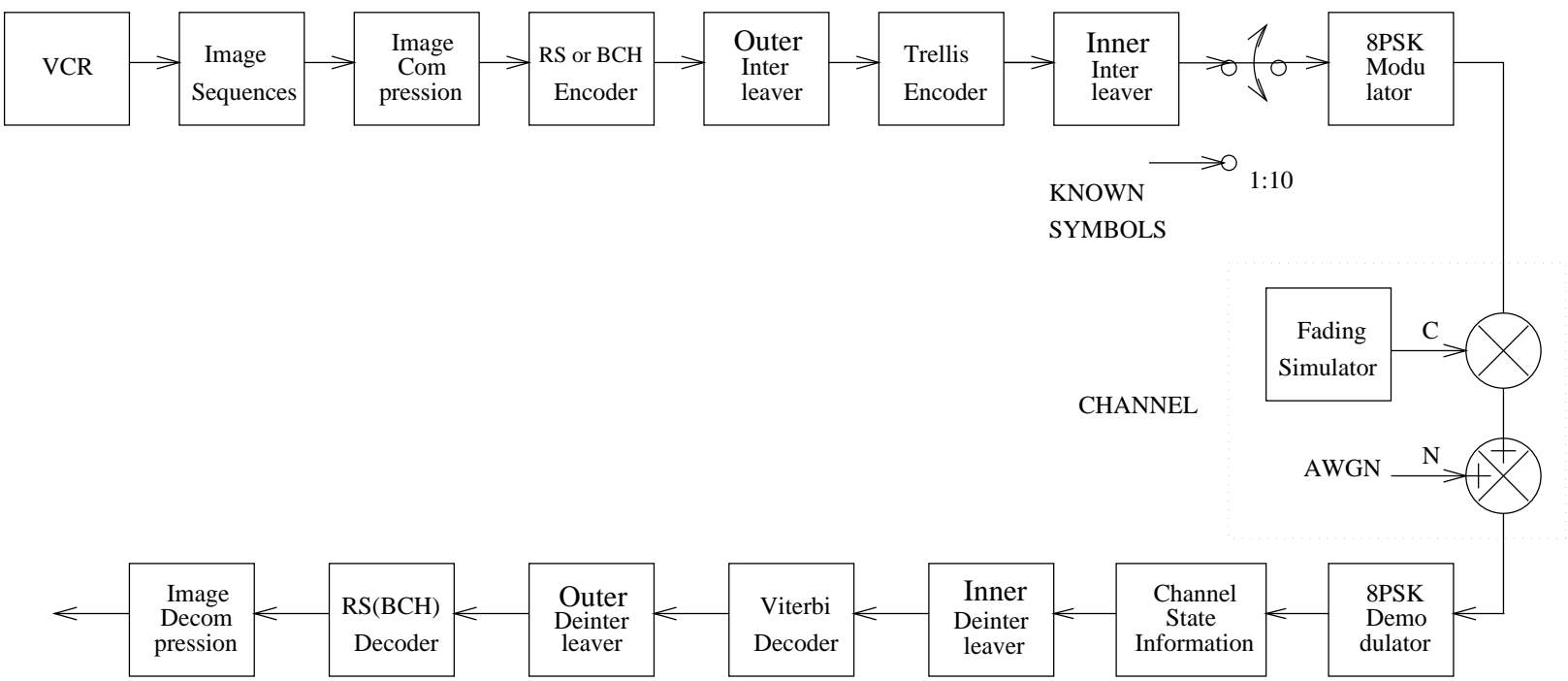
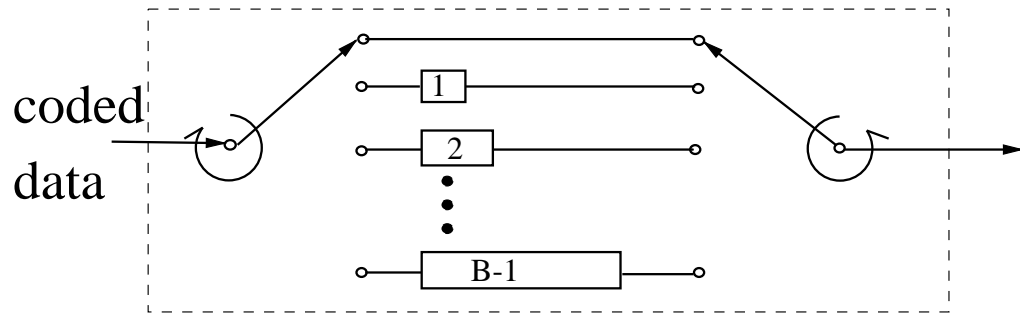


Figure 3.5: System Block Diagram

Convolutional Interleaver



Convolutional Deinterleaver

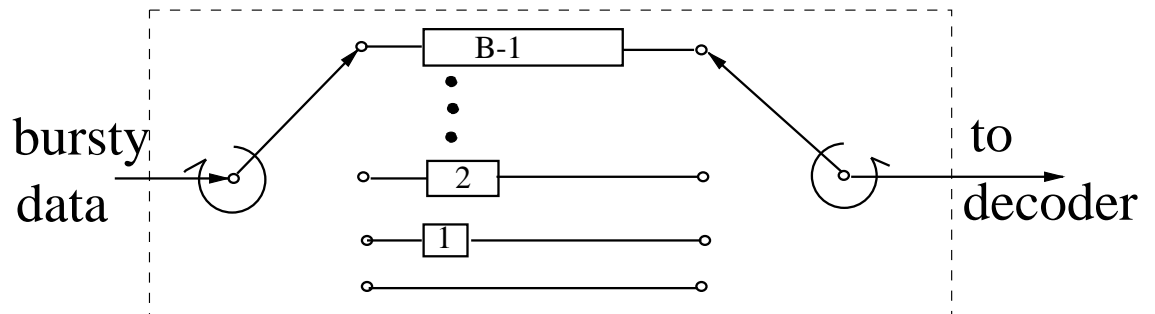


Figure 3.6: Concept of convolutional interleaving

interleaving and de-interleaving is $d(s - 1) + s(d - 1)$. In convolutional interleaving, there is only one variable B , and the total delay for convolutional interleaving is $B(B - 1)$. For the same degree of interleaving (i.e. if s , d and B are very close), convolutional interleaving has around half the delay of block interleaving. Factors affecting the choice of interleaving method include maximum fading duration, Viterbi decoder length, error correction code word length, and residual bursty error length from the inner code. Viterbi decoder length and maximum fading duration affect the choice of inner interleaving structure and parameters. On the other hand, the outer interleaving depends on the outer code word length and residual bursty error length from the inner code. If the interleaving depth d and interleaving span s are nearly equal, convolutional interleaving has less delay than block interleaving. If these two values are widely separated, block interleaving may have less delay.

3.4 Design of inner code and inner interleaver

In a power and bandwidth limited environment, such as in the case of a portable video terminal for mobile satellite channels, the desired system performance should be achieved with the smallest possible power and bandwidth. Trellis-coded modulation (TCM) is a combined coding and modulation scheme for improving the reliability of a digital transmission system without increasing the transmitted power or the required bandwidth. It treats convolutional encoding and modulation as one entity. The decoding of TCM is not based on the free Hamming distance of the convolutional code, it is based on the free Euclidean distance between transmitted signal sequences. Finally, the detection of the transmitted symbols will involve soft rather than hard decisions. The concept of TCM was first proposed by Ungerboeck [39]. It results in significant coding gains without requiring any bandwidth expansion. The essential part of TCM is the mapping rules for modulation after convolutional encoding. The following design rules have been suggested by Ungerboeck:

- Members of the same partition are assigned to parallel transitions (i.e., members of distance $d_{min}^{(1)}$).

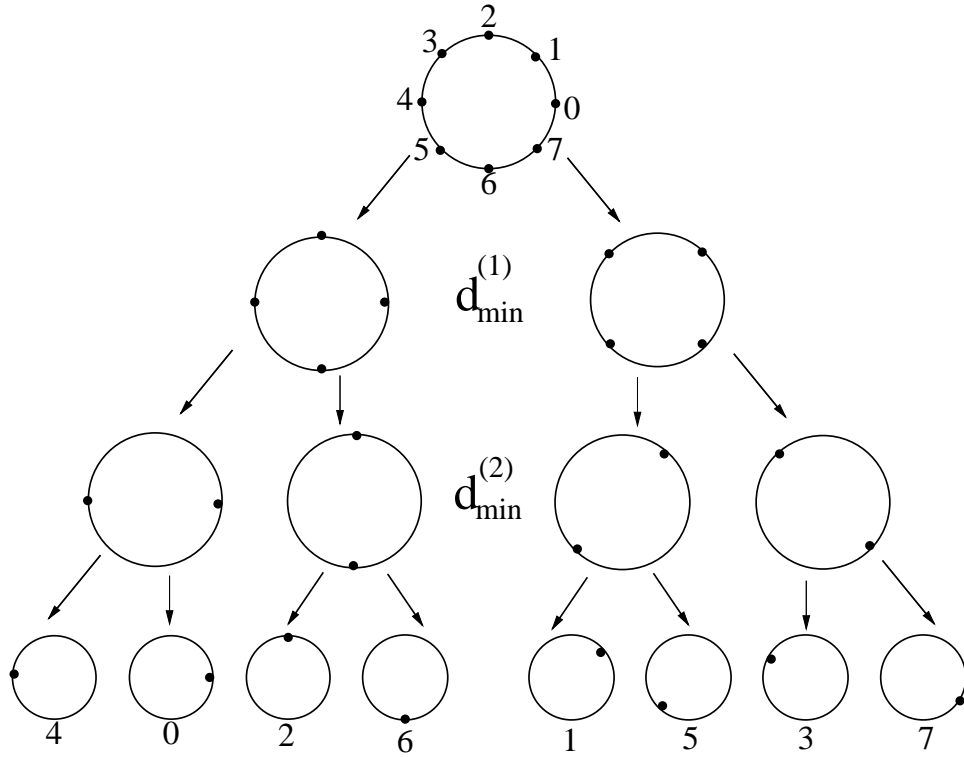


Figure 3.8: Set partitioning of an 8-PSK constellation

- Members of the next larger partition are assigned to adjacent transitions (i.e., members of distance $d_{min}^{(2)}$).
- All the signals are used equally often.

Figure 3.8 shows set partitioning for TCM.

The 8-state 8-PSK, rate 2/3 design from Ungerboeck [39] is used for our TCM code, and a Viterbi decoder [17] is utilized as a sequence estimator. A software Viterbi decoder developed by Joubin Karimi of Queen's University is used in simulations. Figures 3.9 and 3.10 show the encoder and bit-to-symbol mapping rule for 8-state 8-PSK trellis coded modulation.

Let E' be the average energy per symbol for a QPSK signal, and d_{min}^2 be the minimum square distance between two symbols. The relation between E' and d_{min} satisfies [6]:

$$\frac{d_{min}^2}{E'} = 2 \quad (3.24)$$

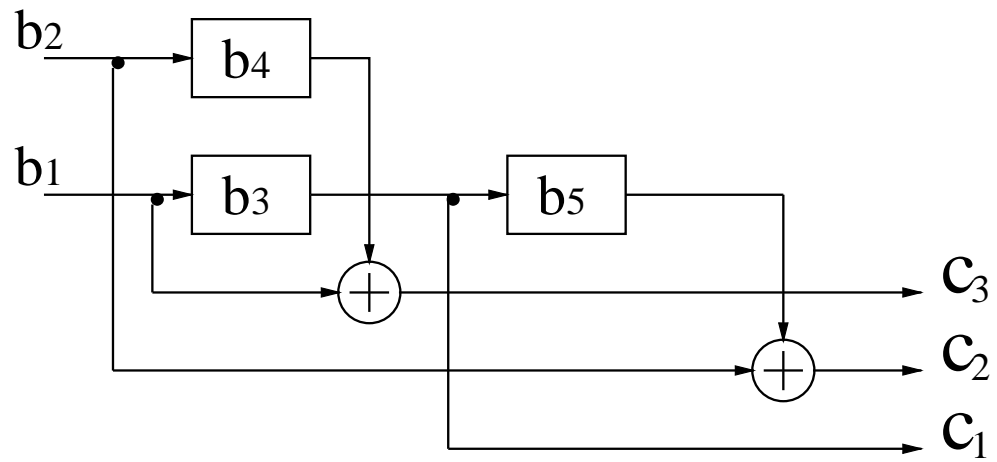
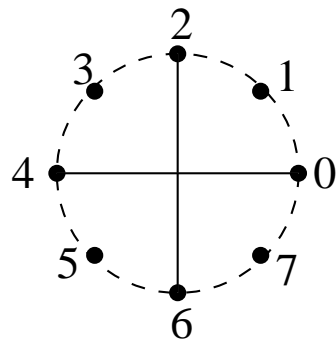


Figure 3.9: 8-state 8-PSK TCM encoder



Symbol	C_1	C_2	C_3
0	0	0	0
4	0	0	1
2	0	1	0
6	0	1	1
1	1	0	0
5	1	0	1
3	1	1	0
7	1	1	1

Figure 3.10: Bits to symbol mapping rule for 8-state 8-PSK TCM

Let E be the average energy per symbol for 8-PSK TCM, and d_{free} be the minimum Euclidean squared distance between all allowable pairs of sequences. An error event for TCM is defined as the period beginning with a split from the correct sequence and ending with a merge to the correct sequence. The distance between the two sequences is the sum of the distances between every symbol over the error event. Figure 3.11 shows the Trellis diagram and minimum distance error event for an 8-state 8-PSK TCM code.

$$\begin{aligned} \frac{d_{free}^2}{E} &= \frac{[d^2(0, 6) + d^2(0, 7) + d^2(0, 6)]}{E} \\ &= 2 + 4 \sin^2(\pi/8) + 2 = 4.586 \end{aligned} \quad (3.25)$$

The coding gain for 8-state 8-PSK TCM over uncoded QPSK is:

$$\begin{aligned} \text{Coding Gain} &= \frac{\frac{d_{free}^2}{E}}{\frac{d_{min}^2}{E'}} \\ &= \frac{4.586}{2} = 3.6\text{dB} \end{aligned} \quad (3.26)$$

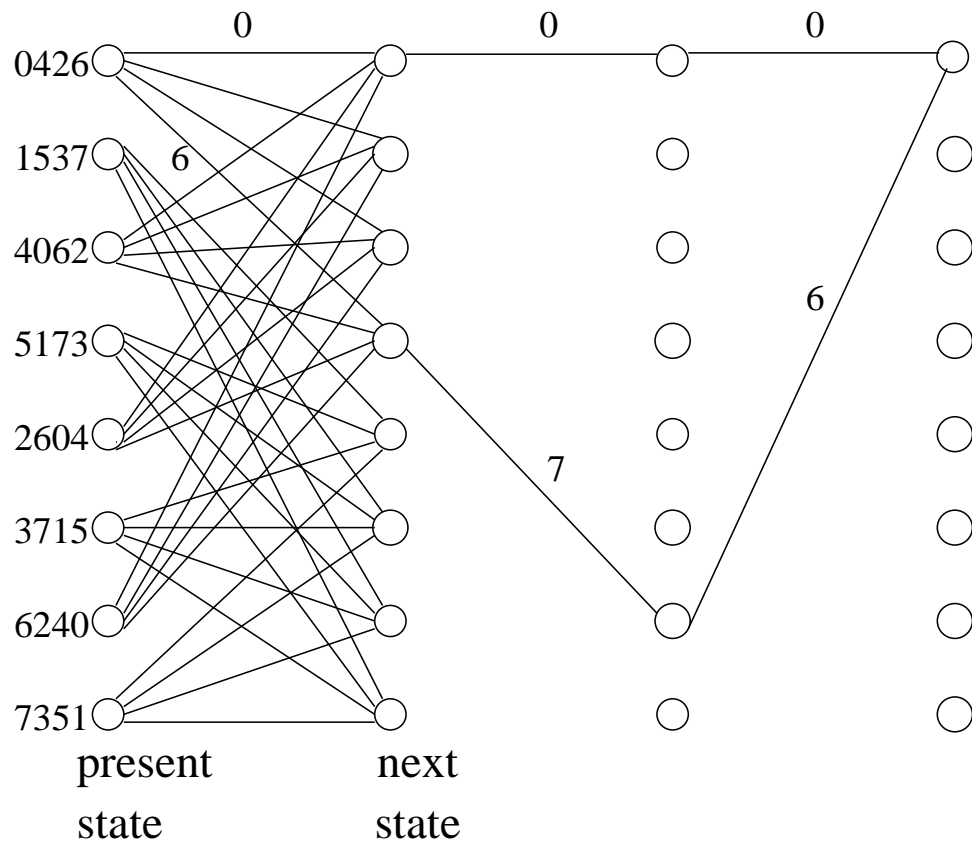
For the same bandwidth and power requirements, there is a 3.6 dB gain over uncoded QPSK in bit-error-rate performance on an AWGN channel.

Trellis-coded modulation (TCM) conserves bandwidth while achieving a high coding gain. The decoding of TCM codes is based on the Viterbi algorithm. The branch metric for decoding is computed over all possible x_k as:

$$m(y_k, x_k) = |y_k - \hat{c}_k x_k|^2 \quad (3.27)$$

where \hat{c}_k is the fading channel state information estimated as discussed in Section 3.2 and x_k is a member of the coded signal constellation.

The inner interleaving parameters are chosen according to the maximum fading duration and Viterbi decoder length. The Viterbi decoder length is chosen to be 6 times the memory length of the inner TCM code [18]. For 8-state 8-PSK TCM, the Viterbi decoder length is 18. For a fading bandwidth of 0.05, the interleaving depth was set to 10 symbols. This choice gives an effective normalized bandwidth f_0 of 0.5, at which the correlation between any two adjacent, deinterleaved symbols becomes



$$d_{\text{free}}^2 = d^2(0,6) + d^2(0,7) + d^2(0,6)$$

Figure 3.11: Trellis diagram and minimum distance error event for an 8-state 8-PSK TCM

negligible. This effect can be verified from (2.39), where a zero of $\rho(T_s)$ is found near 1 when $f_0 = 0.5$. The maximum fading duration is $0.5/f_0$ for arbitrary f_0 .

3.5 Design of Outer codes and outer interleaver

On fading channels with TCM, errors tend to propagate due to unreliable soft-decision decoding information. It is well known that RS (or BCH) codes perform very well on burst-error channels and are therefore used as the outer code to combat residual burst errors. In this concatenated modulation scheme, the inner code is 8-state 8-PSK TCM as discussed in the previous section. The outer code may be either an RS or a BCH code. Figure 3.5 shows the system block diagram.

As shown in Figure 3.5, interleaving is performed between the inner TCM and outer forward error correction (FEC) codes. However, in GEO satellite communication systems, the long delay incurred by receivers is not acceptable. We use two different FEC schemes to test the tradeoff between low bit error rate (BER) and increased delay:

Scheme 1: We use a (255, 223) standard NASA RS code. One block code (255×8 bits) can correct 16 symbol errors or 128 bit burst errors. Due to the large delay incurred, outer interleaving is not introduced between the outer RS and inner TCM codes.

Scheme 2: An outer (255, 223) BCH code is concatenated with an inner TCM code. One block code (255 bits) can correct 4 bit errors. In this case, different outer interleaving depths between the inner and outer codes are used. We compare the performance of these two schemes in the context of the system shown in Figure 3.5.

3.6 Results on Video Test Sequences

3.6.1 Simulation Parameters

The system block diagram is shown in Figure 3.5. The outer error correction code is a (255,223) RS or BCH code. The inner code is 8-state 8-PSK TCM and the inner interleaving depth is 30 symbols for 24 kbit/s video and 60 for 64 kbit/s video sequences. For every 9 data symbols, one training symbol is sent ($K_t = 10$). The normalized fading channel bandwidths are 0.015432 and 0.005787, corresponding to the vehicle speed of 100 km/h, symbol rate of 15 kBd and 40.5 kBd, and 2.5 GHz carrier frequency. Monte-Carlo simulations are based on colour video image sequences of resolution QCIF (176×144 pels) at a rate of 10 frames/sec, with 25 minutes (15000 frames) of motion video at 24 kbit/s and 8 minutes of video at 64 kbit/s. Test video sequences include the well-known Miss America, Susie, Salesman, Mother and daughter, Grandma, Carphone, Foreman, Claire, Stennis, and some other sequences digitized locally in our Image Processing and Communications Laboratory at Queen's University.

3.6.2 Results and Discussion

Figure 3.12 shows bit error rate performances of inner 8-state 8-PSK TCM at different SNR and shadowing levels. As can be seen, bit error rates of $10^{-3} - 10^{-4}$ can be achieved by inner codes alone at SNR in the range of 9-11 dB. From Figures 3.13 and 3.14, further improvement of more than two orders of magnitude in the BER performance can be obtained by employing an outer FEC code. In Figure 3.12, the different normalized fading bandwidths are due to the different data rates.

We tested two different concatenated coding schemes: RS & TCM, BCH & TCM. Since the RS (255, 223) code contains 255 bytes/block, which is 8 times the number of bits in a BCH block, we only introduced outer interleaving for the shorter BCH coding scheme. The results show that for BCH codes with a large interleaving depth of 80, BER performance is around 1.5 dB better than RS codes without interleaving.

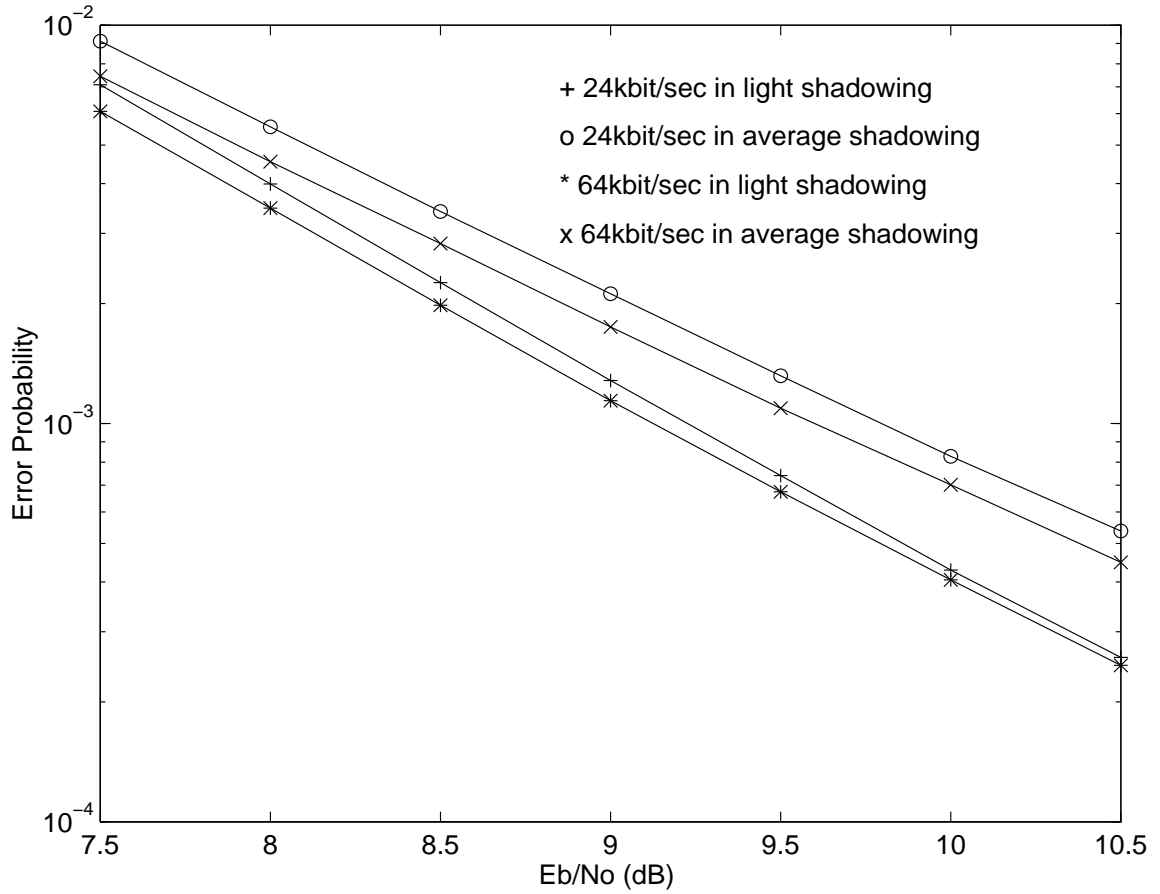


Figure 3.12: Inner TCM code performance for 24 kbit/s and 64 kbit/s video, normalized fading bandwidth at 0.0154 and 0.0057 respectively, pilot symbol rate k_t at 10.

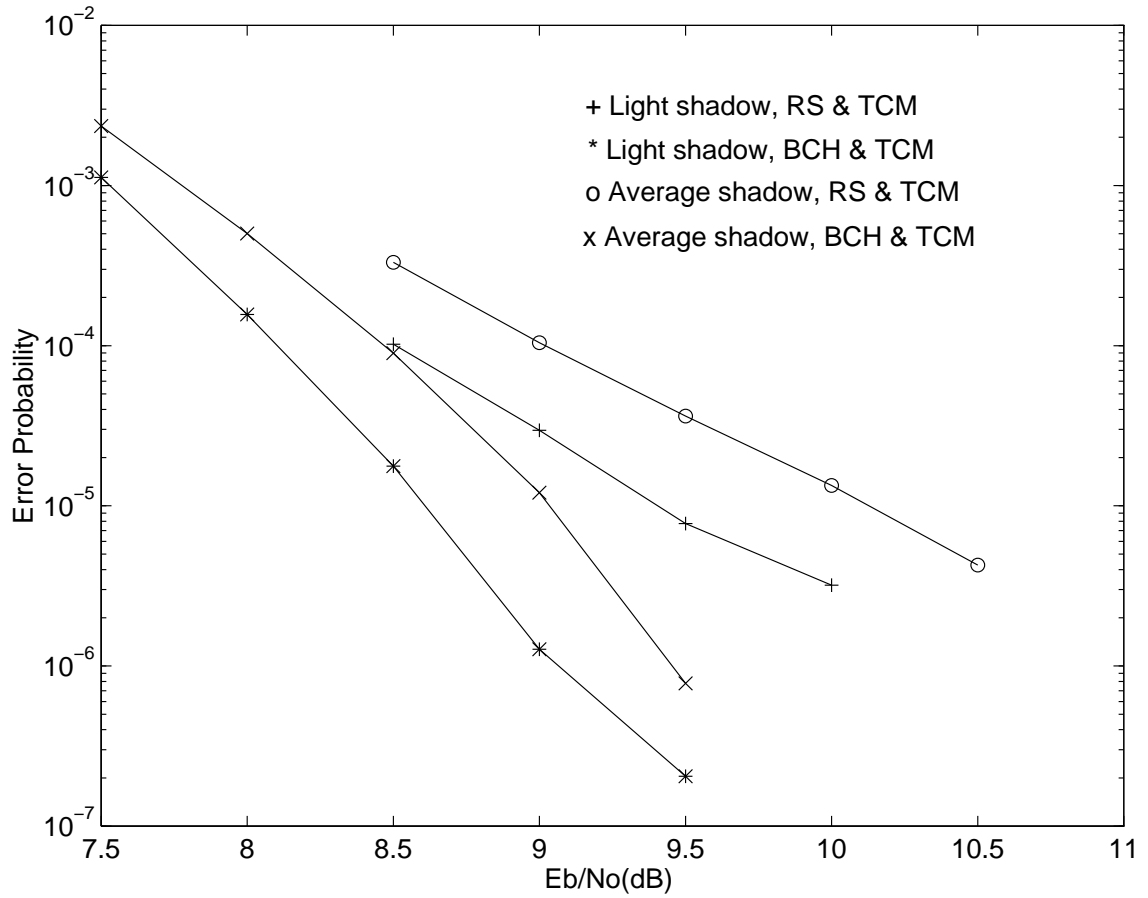


Figure 3.13: System performance for 24 kbit/s video, normalized fading bandwidth at 0.0154, pilot symbol rate k_t at 10.

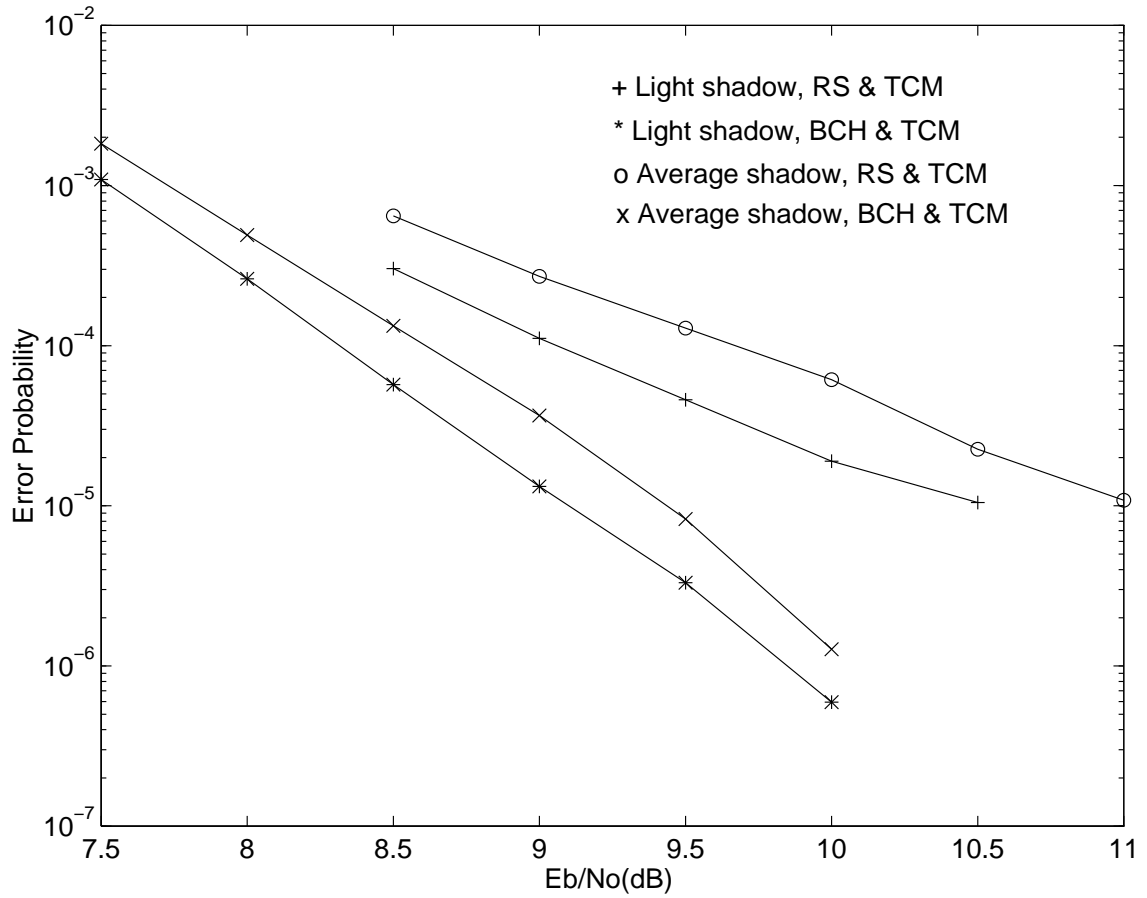


Figure 3.14: System performance for 64 kbit/s video, normalized fading bandwidth at 0.0057, pilot symbol rate k_t at 10.

Also, as shown, the power requirement and delay penalty for interleaving is high. Table 3.1 shows the different delays.

Table 3.1: Delay for different schemes

Delay	RS & TCM	BCH & Outer Interleaving & TCM
24kbit/s	145ms	1.546s
64kbit/s	89ms	615ms



Figure 3.15: Transmitted video through average shadowed mobile satellite channel, channel SNR=10.0dB, RS & TCM coding, one of 200 error frames in a total 15000 video frames

For BCH codes with large interleaving, BER performance is around 2 dB better than RS codes without interleaving. Also, as shown, the SNR penalty for interleaving is high. For 24 and 64 kbits/s compressed image bit streams, the outer (255,223) RS (or BCH) code yields a total bit rate of 27.44 and 73.18 kbits/s, which are baud rates of 13.72 and 36.59 kBd respectively, for 8-PSK TCM. After adding the pilot symbols ($k_t = 10$) the system baud rate becomes 15.2 and 40.5 kBd, respectively. The system shows near error-free performance at SNR 9 - 12 dB at light and average shadowing mobile satellite channels.

Generally, when the BER was below 10^{-6} , the channel errors were rare and had a negligible effect on image quality. Figure 3.15 shows one of 200 error frames decoded out of a total of 15000 video frames transmitted through an averaged shadowed

mobile channel at a channel signal-to-noise ratio of 10 dB with RS & TCM error correction coding and BER of 1.4×10^{-5} . From examining the video sequences, there are different error patterns present for different video sequences. For the low error rates encountered here (BER less than 6×10^{-5}), the H.263 source codec's forced updating strategy as described in Section 2.4.2 is robust enough to recover all the video sequences. Because of the low channel BER, only a few frames, representing 20 seconds total duration in a 25 minute sequence, exhibit visible burst errors (as in Figure 3.15) and the remaining frames are error-free. When the channel SNR is greater than 12 dB, the BER is less than 10^{-7} and there is no error in the 25 minute video sequences.

We have applied this system to several other video sequences and have recorded the results on video tape for subjective perceptual evaluation of quality. The three sample video sequences are "Miss America", "Susie", and "Salesman". The original sequences on the tape are in QCIF (176x144 pels), 4:1:1 YUV format, 150 frames each at 30 frames/sec, subsampled to 50 frames each at 10 frames/sec. Figures 3.16 to 3.24 show sample frames of "Miss America", "Susie", and "Salesman" from the tape. Figures 3.18, 3.21 and 3.24 are examples of significant distortion. As mentioned, at channel SNR greater than 12 dB, the channel BER is less than 10^{-7} . The reason for displaying the distortion at the 10 dB point at average shadowing is that this represents a threshold SNR where the distorted bit stream can still be recovered. It is also interesting to observe the types of visible distortion that occur at 10 dB. This may be useful for designing error concealment techniques in the future.

3.6.3 Conclusion

Our investigations using a software H.263 24 kbit/s and 64 kbit/s codec, concatenated FEC coding, and on-line channel state estimation show that robust moving-image transmission through shadowed mobile satellite channels is feasible. Concatenated codes and pilot symbols result in a 15.2 kBd and 40.5 kBd system, allowing for a near error-free image transmission at channel SNR between 9-12 dB. Depending on



Figure 3.16: Original Miss America at 9.1 Mbits/sec showing frames 117, 126, 135, and 144 from top left to bottom right.



Figure 3.17: H.263 compressed Miss America at 24 kbits/sec, showing frames 117, 126, 135, and 144 from top left to bottom right.



Figure 3.18: H.263 compressed Miss America at 24 kbits/sec in average shadowed fading channel, 10 dB SNR, 15 kD, 145 msec delay, showing frames 117, 126, 135, and 144 from top left to bottom right.



Figure 3.19: Original Salesman at 9.1 Mbits/sec, showing frames 108, 116, 124, and 132 from top left to bottom right.



Figure 3.20: H.263 compressed Salesman at 24 kbits/sec, showing frames 108, 116, 124, and 132 from top left to bottom right.



Figure 3.21: H.263 compressed Salesman at 24 kbits/sec in average shadowed fading channel, 10 dB SNR, 15 kBd, 145 msec delay, showing frames 108, 116, 124, and 132 from top left to bottom right.



Figure 3.22: Original Susie at 9.1 Mbits/sec, showing frames 108, 120, 132, and 144 from top left to bottom right



Figure 3.23: H.263 compressed Susie at 24 kbits/sec, showing frames 108, 120, 132, and 144 from top left to bottom right



Figure 3.24: H.263 compressed Susie at 24 kbits/sec in average shadowed fading channel, 10 dB SNR, 15 kBd, 145 msec delay, showing frames 108, 120, 132, and 144 from top left to bottom right

different system delay requirements, RS & TCM or BCH & TCM can be used for interactive transmission or one-way broadcasting applications. A further point we had verified is that interleaving is very effective in improving coding BER performance; there is at least 2 dB gain for outer interleaving (BCH with outer interleaving) over no outer interleaving (RS without outer interleaving) cases.

3.7 Application of video transmission to other channels

3.7.1 Application to Rician channels

In addition to the shadowed mobile satellite channel, our simulations include Rician and Rayleigh fading channels to access the different SNR requirements under different channel situations. The K-factor for simulating Rician flat fading is 10 dB. Figure 3.25 shows the inner TCM code performance for 24 kbit/s and 64 kbit/s video over a Rician channel with K-factor=10dB.

Comparing the results in Figures 3.25 and 3.12 in average shadowing, the Rician channel with a K-factor of 10 dB requires a channel SNR around 2 dB less to achieve the same inner TCM code performance as an average shadowed mobile satellite channel.

3.7.2 Application to Rayleigh channels

Figure 3.26 shows inner TCM code performance for 24 kbit/s and 64 kbit/s video over a Rayleigh channel. Normalized Doppler frequencies are set the same as in Section 3.6.1. Although the Doppler frequencies are the same under shadowed Rician, Rician and Rayleigh fading channels, the low-pass filter (lpf) bandwidth used in the symbol-aided channel estimation algorithm is different under the three different channels. Based on trial and error, the low-pass filter bandwidth is largest (no lpf) for Rayleigh fading and smallest (0.22) for the Rician (K=10 dB) channel and 0.36 for

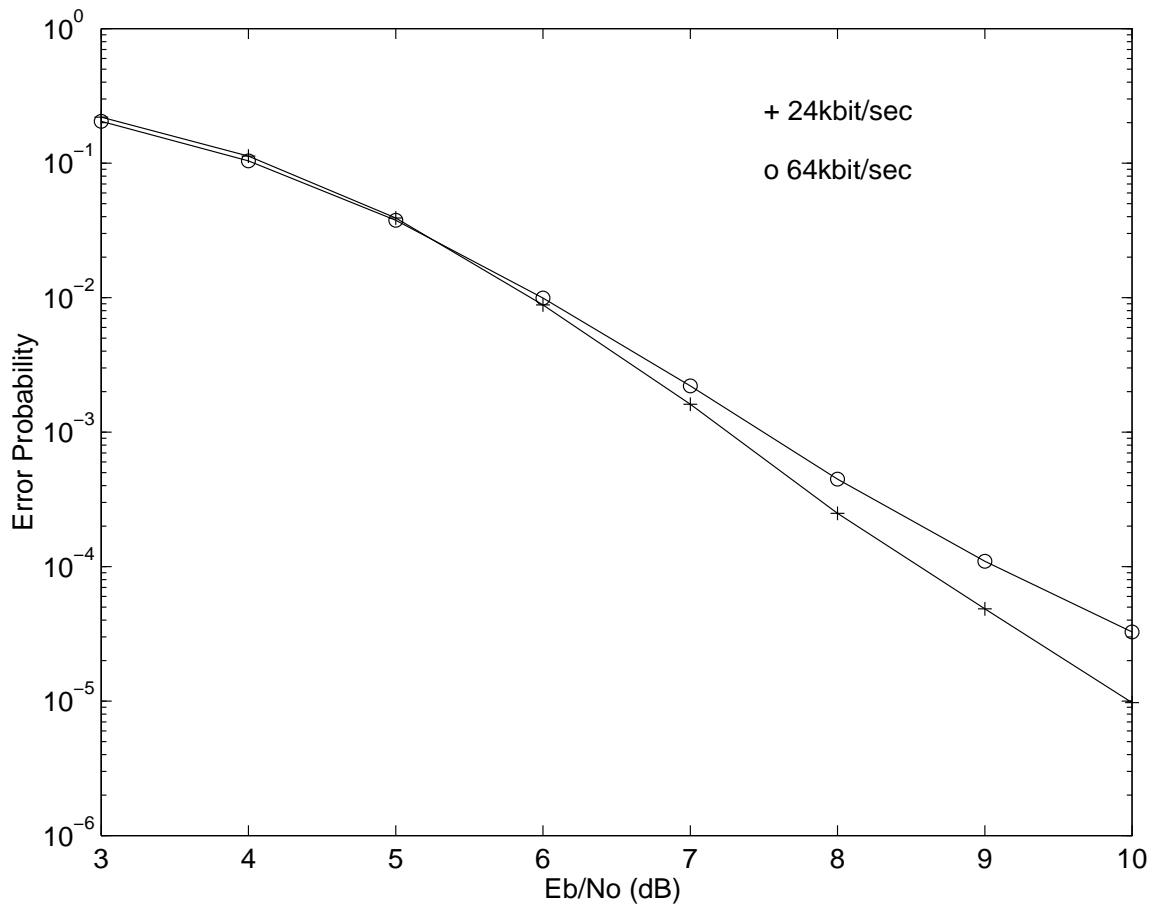


Figure 3.25: Inner TCM code performance for 24 kbit/s and 64 kbit/s video over a Rician channel, $K=10$ dB, normalized fading bandwidth at 0.0154 and 0.0057 respectively, pilot symbol rate k_t at 10.

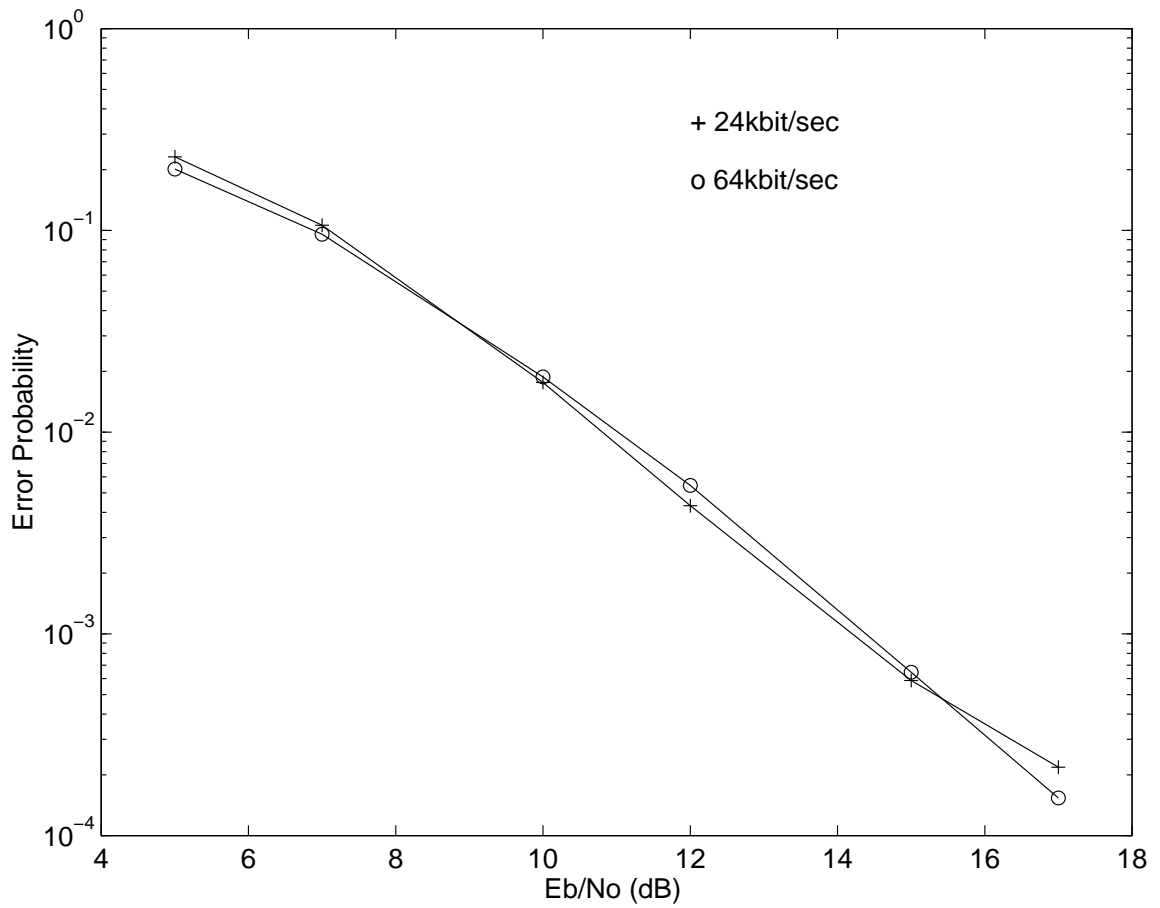


Figure 3.26: Inner TCM code performance for 24 kbit/s and 64 kbit/s video over a Rayleigh channel, normalized fading bandwidth at 0.0154 and 0.0057 respectively, pilot symbol rate k_t at 10.

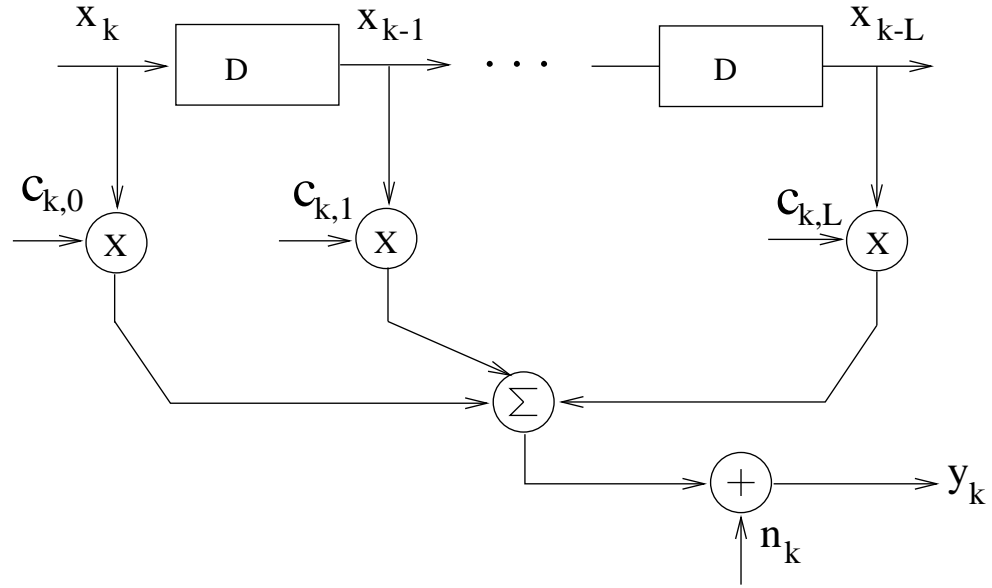


Figure 3.27: Tapped delay line model for frequency-selective fading channel

shadowed Rician fading channel, where a bandwidth of 0.5 corresponds to a frequency of π radians/sec.

Comparing the results in Figures 3.26 and 3.12 in average shadowing, the Rayleigh channel requires an additional channel SNR of 5 dB to achieve the same inner TCM code performance as the average shadowed mobile satellite channel.

3.7.3 Application to 2-Ray frequency-selective Rayleigh fading channels

3.7.3.1 2-Ray frequency-selective Rayleigh fading channels

In this subsection, the error performance of uncoded QPSK and coded 8-state 8-PSK TCM signals transmitted over a 2-ray frequency-selective Rayleigh fading channel are considered. A Viterbi receiver with estimated channel state information is used to decode the transmitted signal sequence.

A general mathematical model for a frequency-selective Rayleigh fading channel is the tapped delay line model shown in Figure 3.27. The 2-ray model is a special case of Figure 3.27.

Here x_k represents the transmitted PSK symbol in the k th interval taking on either a member of a QPSK or 8-PSK signal constellation. According to Figure 3.27, the corresponding received symbol y_k is:

$$y_k = \sum_{j=0}^L x_{k-j} c_{k,j} + n_k \quad (3.28)$$

where the $c_{k,j}$'s, $j=0, \dots, L$, are correlated, zero-mean complex Gaussian random variables, and n_k is a zero-mean complex Gaussian random variable with unit variance. The $c_{k,j}$'s represent the effect of frequency-selective fading while the n_k 's represent the effect of the channel's white Gaussian noise. In practice, channel state information can be obtained through a channel sounding technique such as inserted pilot symbols [46]. The optimal decoder is a Viterbi decoder that selects the sequence $\hat{x} = (\hat{x}_1, \hat{x}_2, \dots, \hat{x}_N)$ which minimizes the metric:

$$J(\hat{x}) = \sum_{k=1}^N \left| y_k - \sum_{j=0}^L \hat{x}_{k-j} \hat{c}_{k,j} \right|^2 \quad (3.29)$$

where the $\hat{c}_{k,j}$'s are the estimated multi-ray fading state information.

3.7.3.2 Comparison of two different modulations for frequency-selective channels: uncoded QPSK and coded 8-PSK TCM

In this section, we compare the error performance of uncoded QPSK and coded 8-state 8-PSK TCM transmitted over a 2-ray frequency-selective Rayleigh fading channel. Gaussian random variables are passed through four third-order Butterworth filters to simulate 2-ray frequency-selective channels. Three pilot symbols are inserted between every nine data symbols to estimate the multipath fading channel state information. Because of the selectivity property of the channel, inner interleaving cannot be used to improve the system performance.

Assume at time k , $k-1$ and $k-2$, three pilot symbols (x_k , x_{k-1} and x_{k-2}) are inserted. Using (3.28), the received signals are:

$$y_k = c_{k,0}x_k + c_{k,1}x_{k-1} + n_k, \quad (3.30)$$

and

$$y_{k-1} = c_{k-1,0}x_{k-1} + c_{k-1,1}x_{k-2} + n_{k-1}. \quad (3.31)$$

as the channel is a slow fading channel, we assume that $c_{k,0} = c_{k-1,0}$ and $c_{k,1} = c_{k-1,1}$. This yields a linear system of two equations and two unknowns. With this slow fading assumption, equations (3.30) and (3.31) are solved to obtain the two ray channel state information $c_{k,0}$ and $c_{k,1}$.

This tracking algorithm is therefore valid for a slowly fading channel (experimentally, we have found that f_0 should be less than 0.01) due to the equal complex channel gain assumption above. The two-ray complex fading channel gains of the data symbols are derived using linear interpolation between two pairs of channel information from the pilot symbols.

The BER performance of uncoded QPSK under a two-ray frequency-selective channel with perfect channel state information closely matches the simulation result in [11]. Figures 3.28 and 3.29 show uncoded QPSK performance for 24 kbit/s and 64 kbit/s video over a two-ray Rayleigh frequency-selective fading channel with perfect channel state information and with our pilot channel estimation scheme, respectively. Equal energy rays (ratio=1) and unequal energy split with a ratio of 10 are tested. As shown, equal energy rays give superior results compared to unequal energy rays. This can be understood by noting that under perfect channel state information, equal energy rays optimize the inherent diversity effect of a two-beam channel. Figures 3.30 and 3.31 show coded 8-state 8-PSK TCM performance for 24 kbit/s and 64 kbit/s video over a two-ray Rayleigh frequency-selective fading channel with perfect channel state information and pilot channel state estimation, respectively. Equal energy two-ray (ratio=1) and unequal energy split with a ratio of 10 are also tested.

Now the performances of uncoded QPSK and coded 8-PSK TCM are compared under the frequency-selective channels. Figures 3.34 and 3.35 show that the performance of 8-state 8-PSK TCM is inferior to uncoded QPSK under the frequency-selective channel both with perfect channel state information and with pilot channel state information. This is not surprising: inner TCM code is designed for a random

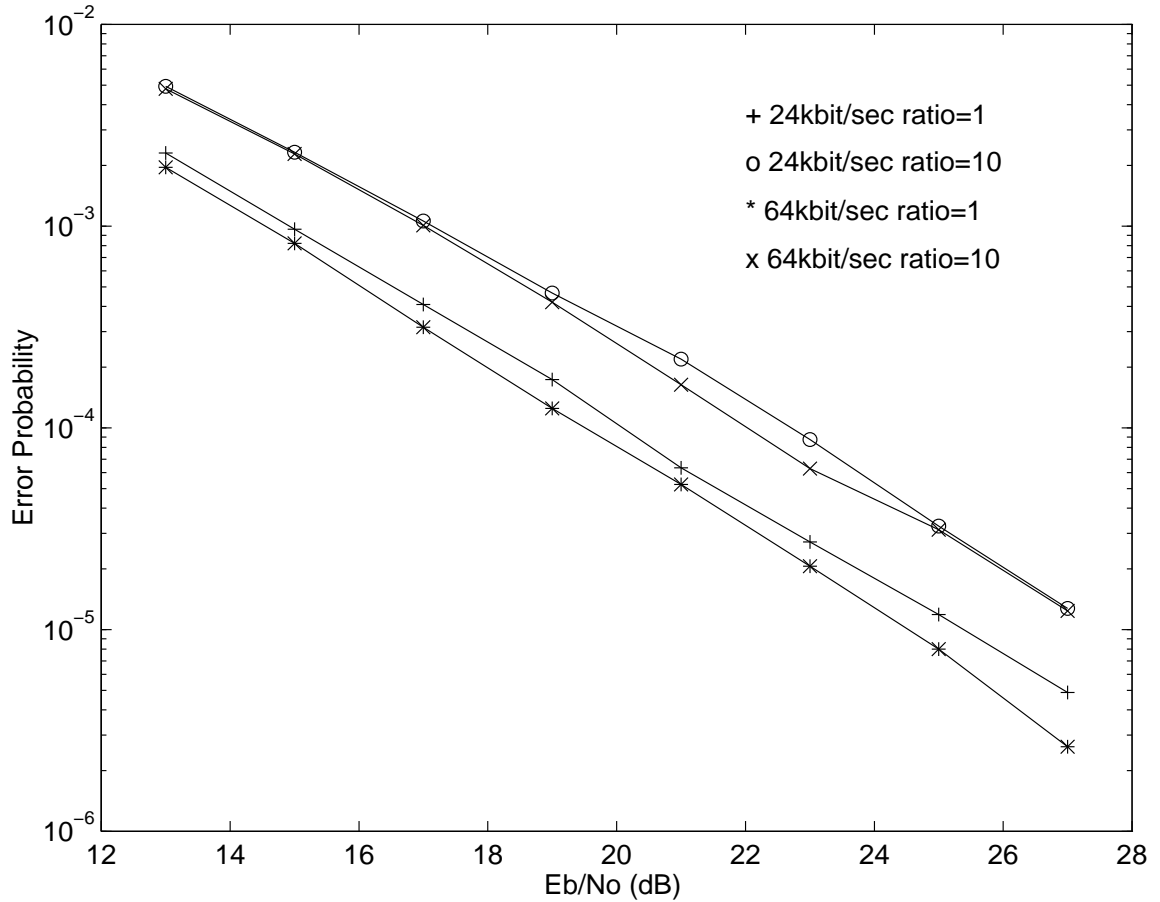


Figure 3.28: Uncoded QPSK performance for 24kbit/s and 64kbit/s video over two-ray Rayleigh frequency-selective fading channel, perfect channel state information, ratio is first ray energy divided by second ray energy. Normalized fading bandwidth at 0.0077 and 0.00286 respectively, and 3 pilot symbols are inserted every 9 data symbols.

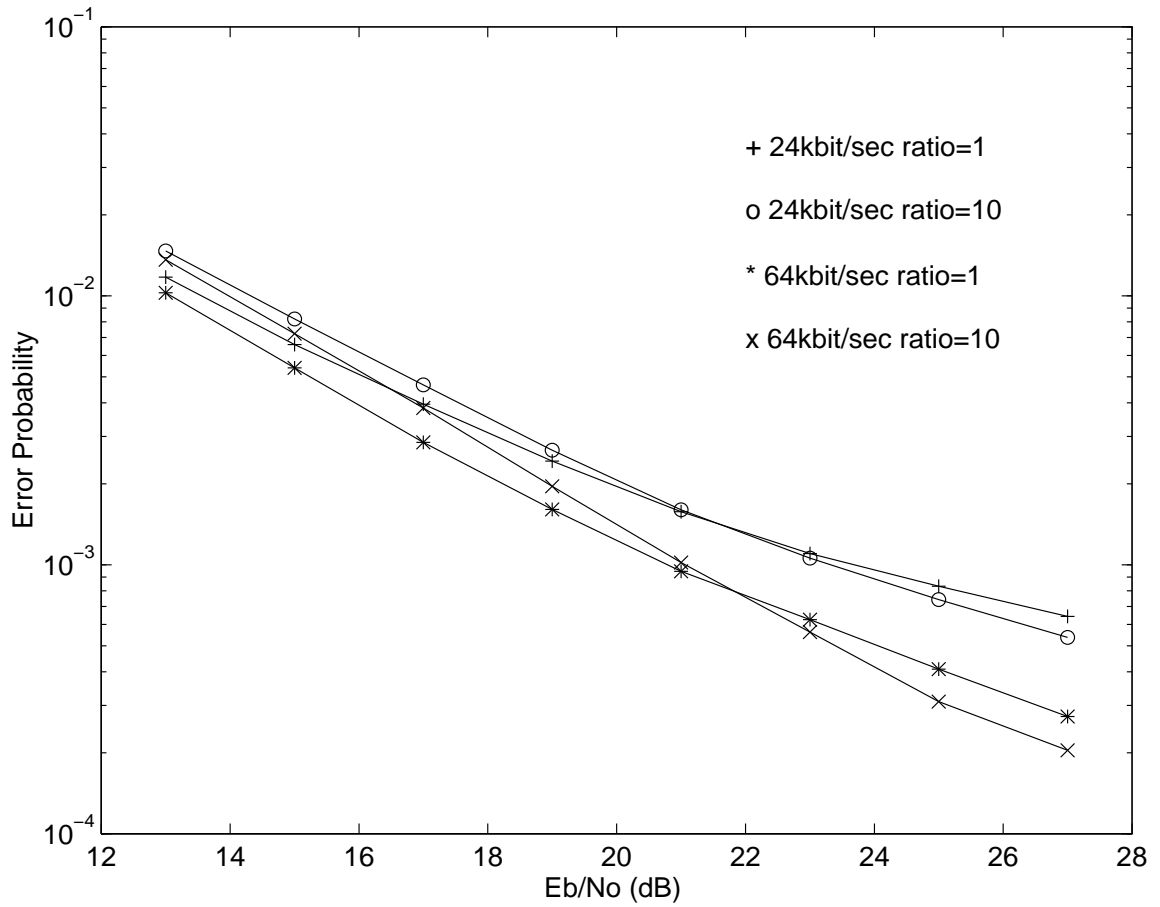


Figure 3.29: Uncoded QPSK performance for 24kbit/s and 64kbit/s video over two-ray Rayleigh frequency-selective fading channel, pilot channel state estimation, ratio is first ray energy divided by second ray energy. Normalized fading bandwidth at 0.0077 and 0.00286 respectively, and 3 pilot symbols are inserted every 9 data symbols.

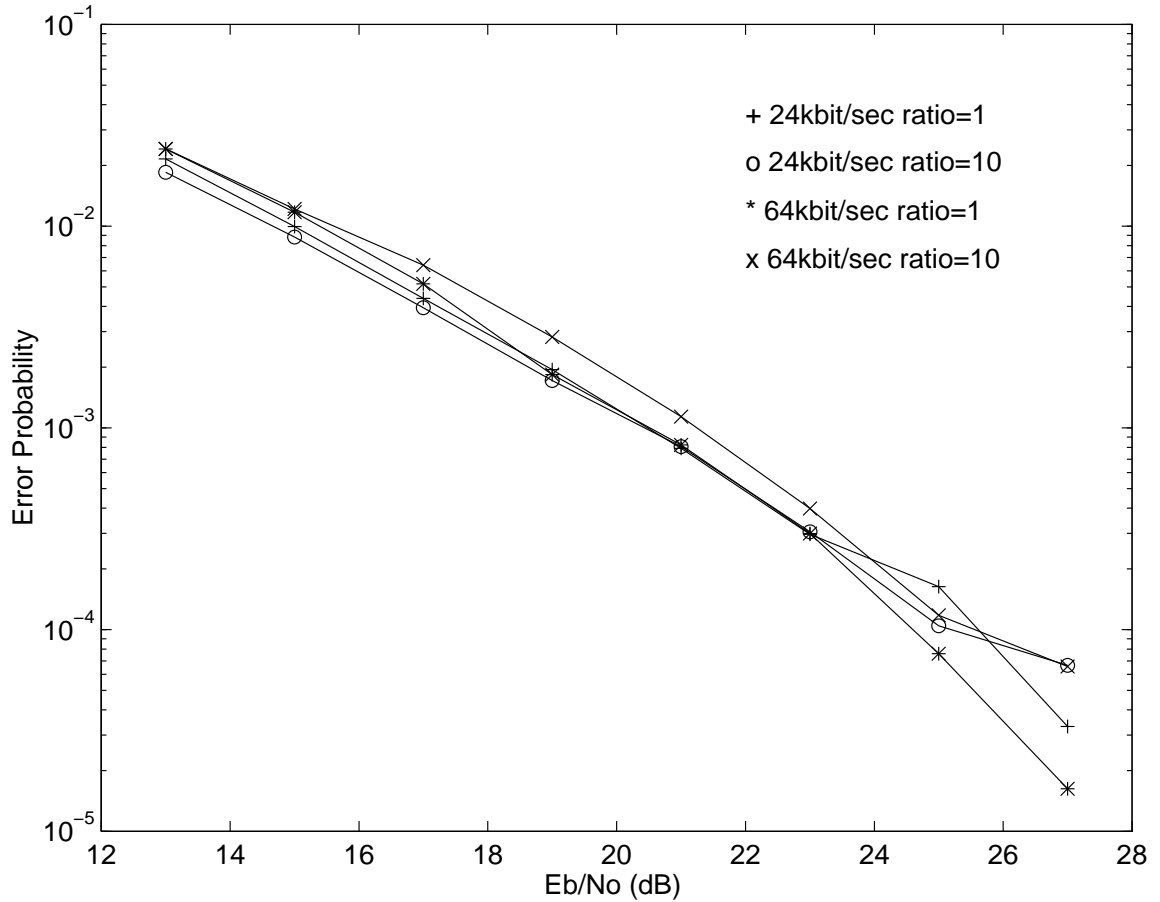


Figure 3.30: Coded TCM performance for 24 kbit/s and 64 kbit/s video over two-ray Rayleigh frequency-selective fading channel, perfect channel state information, ratio is first ray energy divided by second ray energy. Normalized fading bandwidth at 0.0077 and 0.00286 respectively, and 3 pilot symbols are inserted every 9 data symbols.

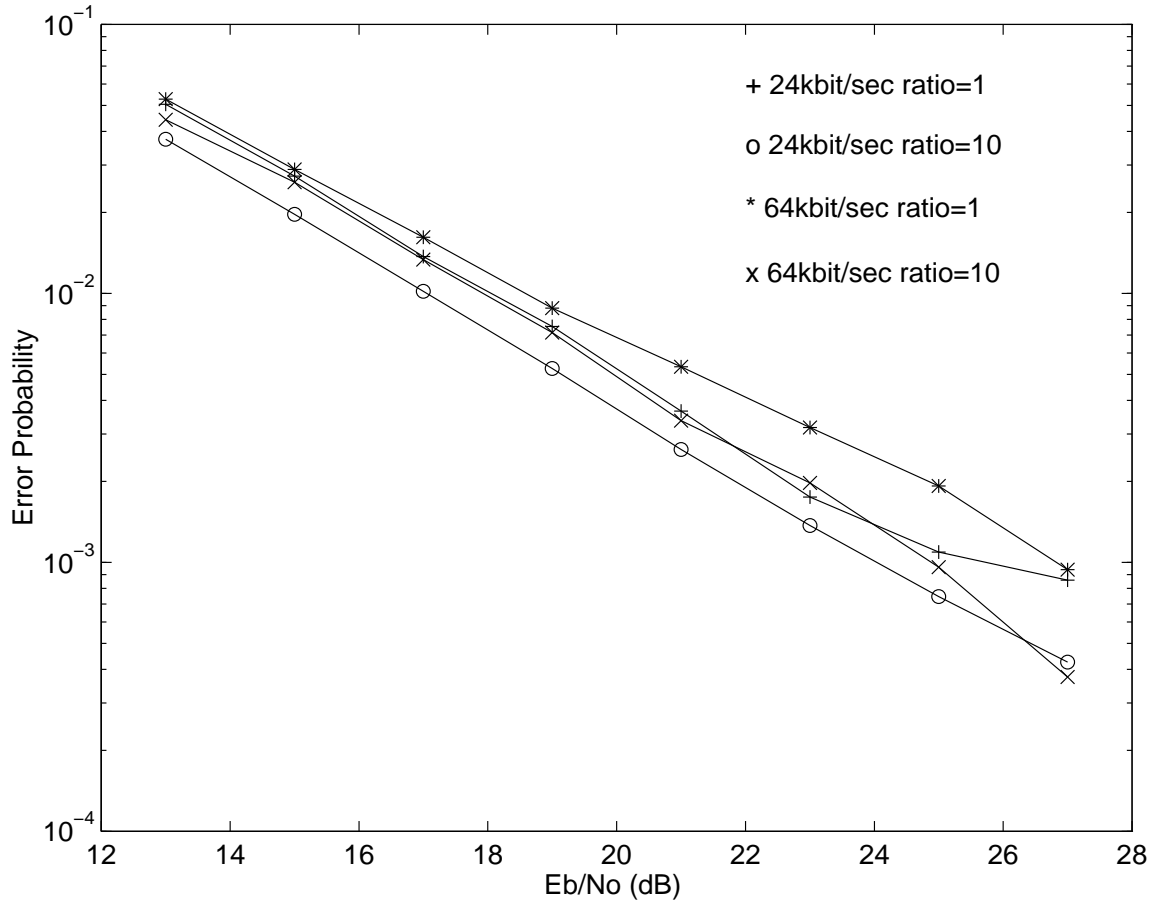


Figure 3.31: Coded TCM performance for 24 kbit/s and 64 kbit/s video over two-ray Rayleigh frequency-selective fading channel, pilot channel state estimation, ratio is the first ray energy divided by the second ray energy. Normalized fading bandwidth at 0.0077 and 0.00286 respectively, and 3 pilot symbols are inserted every 9 data symbols.

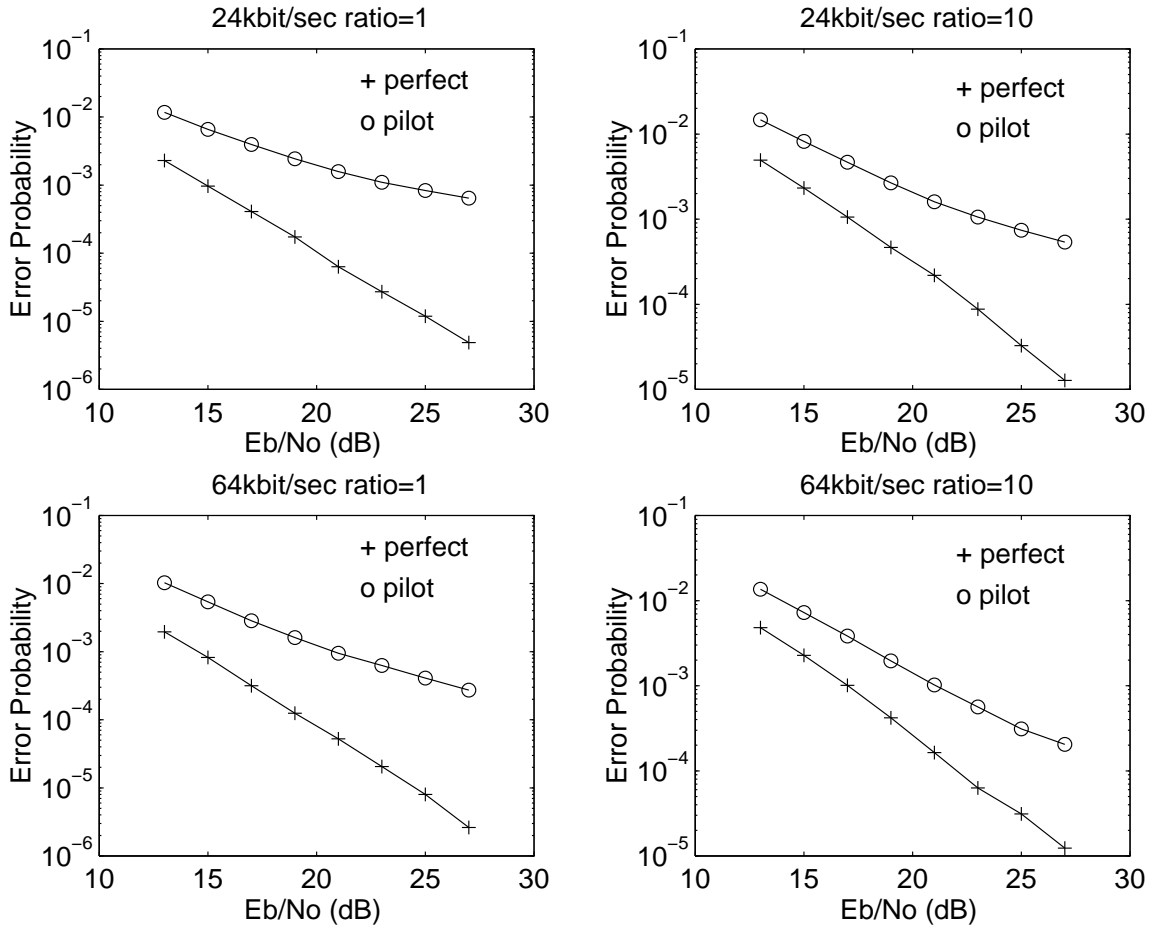


Figure 3.32: Uncoded QPSK performance for 24 kbit/s and 64 kbit/s video over two-ray Rayleigh frequency-selective fading channel with perfect channel state information and with pilot channel state estimation, ratio is the first ray energy divided by the second ray energy. Normalized fading bandwidth at 0.0077 and 0.00286 respectively, and 3 pilot symbols are inserted every 9 data symbols.

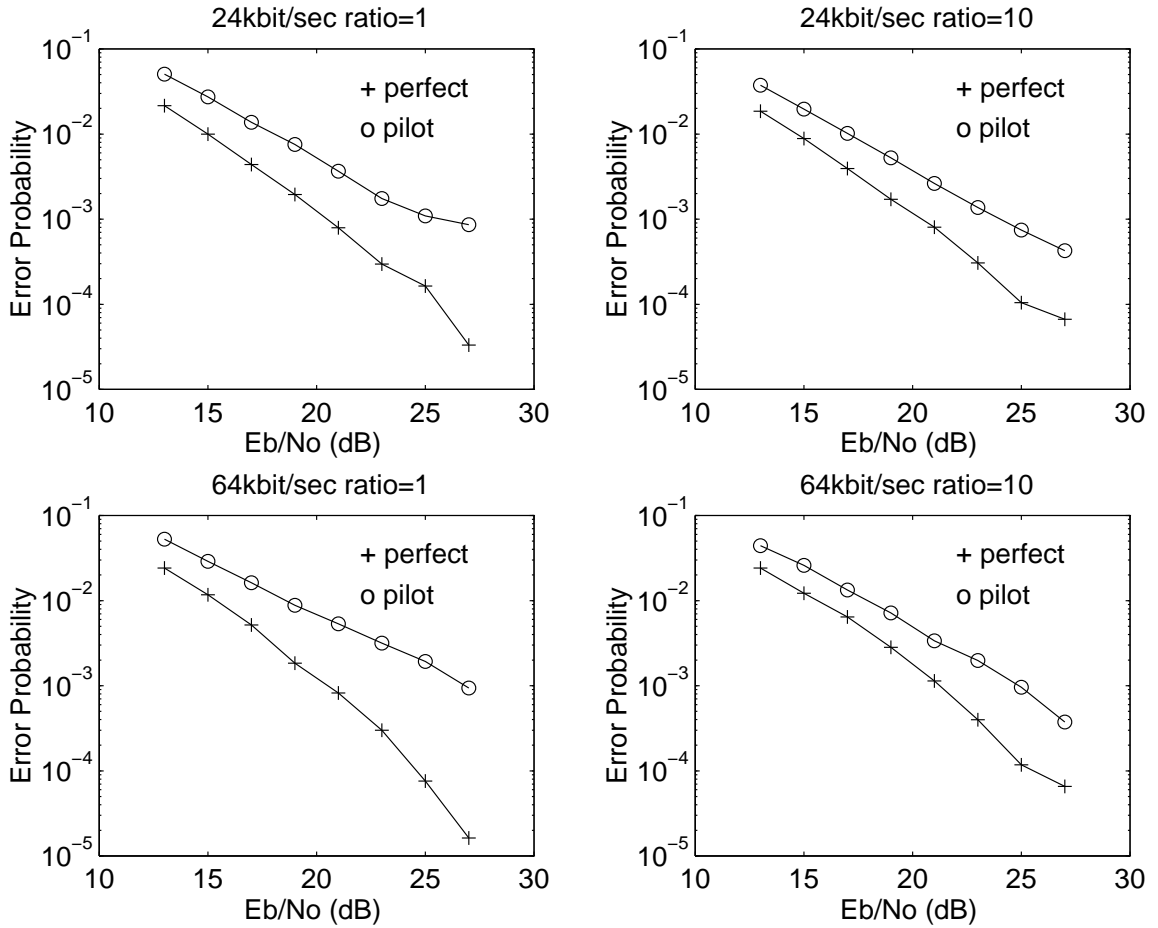


Figure 3.33: Coded TCM performance for 24kbit/s and 64kbit/s video over two-ray Rayleigh frequency-selective fading channel with perfect channel state information and with pilot channel state estimation, ratio is the first ray energy divided by the second ray energy. Normalized fading bandwidth at 0.0077 and 0.00286 respectively, and 3 pilot symbols are inserted every 9 data symbols.

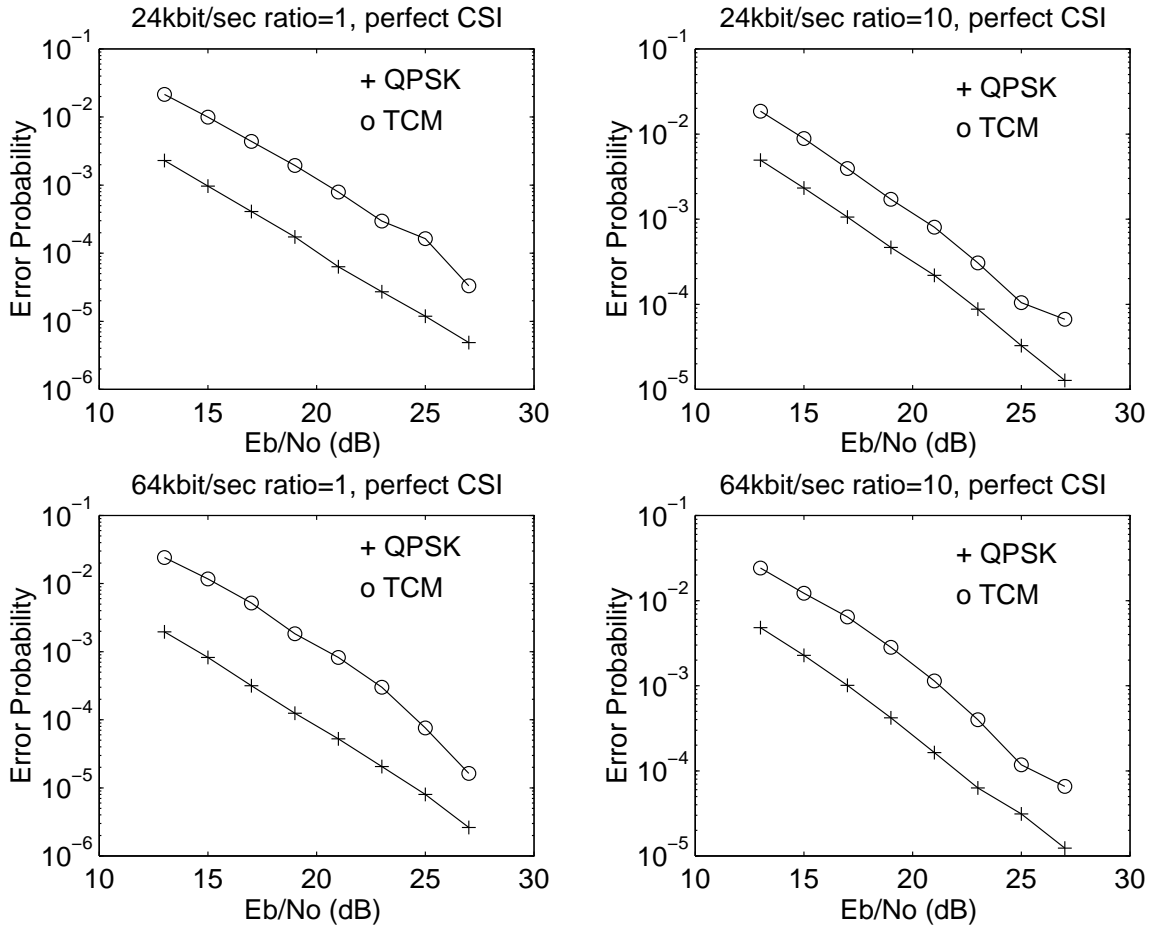


Figure 3.34: Uncoded QPSK and coded TCM performance for 24kbit/s and 64kbit/s video over two-ray Rayleigh frequency-selective fading channel with perfect channel state information, ratio is the first ray energy divided by the second ray energy. Normalized fading bandwidth at 0.0077 and 0.00286 respectively, and 3 pilot symbols are inserted every 9 data symbols.

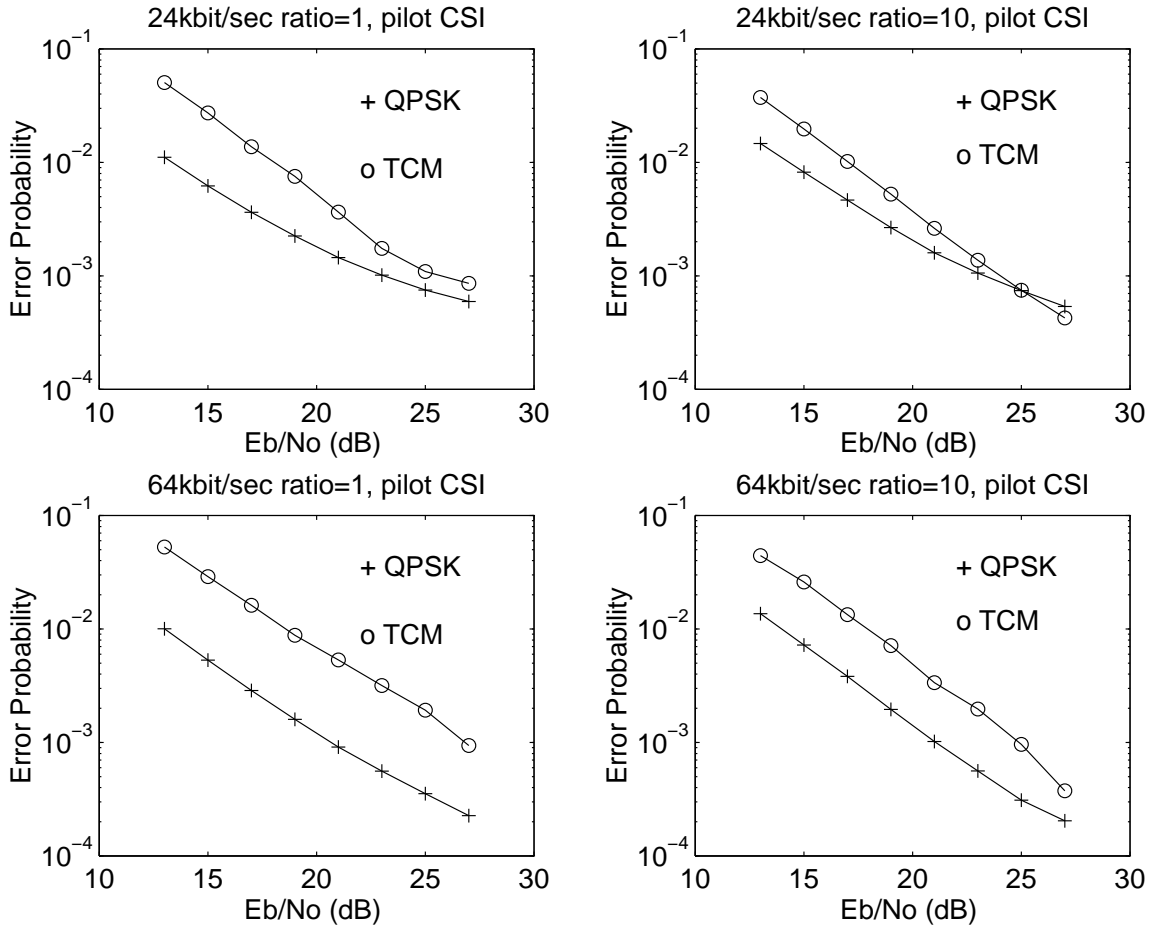


Figure 3.35: Uncoded QPSK and coded TCM performance for 24kbit/s and 64kbit/s video over two-ray Rayleigh frequency-selective fading channel with pilot channel state estimation, ratio is the first ray energy divided by the second ray energy. Normalized fading bandwidth at 0.0077 and 0.00286 respectively, and 3 pilot symbols are inserted every 9 data symbols.

error channel and does not have optimal performance over fading channels. Inner interleaving cannot be used to improve the system performance because of the selectivity property of the channel. The more dense 8-PSK signal constellation also contributes to the 8-PSK TCM's poorer performance compared to QPSK modulation.

3.7.3.3 Comparison of two different receiver structures for frequency-selective channels: one-ray receiver and two-ray receiver

In this section, two different receiver structures are studied and tested for 2-ray frequency-selective channels. One receiver structure is designed for frequency-nonselective (one-ray) channels. Another one is designed for two-ray frequency-selective channels. In the simulation, one pilot symbol is inserted every nine data symbols for the one-ray receiver. For the two-ray receiver, three pilot symbols are inserted every nine data symbols. Thus, the one-ray receiver has 11.11% bandwidth expansion for pilot symbols and two-ray receiver has 33.33% bandwidth expansion.

Figures 3.36 and 3.37 show that the one-ray receiver is outperformed by the two-ray receiver when the two ray energy ratio is between 0 - 20 dB, but the one-ray receiver is superior when the two-ray energy ratio is large enough. This cross-over value is between 15 - 30 dB. This is explained by the fact that interleaving cannot be used in a 2-ray receiver. Thus a 2-ray receiver cannot take advantage of TCM. A second observation is that the performance of the 2-ray receiver gets worse as the energy ratio increases. This phenomenon is due to the difficulty in both estimating the weak ray and in the loss of diversity.

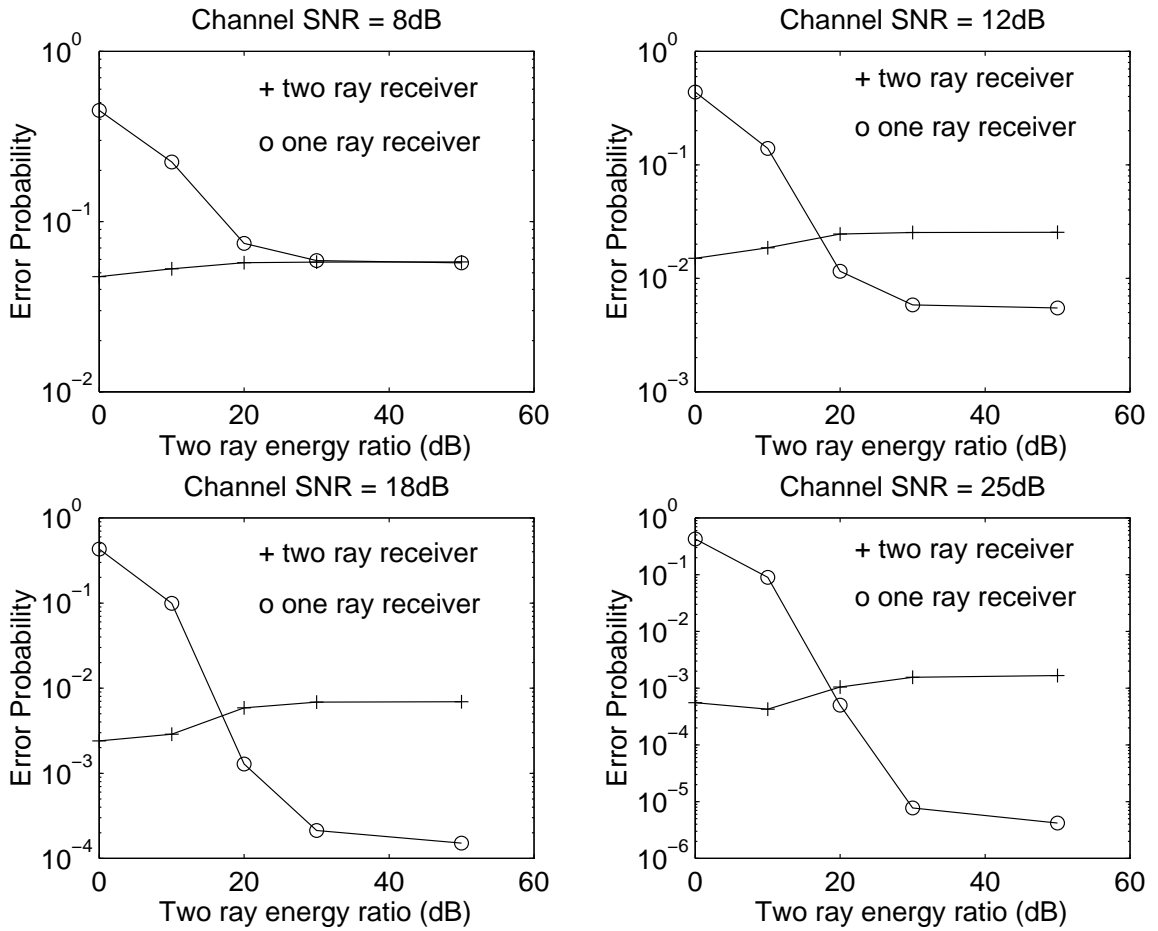


Figure 3.36: Two-ray receiver (Uncoded QPSK) and one-ray receiver (coded TCM with interleaving) performance over two-ray Rayleigh frequency-selective fading channel with pilot channel state estimation, ratio is the first ray energy divided by the second ray energy in dB. Normalized fading bandwidth at 0.0057.

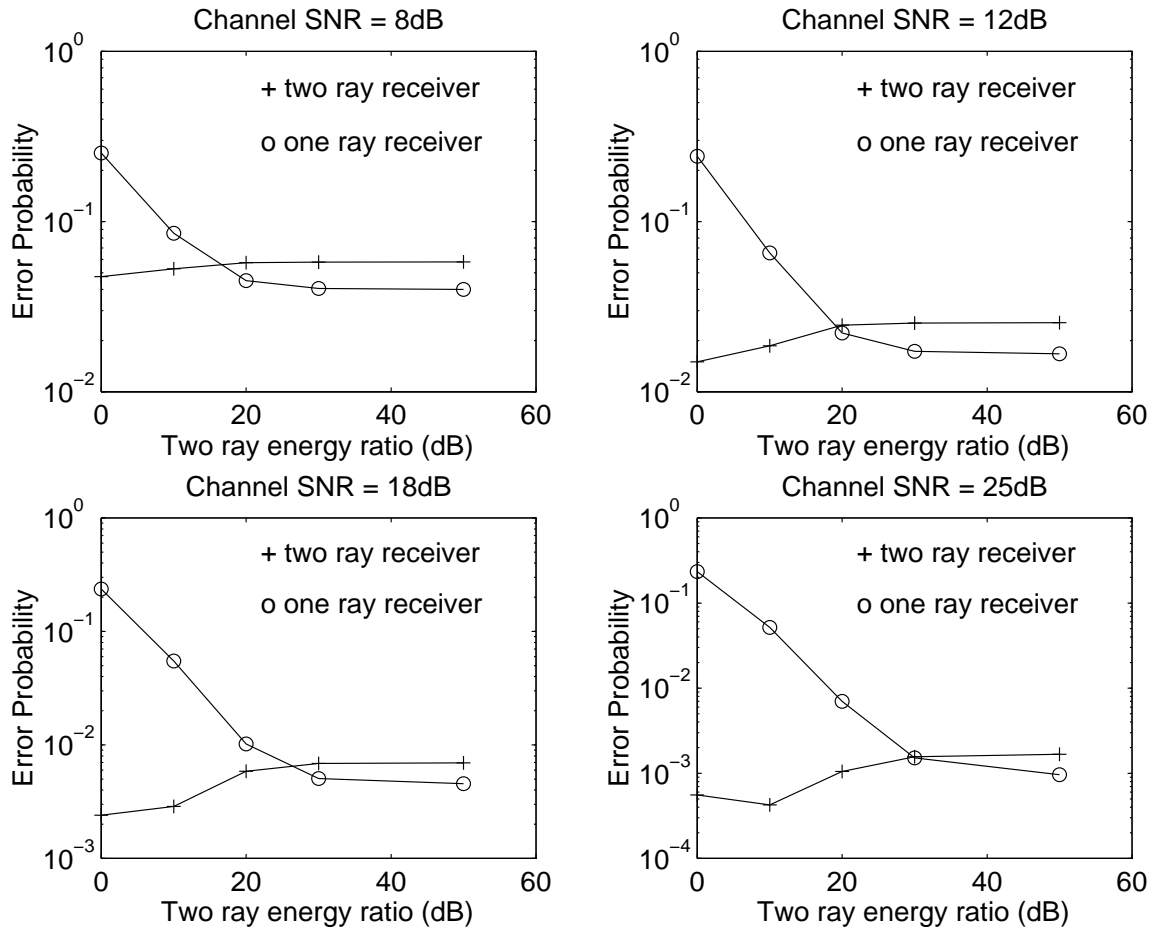


Figure 3.37: Two-ray receiver (Uncoded QPSK) and one-ray receiver (Uncoded QPSK without interleaving) performance over two-ray Rayleigh frequency-selective fading channel with pilot channel state estimation, ratio is the first ray energy divided by the second ray energy in dB. Normalized fading bandwidth at 0.0057.

Chapter 4

3-D Subband Video Transmission through Mobile Channels

4.1 Subband coding

While the H.261 and H.263 standards mainly focus on motion compensated block transform coding, subband coding is an alternative compression method. As described in Chapter 2, subband coding takes direct advantage of the human visual system's temporal and spatial frequency response. 3-D subband coding possesses the desirable property of scalability and multiresolution [35]. Subband coding algorithms are capable of producing one compressed full resolution video bit stream with various substreams corresponding to different resolutions/rates of the same video sequence which can support multiple decoder display formats and a wide, finely scaled range of bit rates. Adaptive bit allocations can be implemented in different frequency bands. Using fixed-rate spatial and temporal subband compression, when combined with vector quantization, results in more robust video transmission with respect to channel error than the variable rate hybrid H.261 and H.263 standards. However, subband coding requires more bandwidth than hybrid coding. In this Chapter, we propose a new scheme that employs three-dimensional subband video transmission through a mobile satellite channel. This scheme is bandwidth scalable, more error resilient, and requires no forward error correction.



(a)



(b)

Figure 4.1: Original images (a) Lenna (b) Susie

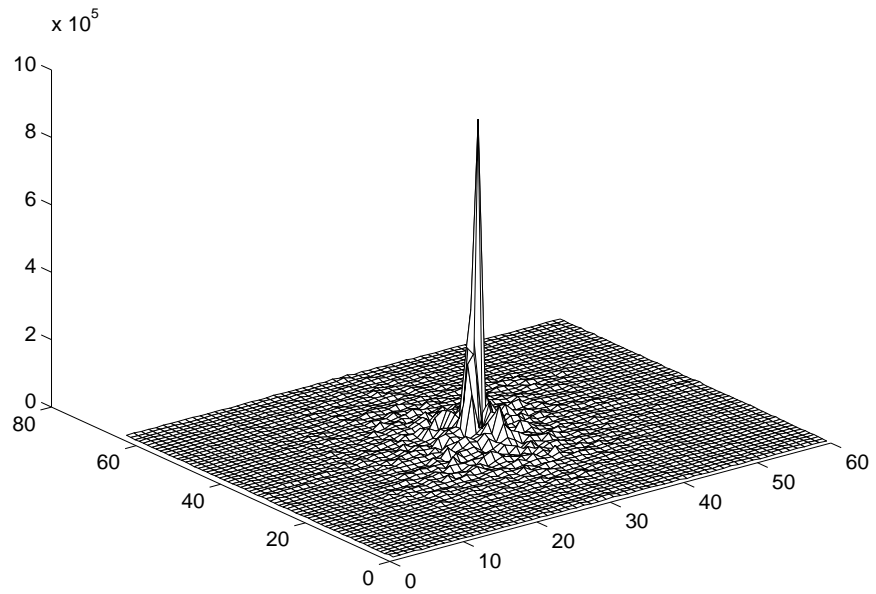
4.1.1 Frequency spectrum of sample images

In practice one often encounters video signals with energy dominantly concentrated in a particular region of frequency. For example, Figure 4.1 shows original “Lenna” and “Susie” images. Figure 4.2 shows the frequency spectrum of (a) lenna, and (b) Susie images. We can see that most of the signal energy is contained in the low horizontal and vertical frequency bands. It is therefore possible to compress the video by subband filtering. It is more common, however, to encounter signals that are not strictly lowpass, but which still have dominant frequency bands. We can split the signal into two frequency bands by using an analysis bank. High frequency subbands usually have less energy than low frequency subbands and can thus be encoded with fewer bits than low frequency subbands.

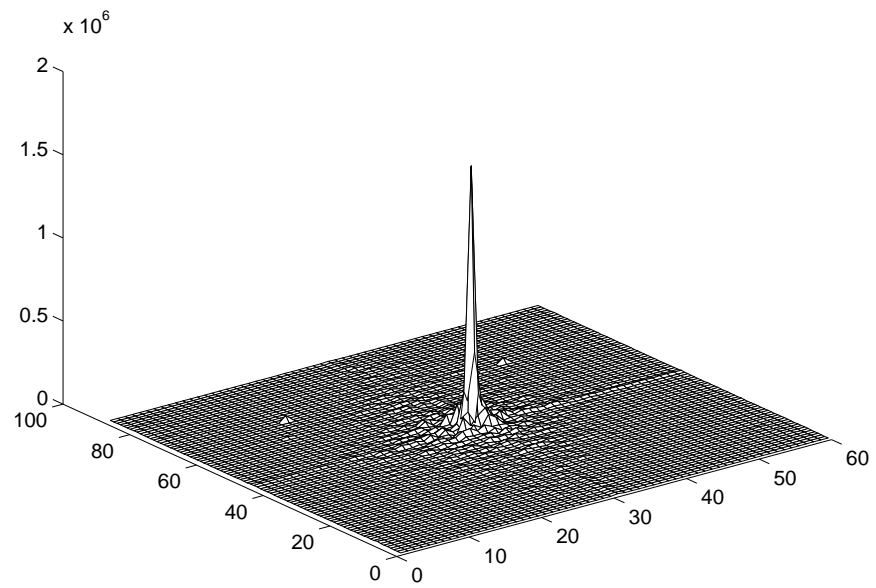
4.1.2 Analysis and Synthesis Filters

A decimated analysis filterbank is used to decompose full band images. The reconstruction of the full band signal is done using expanders and a synthesis filterbank as shown in Figure 4.3.

Figure 4.3 shows the Quadrature Mirror Filter (QMF) bank. The input signal $x(n)$ is first filtered by two filters $H_0(z)$ and $H_1(z)$, typically lowpass and highpass. Each

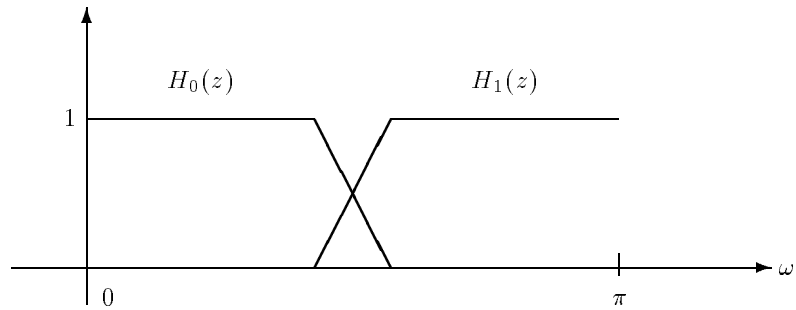


(a)

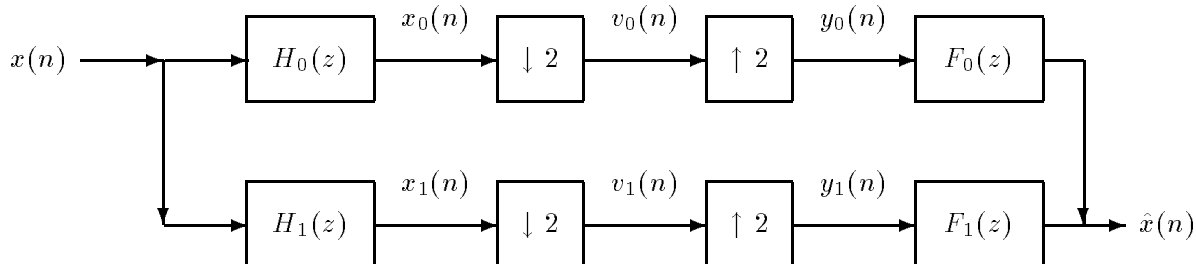


(b)

Figure 4.2: Frequency spectra of sample images (a) Lenna (b) Susie. Notice the lowpass nature of the spectra.



(a)



(b)

Figure 4.3: (a) Quadrature Mirror Filter (b) Subband Analysis and Synthesis Filterbanks

signal $x_k(n)$ (subband signal) is therefore approximately bandlimited. The subband signals are decimated by a factor of 2 to produce $v_k(n)$. Without loss of generality, we restrict the following discussion to the simple case of a two filter bank. Multifilter banks can be applied in a similar way [41]. Figure 4.3 only shows one stage of subband analysis and synthesis. Multistage and multilevel subband decomposition can also be implemented by applying analysis filters recursively. Figures 4.4 and 4.5 show subband analysis and synthesis trees, respectively. Figure 4.6 shows multilevel subbands arising from the analysis tree.

Each decimated signal $v_k(n)$ is then coded in such a way that the special properties

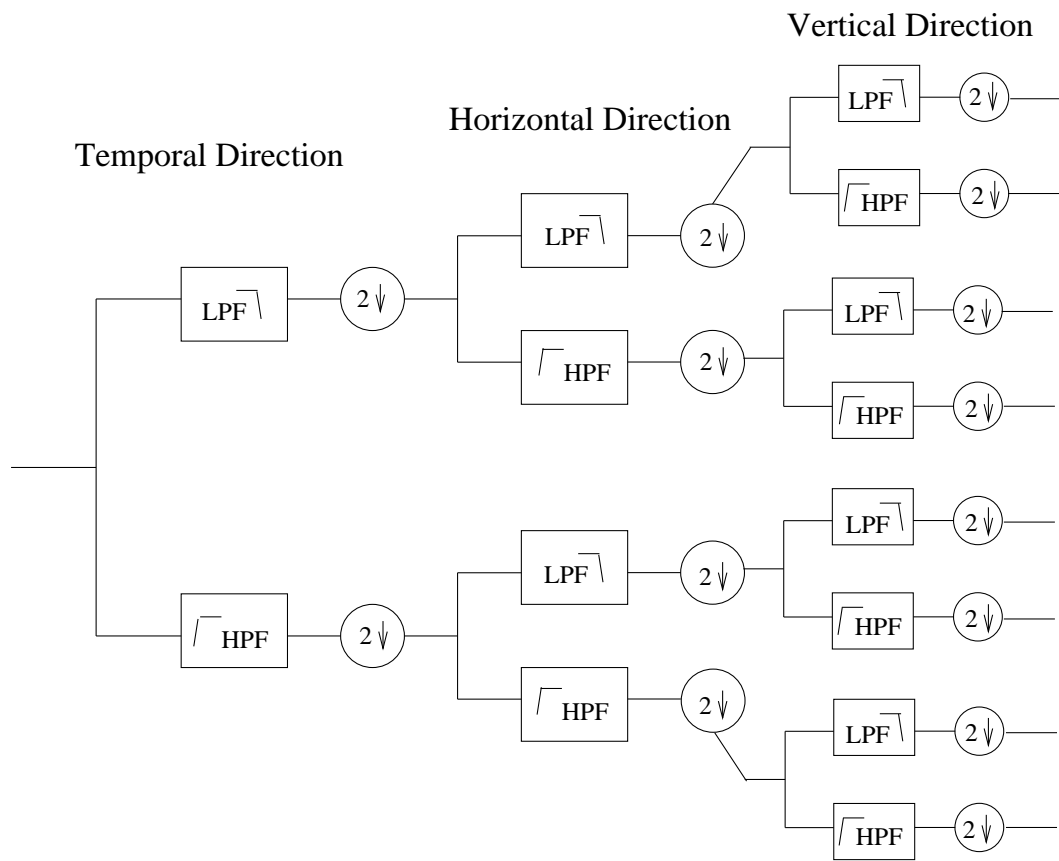


Figure 4.4: 3-D subband analysis tree

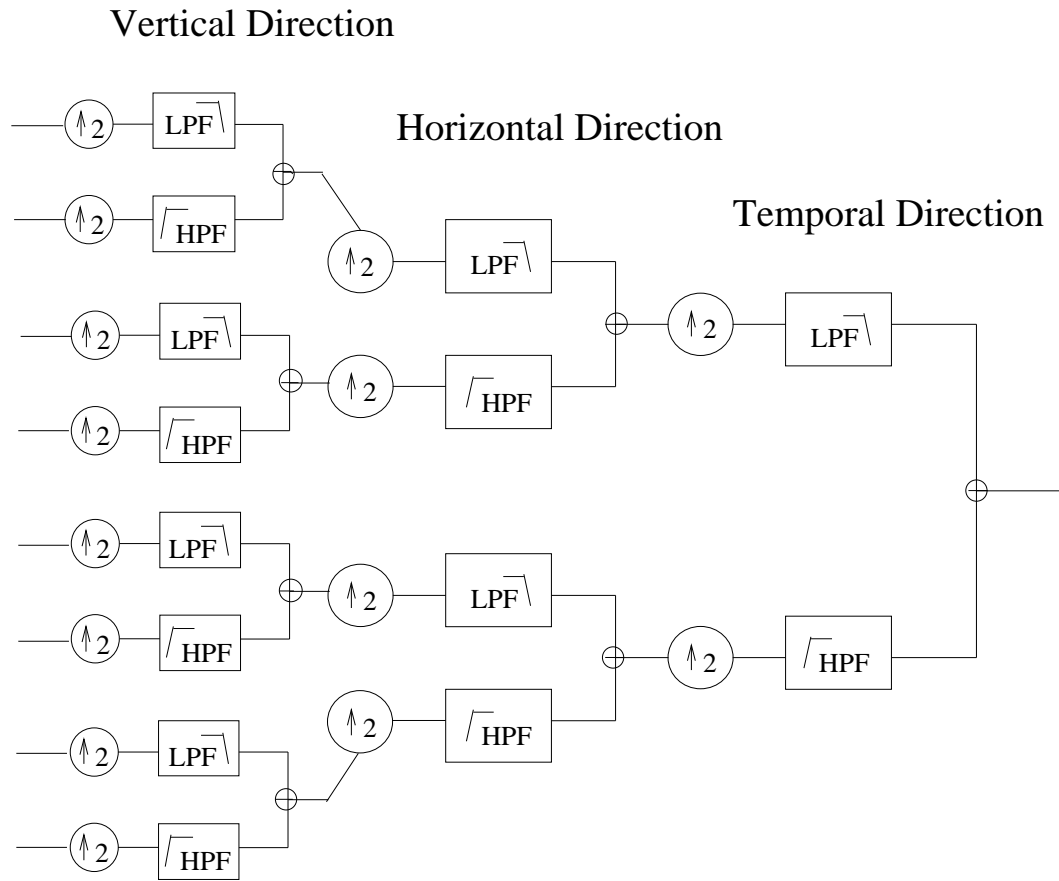
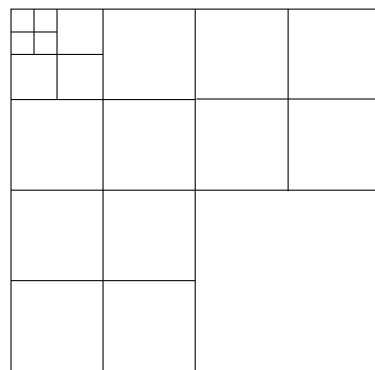
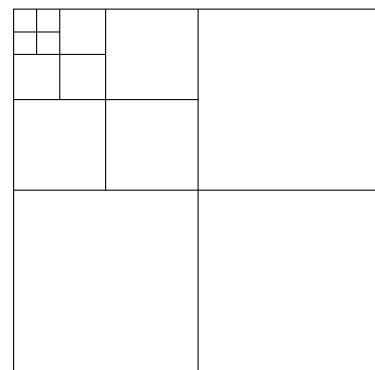


Figure 4.5: 3-D subband synthesis tree



Low frequency Temporal



High frequency Temporal

Figure 4.6: Multilevel subbands

of the subband (such as energy level, perceptive importance, and so on) are exploited. At the receiver, the signals are decoded to produce the signals $v_0(n)$ and $v_1(n)$ which are then passed through two-fold expanders. The output signals $y_0(n)$ and $y_1(n)$ are then passed through the filters $F_0(z)$ and $F_1(z)$ to produce the output signal $\hat{x}(n)$.

$H_0(z)$ and $H_1(z)$ are called analysis filters, and the pair $[H_0(z), H_1(z)]$ the analysis bank. This pair followed by the two decimators is the *decimated analysis bank*. Similarly, $F_0(z)$ and $F_1(z)$ are the synthesis (or reconstruction) filters, and the pair $[F_0(z), F_1(z)]$ the synthesis bank. If the channel is error free, the reconstructed signal $\hat{x}(n)$ differs for *four* reasons: aliasing, amplitude distortion, phase distortion, and coding/quantization distortion. It will be shown that the filters can be designed in such a way that the first three distortions are completely eliminated.

In practice, the analysis filters have nonzero transition bandwidth and stop band gain. The subband signals are therefore not bandlimited and their decimation results in aliasing. The reconstructed signal and the original signal are related as follows:

$$\hat{X}(z) = \frac{1}{2}[H_0(z)F_0(z) + H_1(z)F_1(z)]X(z) + \frac{1}{2}[H_0(-z)F_0(z) + H_1(-z)F_1(z)]X(-z) \quad (4.1)$$

It is clear from (4.1) that if the analysis and synthesis filters satisfy the condition

$$H_0(-z)F_0(z) + H_1(-z)F_1(z) = 0, \quad (4.2)$$

aliasing is cancelled. The following simple filter choice therefore cancels aliasing:

$$F_0(z) = H_1(-z), F_1(z) = -H_0(-z). \quad (4.3)$$

Substituting (4.3) into (4.1), the reconstructed signal can be expressed as

$$\hat{X}(z) = T(z)X(z), \quad (4.4)$$

where

$$T(z) = \frac{1}{2}[H_0(z)H_1(-z) - H_1(z)H_0(-z)] \quad (4.5)$$

is called the *distortion transfer function*, or “overall” transfer function of the alias-free system.

A system is said to be a perfect reconstruction (PR) system if the reconstructed signal $\hat{x}(n) = ax(n - n_0)$ for some constant $a \neq 0$ and integer n_0 . Now suppose $H_0(z)$ is power symmetric, that is $H_0(z)$ satisfies

$$\tilde{H}_0(z)H_0(z) + \tilde{H}_0(-z)H_0(-z) = 1 \quad (4.6)$$

where “tilde” stands for complex conjugation. In $\tilde{H}_0(z)$ notation, the coefficients of H_0 are conjugated and z is inverted. If the filter $H_1(z)$ is chosen as

$$H_1(z) = -z^{-N} \tilde{H}_0(-z) \quad (4.7)$$

then it follows from (4.3) that the synthesis filters are given by:

$$F_0(z) = z^{-N} \tilde{H}_0(z), \quad (4.8)$$

$$F_1(z) = z^{-N} \tilde{H}_1(z). \quad (4.9)$$

We note that with this choice of power symmetric filters, $T(z)$ in equation (4.5) becomes all-pass, and the system becomes PR. The above choices of filters can be expressed in the time domain as:

$$h_1(n) = (-1)^n h_0^*(N - n) \quad (4.10)$$

$$f_0(n) = h_0^*(N - n) \quad (4.11)$$

$$f_1(n) = h_1^*(N - n). \quad (4.12)$$

For signal compression applications, the design of optimal perfect reconstruction (PR) QMFs should consider several other parameters in addition to aliasing and in-band distortion. These parameters specify energy compaction, aliasing energy, unit step response, zero-mean high-pass filter, uncorrelated subband signals, constrained nonlinear phase response, and input source statistics. The parameters are combined to define the objective function of an optimization problem. We will discuss the aliasing energy problem. In principle, the PR QMFs eliminate aliasing. However, in practice, since not all the decomposition bands or coefficients are used in the synthesis, or because of different levels of quantization in the subbands, noncancelled aliasing

energy components exist in the reconstructed signal regardless. Thus, the optimal solution should minimize this aliasing energy component. Three important criteria are now described in more detail:

- **Step Response:** The representation of edges in images is a crucial problem. The edge structures are localized in time; therefore, they should be represented by time-localized basis functions. Otherwise, the ringing artifacts occur in encoded images. An edge can be crudely considered as a step. Therefore, the step responses of the low-pass filter in the filter bank should be considered during the design procedure.
- **Zero-Mean High-Pass Filter:** Most of the energy of practical signal sources is concentrated around the DC frequency. Therefore, practical signal decomposition techniques should be able to represent the DC component with only one basis function. Following this argument, we should constrain the high-pass QMF impulse response to have zero mean.
- **Uncorrelated Subband Signals:** Any good signal decomposition technique of coding applications should provide uncorrelated transform coefficients or subband signals for maximum coding gain (compression). The cross-correlation of the two subband signals should be minimized.

Details of filters designed according to these criteria can be found in [2].

4.1.3 Optimum Bit Allocation For Frequency Bands

The two-dimensional version of optimum subband bit allocation based on minimizing the average mean square reconstruction error of the image [2] is given by

$$B_{ij} = B + \frac{1}{2} \log_2 \frac{\sigma^2(i, j)}{[\prod_{ij} \sigma^2(i, j)]^{1/N^2}}, \quad (4.13)$$

where B_{ij} is the bit rate for the ij th subband, B is the average bit rate for the whole image, and $\sigma^2(i, j)$ is the variance of the ij th subband.

4.2 Pyramid Lattice Vector Quantizer (PVQ)

Fisher [14][15] first introduced PVQ as a fast method of encoding Laplacian-distributed independent and identically distributed (i.i.d.) vectors and later applied this technique to encoding high frequency DCT coefficients, which can be approximated by the Laplacian distribution. PVQ involves grouping data into L -dimensional vectors, mapping these vectors onto an L -dimensional pyramid structure as shown in Figure 4.7, and finding the nearest lattice point on this pyramid. The lattice points on the pyramid form the PVQ codebook, and each lattice point is assigned a binary codeword index. Since the pyramid structure is regular, encoding and decoding can be performed with simple computations and minimal memory look-up. This eliminates the need for codebook storage and training found in LBG-based VQ designs and allows for very large codebooks without being restricted by physical memory size. Furthermore, the computational complexity for both encoding and decoding depends linearly on the vector size, not exponentially as with the encoding required for most LBG-based VQ schemes. This allows for real-time encoding and decoding, making PVQ a practical and effective method of quantizing image data at video rates.

The pyramid shape can be derived using the asymptotic equipartition principle (AEP) from information theory. If the vector data are i.i.d. and have Laplacian distributions, the AEP implies that for a large vector dimension, L , almost all vectors will fall in an equiprobable L -dimensional pyramid surface.

Based on the geometric structure of a Laplacian source [14], let X_i be a sequence of i.i.d. Laplacian random variables with pdf:

$$p_x(x_i) = \frac{\lambda}{2} e^{-\lambda|x_i|} \quad (4.14)$$

The sequence X_i is assembled into vectors X of length L , with a resulting density

$$f_x(x) = \prod_{i=1}^L p_x(x_i) \quad (4.15)$$

A contour of constant probability density is specified by the condition

$$r = \sum_{i=1}^L |X_i| = \|X\|_1 = \text{constant} \quad (4.16)$$

where $\|X\|_1$ is the familiar l_1 norm. Let $S(L, K)$ be defined as:

$$S(L, K) = \{X : \sum_{i=1}^L |X_i| = K\} \quad (4.17)$$

Geometrically, $S(L, K)$ is the surface of a hyperpyramid in L -dimensional space.

The scalar random variable r indexes a particular contour of constant density $f_x(x)$ or, equivalently, the pyramid $S(L, K)$. The pdf of r is given by:

$$p_r(r) = \frac{\lambda^L r^{L-1} e^{-\lambda r}}{\Gamma(L)} \quad (4.18)$$

Defining:

$$\rho = \frac{r}{L} \quad (4.19)$$

as the per dimension l_1 norm of X , it can be shown that

$$E[r] = \frac{L}{\lambda}, \quad (4.20)$$

$$\text{var}[r] = \frac{L}{\lambda^2}, \quad (4.21)$$

$$E[\rho] = \frac{1}{\lambda}, \quad (4.22)$$

and

$$\text{var}[\rho] = \frac{1}{L\lambda^2}. \quad (4.23)$$

For large L , using (4.20), the vector X becomes highly localized around the particular contour of constant density, r , given by $r = L/\lambda$ [14]. For each vector X let \hat{X} be the closest vector (mean absolute error criterion) on $S(L, L/\lambda)$. Then:

$$E \left\{ \frac{1}{L} \|X - \hat{X}\|_1 \right\} = E|\rho - E(\rho)| = \frac{2L^L e^{-L}}{\lambda \Gamma(L+1)} \quad (4.24)$$

The vector \hat{X} can be computed from the well-known projection theorem. Let vector $S(X)$ have components:

$$S_i = \begin{cases} 1, & \text{if } X_i > 0 \\ 0, & \text{if } X_i = 0, \text{ if } \|X\|_1 \geq L/\lambda, \\ -1, & \text{if } X_i < 0 \end{cases} \quad (4.25)$$

or:

$$S_i = \begin{cases} 1, & \text{if } X_i \geq 0 \\ -1, & \text{if } X_i < 0, \text{ if } \|X\|_1 < L/\lambda, \end{cases} \quad (4.26)$$

The two cases correspond to X being either on or outside, or inside the pyramid, respectively. The vector on the pyramid $S(L, L/\lambda)$ that is closest to X can be computed as:

$$\hat{X} = X - \left[\left(X, \frac{S}{\|S\|_2} \right) - \frac{L\|S\|_2}{\lambda\|S\|_1} \right] \frac{S}{\|S\|_2} \quad (4.27)$$

where (\cdot, \cdot) is the usual inner product and provided that:

$$S(X) = S(\hat{X}) \quad (4.28)$$

If the result yields a vector \hat{X} that does not satisfy the last equation, corresponding to X being “above” a corner or out of the pyramid, then all the components of X that fail should be set to zero and (4.25), (4.26), and (4.27) reapplied.

Since the probability density is constant along this geometric surface, the quantizer representation regions should tend to be distributed uniformly on the surface of the pyramid.

A PVQ can be constructed based on a subset of the points in the cubic lattice (that is, the set of all vectors with integer components). As such, the PVQ is a type of lattice quantizer, but it is not based on a uniform source pdf. Thus, the implementation can be quite simple.

If pyramid $S(L, L/\lambda)$ has $L/\lambda = K$ where K is a positive integer, the number of vectors with integer components that lie on $S(L, K)$ is:

$$N(L, K) = \left\{ \begin{array}{l} \text{the number of vectors } x \text{ such that} \\ \sum_{i=1}^L |x_i| = K, \text{ and } x_i \text{ an integer, for } i=1, \dots, L \end{array} \right\} \quad (4.29)$$

A source encoding procedure for an i.i.d. Laplacian vector X is as follows:

- Choose L, K constrained by the data rate R (bits/pixel), so that:

$$N(L, K) \leq 2^{RL} \quad (4.30)$$

- Form the L dimensional vector X

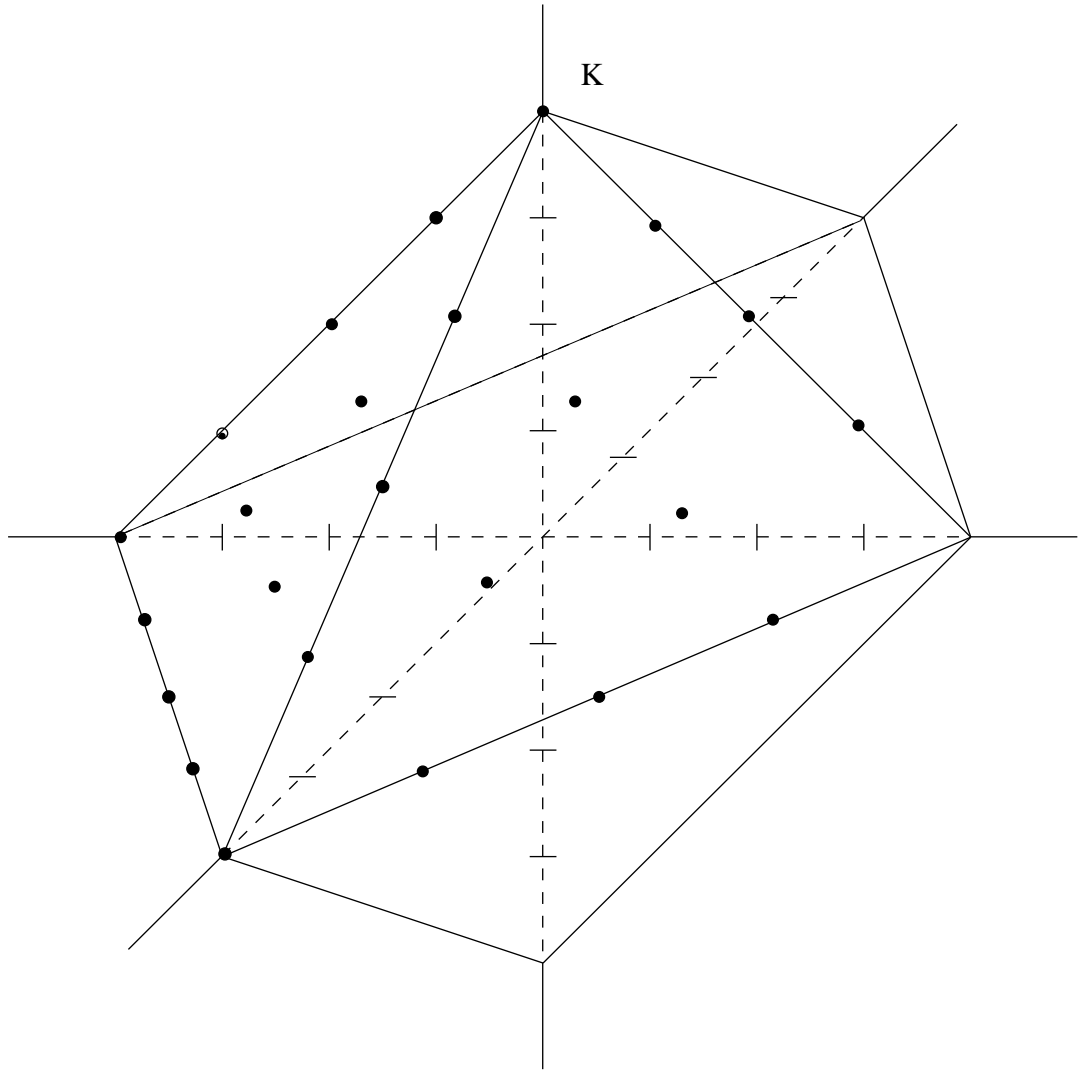


Figure 4.7: Integer lattice points on a 3-D pyramid of “radius” $K=4$

- Form $\hat{X} \in S(L, L/\lambda)$
- Scale \hat{X} by $K\lambda/L$ to obtain a corresponding point, \tilde{X} on $S(L, K)$
- Find the closest of the $N(L, K)$ integer component vectors on $S(L, K)$ to \tilde{X} .
 - Round each component of \tilde{X} to the nearest integer; call the resulting vector \tilde{y}
 - Check if $\|\tilde{y}\|_1 = K$ and make adjustment; denote the resulting vector as \hat{y}
- The vector quantizer representation point is $y = (\frac{L}{\lambda})\hat{y}/K$.

4.2.1 A Product Code PVQ

Subband coefficients of real images, although roughly Laplacian in nature, are far from being independent and identically distributed. As a result, most image vectors land far from the assumed pyramid surface. Fisher proposed a product-code PVQ method of mapping vectors on to the pyramid surface. Figure 4.8 shows the concept of a product code.

For a moderately sized dimension, significant distortion may be introduced in approximating X by $\hat{X} \in S(L, L/\lambda)$. A general VQ design can be based on concentric pyramids. That is, a single pyramid VQ is designed for a normalized vector with $2^{R_p L}$ output points, and a scalar quantizer designed for r with 2^{R_r} output levels. The total rate per dimension R to encode a vector is the sum of the PVQ average rate per dimension R_p and the scalar quantizer rate R_r :

$$R_p L + R_r = RL \quad (4.31)$$

If $\hat{Y} = PVQ(\hat{X})$ is the pyramid quantizer output and $\hat{r} = Q(r)$ the scalar quantizer output, then the product code output is $Y = \hat{r}\hat{Y}$.

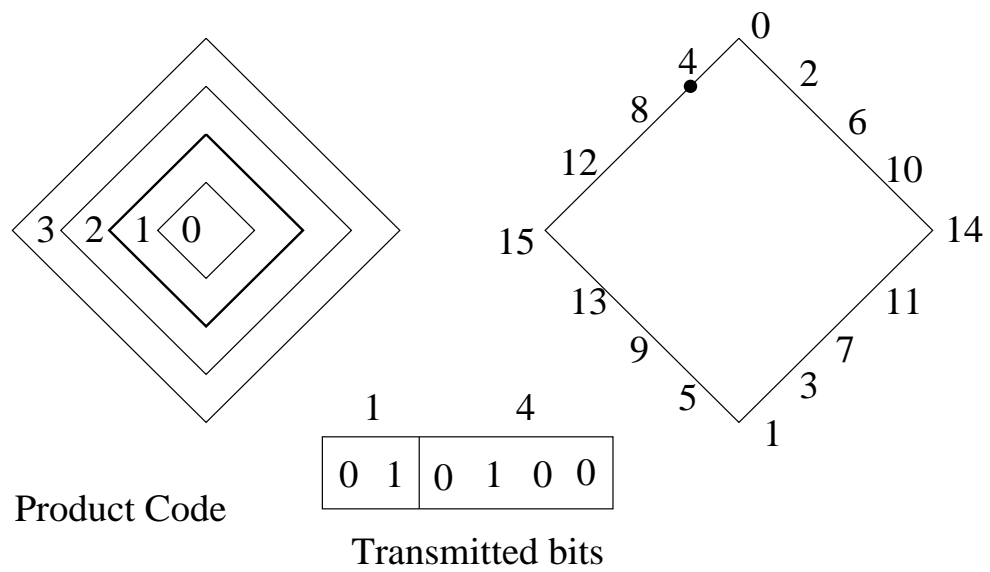


Figure 4.8: The distribution of information in the product enumerated PVQ index

4.3 3-D Subband Coding Using PVQ

4.3.1 Introduction

Pyramidal vector quantization (PVQ), with its robust fixed-rate property, has been applied to two-dimensional (2-D) image coding [29]. In this thesis, we extend the PVQ scheme to three-dimensional (3-D) subband video coding and apply it to shadowed mobile satellite channels that are modelled as described in Section 2.2.5. The objective of our study is to reduce or eliminate the need for FEC and interleaving that were described in Chapter 3.

Our proposed image/video transmission system utilizes 3-D subband video coding, combined with pyramidal vector quantization (PVQ) and adaptive bit allocation within subbands for source coding. Bandwidth efficient 8-state 8-PSK (phase shift keying), interleaving, trellis-coded modulation (TCM) and Viterbi decoding, described in Chapter 3, are used for channel coding and receiver modeling. A detailed computer simulation of the transmission system has been developed, and results from video image sequence tests demonstrate that our proposed system has efficient image compression, error resilience to channel fading, and minimum system delay and complexity. Since the modulation is coherent, either the pilot symbol aided algorithm or the low delay DFALP algorithm (see Section 3.2.3) is needed to estimate fading channel state information. DFALP uses linear prediction to track the fading channel state information, and this reduces the estimation delay. Figure 4.9 shows the system block diagram.

The details of the above transmission scheme are presented in Chapter 3, except that forward error correction and outer interleaving are eliminated here. This also reduces signal processing complexity and transmission delay. Compared to the variable length source coding used in H.261 and H.263, fixed length subband coding and pyramidal vector quantization are less sensitive to channel errors.

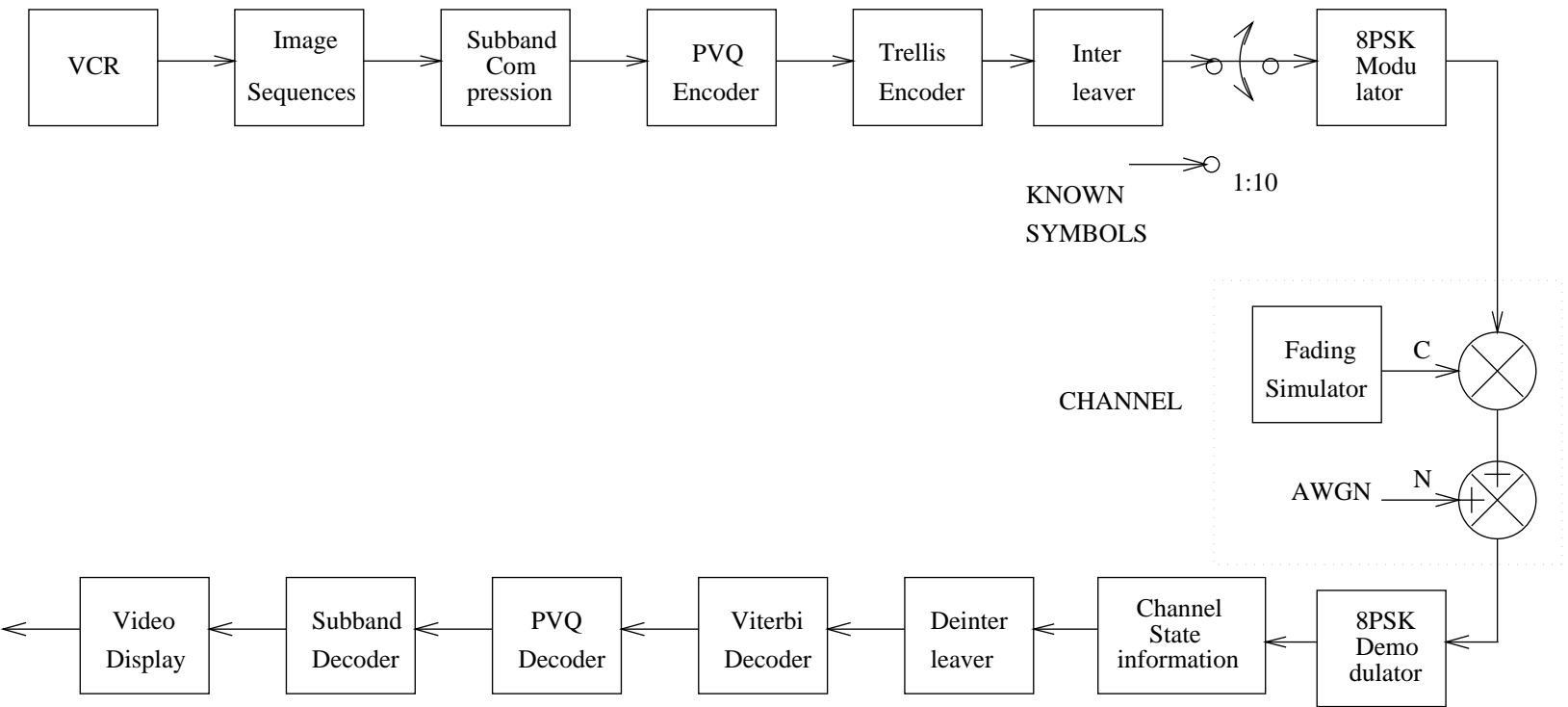


Figure 4.9: System block diagram for 3-dimensional subband scheme

Table 4.1: Example of 9-tap quadrature mirror filter coefficients

Coefficient	LPF	HPF
$h(0)$	0.5645751	0.5645751
$h(-1), h(1)$	0.2927051	-0.2927051
$h(-2), h(2)$	-0.05224239	-0.05224239
$h(-3), h(3)$	-0.04270508	0.04270508
$h(-4), h(4)$	0.01995484	0.01995484

Table 4.2: Optimal PR QMF filter coefficients based on energy compaction with zero mean high-pass filter

n	0	1	2	3
h(n)	0.317976535	0.748898833	0.534939876	-0.058836349
n	4	5	6	7
h(n)	-0.205817322	0.042523091	0.060007692	-0.025478793

Table 4.3: Example of integer coefficient PR QMF filter

h(n)	3	6	2	-1
------	---	---	---	----

4.3.2 3-D subband codec design

We now extend the 2-D subband coding and PVQ scheme of [29] to the 3-D case. The 3-D subband coder allows for adaptive bit allocation between temporal and spatial information. A 2-D subband coding software codec from Portable Video Research Group (PVRG) [29] is used, extended to 3-D and applied to the mobile satellite channel. In [29], every vector contains pattern, shape, and sign information in a manner which limits the effects of single bit errors and is much more robust to channel errors. We apply 3-D subband coding and the PVQ scheme to the above mobile satellite transmission system, which is described in detail in Chapter 3. Figure 4.10 shows the hierarchical subband decomposition. Temporal frequency decomposition is applied first with a 2-tap filter (Haar filter basis), which minimizes delay and error propagation through fading channels. Basically, the 2-tap filter decomposes 2 frames of video to average and difference signals. The tree-structured subband decomposition consists of two temporal subbands followed by a cascade of spatial subbands. There are more subband decompositions in the low temporal band than in the high temporal band and more bits are allocated to the low temporal band. The lowest spatial frequency band in the low temporal band uses scalar quantization. Since we have observed that the lowest spatial frequency band in the high temporal subband has a small variance and large mean, we subtracted the mean first and then applied scalar quantization. All the other bands use pyramidal lattice vector quantization.

As mentioned in Section 4.1.2, there are many criteria for choosing the spatial subband analysis quadrature mirror filters (QMF), such as energy compaction, aliasing energy, unit step response, zero-mean high-pass filter, uncorrelated subband signals, constrained nonlinear phase response, and hardware implementation complexity. We have tested several different separable QMFs based on these criteria and the results are discussed in Section 4.3.3. Tables 4.1, 4.2, and 4.3 show three designs of QMF coefficients used in our experiments. Table 4.1 is a symmetric QMF and Table 4.3 is an integer coefficient PR QMF filter.

FILTER	Susie(CIF)		Miss(CIF)	
	0.6bpp	0.47bpp	0.6bpp	0.47bpp
A	33.24	32.44	35.19	33.86
B	32.73	31.95	34.92	33.46
C	33.28	32.41	35.26	34.10
D	33.26	32.43	35.15	34.01
E	33.12	32.35	35.55	34.44
F	33.06	32.29	35.53	34.42
G	32.77	31.99	31.61	30.98

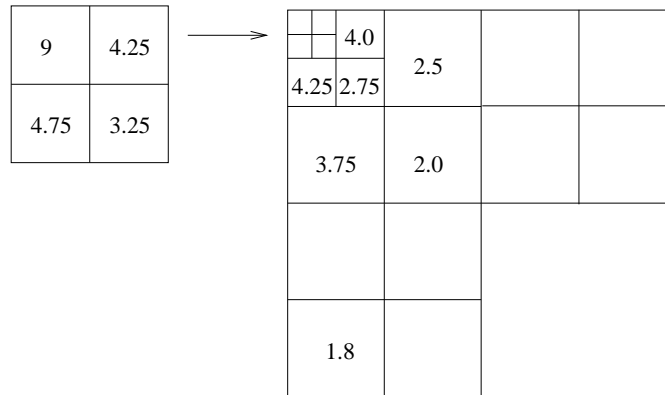
Table 4.4: PSNR performance using different filters

Comparing the 3-D subband and PVQ scheme to standard hybrid schemes such as H.261, described in Chapter 2, indicates that annoying block effects at low-bit rates are reduced, while the inherent high error-resiliency of the 3-D subband/PVQ eliminates the need for FEC, even through a channel that has a bit error rate in the vicinity of 10^{-3} . In contrast, the hybrid coded H.261 requires a bit error rate of less than 10^{-5} under the same channel conditions as in Chapter 3.

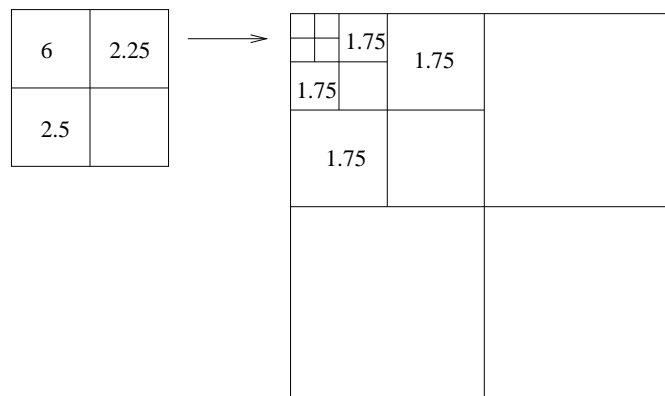
4.3.3 Results on video test sequences

Our preliminary “video-coded modem” simulation results involve video sequences transmitted through light shadowed and average shadowed mobile satellite channels using 2-D and 3-D subband PVQ without FEC. Sample results on luminance-component images can be found in Figures 4.11 and 4.12 for the 2-D and 3-D cases respectively. The 3-D case involved a 34-frame interlaced-scanned image sequence captured at 560×480 resolution at 30 frames/sec and subsampled to 10 frames/sec. The 2-D case is simply the first image chosen from the 34-frame sequence, which is typical of the sequence. Received frames 0, 3, 6, and 9 are shown in Figure 4.12. The channel SNR is 10.5 dB per bit in average shadowing, resulting in a channel bit

Low frequency Temporal



High frequency Temporal



Total 0.6bpp

Figure 4.10: Temporal and Spatial Subband Decomposition

VIDEO	2-D	3-D		H.263		
	0.6bpp	0.6bpp	0.47bpp	0.063bpp	0.095bpp	0.25bpp
Miss(QCIF)	31.73	33.88	32.23	36.66	37.95	39.82
Susie(QCIF)	30.29	32.14	30.49	31.46	33.16	36.28
Miss(CIF)	33.27	35.19	33.86			
Susie(CIF)	32.15	33.24	32.44			
Mark	31.38	32.23	31.31			

Table 4.5: PSNR performance at 0.6bpp and 0.47bpp for subband coding and performance of H.263 average over the sequences

error rate of 1.0×10^{-3} . Other video sequences including Miss_America and Susie at 352×288 (CIF), 176×144 (QCIF), and 10 frames/sec were also investigated. In the testing, the image compression was set to 0.6 bpp and 0.47 bpp. Table 4.4 shows the peak signal-to-noise ratio (PSNR) performance using different filters for the 3-D scheme, where

$$PSNR = 10 \log_{10} \left(\frac{256^2}{MSE} \right). \quad (4.32)$$

Filter A is a 9-tap symmetric separable QMF [1] as in Table 4.1. Filter B is a 4-tap integer-coefficient perfect reconstruction (PR) QMF as shown in Table 4.3. Filters C and E are, respectively, 12-tap and 6-tap PR QMFs based on energy compaction with a zero-mean high-pass filter [2]. Filters D and F are, respectively, 12-tap and 6-tap PR QMFs based on minimized inter-band aliasing energy with a zero-mean high-pass filter [2]. Filter G is the 8-tap Johnston QMF filter [2]. From Table 4.4, we can see the performances are similar for these different filters except in the case of the 4-tap filter and 8-tap Johnston filter. For reduced hardware complexity, the 4-tap integer-coefficient perfect reconstruction QMF can be used, but with a PSNR degradation of about 0.3 dB - 0.5 dB.

Table 4.5 compares the PSNR for the 3-D and 2-D cases using a 9-tap symmetric filter [1] and indicates the PSNR improvement using the 3-D subband scheme. This

is also borne out by a noticeable improvement in subjective quality in Figures 4.11 and 4.12. Using the same PSNR, the 2-D case requires 0.6 bpp, while the 3-D case only needs 0.40-0.48 bpp. It is observed from the 3-D scheme that the channel errors are spatially confined to isolated regions of the image, fine details are preserved, and blocking artifacts are not visible.

Source coding algorithm parameters were not optimized in the results presented. In our simulation, we used a fixed PVQ bit allocation scheme to compress different video sequences. For the “Susie” sequence, we have observed that a change in the lower temporal subband bit allocation from low horizontal/high vertical to high vertical/low horizontal subband yields improved results. Future issues include designing several different fixed bit-rate PVQ adaptive bit allocation tables to account for different subband variance distributions. Another issue involves incorporating motion compensation [33][49] to improve video compression performance, while maintaining low computational complexity.

Table 4.5 also shows PSNR and bits-per-pixel for 3-D subband and H.263 source coding. From this table, we can see that H.263 achieves a higher PSNR with a higher compression ratio. The PSNR’s are lower for “Susie” than the corresponding “Miss”. This is mainly due to the faster movement in “Susie” relative to “Miss”. H.263 achieves higher compression ratio in both sequences because it uses intra frame coding for all the frames except for the first. Also H.263 uses runlength and Huffman coding to achieve about ten times more overall compression. However, if any channel error occurs on one frame in H.263, the worst case is that it will propagate to the 49 remaining frames, even with H.263 forced updating. On the other hand, 3-D subband coding used fixed two-frame temporal compression. A channel error on one frame would at most affect two frames.

4.3.4 Conclusions

Our simulation results show that by using fixed-rate 3-D subband coding and pyramidal vector quantization, compressed video can be transmitted and recovered through

a mobile satellite channel with acceptable quality below 0.6 bpp and a channel bit error rate of 10^{-3} . The system delay and complexity are greatly decreased due to the elimination of the outer forward error correction and interleaving which are essential for H.261 and H.263 video transmission to combat fading channel bursty errors [43]. The elimination of inter-frame, runlength and Huffman coding also greatly simplifies the source coding algorithm and increases error resilience with the tradeoff of a higher bit-rate. Compared to the 2-D subband PVQ algorithm of [29], 1.0-2.0 dB PSNR improvement or, equivalently, 21-34% bit rate reduction can be achieved by the 3-D scheme.



Figure 4.11: Original (left) and 2-D subband PVQ coded Mark at 0.6 bpp (right), PSNR=31.3 dB, recovered from average shadowed mobile satellite channel, channel SNR=10.5 dB, BER= 10^{-3}



Figure 4.12: 3-D subband PVQ coding video sequences at PSNR=32.2 dB, 0.6 bpp, recovered from average shadowed mobile satellite channel during deep fading, channel SNR=10.5 dB, BER= 10^{-3}

Chapter 5

Summary and Conclusions

This chapter will summarize the material in the previous chapters. The motivation of this research is to propose and test the feasibility of a system for video image transmission through mobile satellite channels. Based on the extensive simulation results, the following conclusions can be made. Suggestions for further research are also discussed.

5.1 Summary of Contributions

1. A system was designed for the transmission of video over mobile satellite communication channels including trellis coded modulation (TCM), interleaving, forward error correction (FEC), channel signal-to-noise ratio (SNR), bandwidth and delay requirements. In the first part of the thesis, we utilized the existing video source coding standards H.261 and H.263. The system is specially designed for mobile satellite channels. Because of the very high compression of the video, the source is sensitive to channel errors due to variable length entropy coding. Outer forward error correction is required in the system to lower the channel SNR requirement. From our simulations, we find that video image transmission through mobile satellite channels is feasible with a channel SNR requirement of 9-12 dB under light and average shadowing. For this case,

the channel bandwidth is 15 kbd and 40.5 kbd for 24 kbit/sec and 64 kbit/sec video, respectively. Depending on different degrees of interleaving, the system delay varies from 89 ms to 1.546 s, depending on required SNR performance.

2. A variety of new and existing channel estimation schemes was compared in flat (frequency non-selective) fading. In this thesis, five different fading tracking algorithms are tested and compared. These five algorithms are:

- Pilot Symbol Aided (SA)
- Symbol Aided and Decision Directed (SADD)
- Decision Feedback with Adaptive Linear Prediction (DFALP)
- Kalman Filtering
- Multiple Model

From our simulation, we find that the performance of SA is close to the best for channel SNR less than 15 dB, which is a range of SNR of interest for noise-limited GEO satellite systems. Besides this, SA is also the simplest among these algorithms. Thus, it is adopted in our system.

3. A new two-ray channel estimation algorithm was developed for frequency selective fading. For the slow fading channel, three pilot symbols are inserted every k_t data symbols to estimate the two-ray channel state information. Two equivalent bandwidth modulation schemes (uncoded QPSK and coded TCM) are tested under both perfect and pilot channel state information situations. From our simulation, we find that uncoded QPSK outperforms coded 8-PSK TCM under both perfect and pilot channel state information situations. This can be explained by the fact that 8-PSK TCM achieves its coding gain over uncoded QPSK under memoryless channels, especially the AWGN channel. Because of the effect of frequency-selective fading on adjacent bits, inner interleaving cannot be used, while such channels exhibit bursty errors during deep fades.

We also tested the performance of two different receivers designed for flat (one-ray) fading channels and two-ray channels under the two-ray frequency-selective channel. Results show that when the two ray signal energy ratio is larger than 20 dB, the one-ray receiver performs better than the two-ray receiver.

4. We have proposed, implemented and evaluated a pyramid vector quantization (PVQ), three-dimensional (3-D) subband codec with a comparison to hybrid coding at low bit rates. The 3-D subband source coding eliminates the need for forward error correction and interleaving which is required by the hybrid H.261 and H.263 source coding for mobile satellite channels. The 3-D subband coding scheme also minimizes the temporal error propagation. The tradeoff is that the 3-D scheme achieves around 10 times less compression ratio than H.263.

5.2 Suggestions for Further Research

1. In this thesis, the pilot symbol aided channel estimation scheme is used to track both frequency-selective and frequency-nonselctive fading channel changes. This algorithm is not adequate for tracking the channel during a deep fade. A diversity combining technique for combatting a deep fade could be used in conjunction with the mentioned pilot symbol aided channel estimation techniques.
2. The bit error rate performance is evaluated by Monte-Carlo simulation. More work is needed in performing an error analysis of the complete system.
3. We show the error patterns of video through the fading channel. Error concealment techniques could be designed to correct video distortion and lower the channel SNR requirements.
4. Future issues in subband coding include designing several different fixed bit-rate PVQ adaptive bit allocation tables to account for different subband variance

distributions. Another issue involves incorporating motion compensation to improve video compression performance, while maintaining low computational complexity.

Bibliography

- [1] E.H. Adelson, E. Simoncelli, and R. Hingorani, "Orthogonal Pyramid Transforms for Image Coding," in *Proc. SPIE*, (Cambridge, MA), Oct. 1987, pp. 50-58.
- [2] A. Akansu and R. Haddad, *Multiresolution Signal Decomposition*, Academic Press, 1992.
- [3] Yaakov Bar-Shalom and Thomas E. Fortmann, *Tracking and Data Association*, Academic Press, Inc., 1988.
- [4] Yaakov Bar-Shalom and Xiao-Rong Li, *Estimation and Tracking: Principles, Techniques, and Software*, Artech House, Inc., 1993.
- [5] Bello P.A., "Characterization of randomly time-variant linear channels", *IEEE Trans. Commun. Systems*, CS-11, pp. 360-393, 1963.
- [6] Ezio Biglieri, Dariush Divsalar, Peter J. McLane and Marvin K. Simon, *Introduction to Trellis-Coded Modulation with Applications*, Macmillan Publishing Company, 1991.
- [7] B. Vucetic, "Bandwidth Efficient Concatenated Coding Schemes for Fading Channels," *IEEE Trans. Commun.*, Vol. 41, pp.51-61, Jan. 1993.
- [8] J. K. Cavers, "An analysis of Pilot Symbol Assisted Modulation for Rayleigh Fading Channels," *IEEE Trans. Veh. Technol.*, Vol.40, No.4, pp.687-693, Nov. 1991.

- [9] CCITT Recommendation H.261, RM8.
- [10] C. Tellambura, Q. Wang, and V. K. Bhargava, "Performance of Trellis Coded Modulation Schemes on Shadowed Mobile Satellite Communication Channels," *IEEE Trans. Veh. Technol.*, Vol. 43, pp.129-139, Feb. 1994.
- [11] Wai Ping Chou, *16-State Truncated State Estimator for $\pi/4$ -DQPSK Transmission on a Two Beam Fading Channel with Short Inter-Beam Delay*, M.Sc. Thesis, Queen's University, 1993.
- [12] Thomas M. Cover and Joy A. Thomas, *Elements of Information Theory*, John Wiley & Sons, Inc., 1991.
- [13] Q.Dai and E.Shwedyk, "Detection of bandlimited signals over frequency selective Rayleigh fading channels", *IEEE Transactions on Communications*, Vol. 42, No. 3, pp. 941-950, March 1994.
- [14] T.R. Fisher, "A Pyramid Vector Quantizer," *IEEE Transaction on Information Theory*, IT-32:568-583, July 1986.
- [15] T.R. Fisher, "Geometric Source Coding and Vector Quantization," *IEEE Transaction on Information Theory*, IT-35:137-145, January 1989.
- [16] Allen Gersho and Robert M. Gray, *Vector Quantization and Signal Compression*, Kluwer Academic Publishers, 1991.
- [17] Jerrold A. Heller and Irwin Mark Jacobs, "Viterbi Decoding for Satellite and Space Communication", *IEEE Transactions on Communication Technology*, Vol. com-19, No. 5, pp. 835-848. Oct. 1971.
- [18] Irvine, G.T. and P.J. McLane, "Symbol-aided plus decision-directed reception for PSK/TCM modulation on shadowed mobile satellite fading channels," *IEEE Journal on Selected Areas in Communications*, Vol.10, No.8, 1992, pp.1289-1299.

- [19] W. Jakes, *Microwave Mobile Communications*, John Wiley and Sons, New York, 1974.
- [20] A.C.M. Lee and P.J.McLane, "Convolutionally interleaved PSK and DPSK trellis code for shadowed, fast fading mobile satellite communication channels," *IEEE Trans. Veh. Technol.*, Vol. 39, pp.37-47, June 1990.
- [21] William C.Y. Lee, *Mobile Communication Engineering*, McGraw-Hill, 1982.
- [22] Shu Lin and Daniel J. Costello, *Error Control Coding*, Prentice-Hall, Inc. Englewood Cliffs, New Jersey, 1983.
- [23] Ming Liou, "Overview of the px64 kbits/s Video Coding Standard," *Communications of the ACM*, Vol.34, No.4, pp. 59-63, April 1991.
- [24] Y. Liu and S.D. Blostein, "Identification of Frequency Non-selective Fading Channels Using Decision Feedback and Adaptive Linear Prediction," *IEEE Trans. Commun.*, Vol.43, No.2-4, pp. 1484-1492, April, 1995.
- [25] C. Loo, "A Statistical Model for a Land Mobile Satellite Link," *IEEE Trans. Veh. Technol.*, Vol. 34, pp. 122-127, Aug. 1985.
- [26] C. Loo *et al.*, "Measurements and Modelling of Land-mobile Satellite Signal Statics," in *1986 Vehicular Technology Conf.*, Vol.34, Dallas, TX, May 1986, pp. 262-267.
- [27] J.E. Mazo, "Exact Matched Filter Bound for 2-Beam Rayleigh Fading", *IEEE Trans. on Comm.*, Vol. 39, pp. 1027-1030, July 1991.
- [28] P.J.McLane, P.H.Wittke, P.K.M.Ho, and C.Loo, "PSK and DPSK trellis codes for fast fading, shadowed mobile satellite communication channels," *IEEE Trans. Commun.*, vol.36, pp. 1242-1246, Nov. 1988.
- [29] T. Meng *et al.*, "Portable Video-on-Demand in Wireless Communication," Proceedings of the IEEE, pp. 659-680, April, 1995.

- [30] Michael L. Moher and John H. Lodge, "TCMP - A Modulation and Coding Strategy for Rician Fading Channels," *IEEE Journal on Selected Areas in Communications*, Vol.7, No.9, Dec. 1989, pp.1347-1355.
- [31] S. Y. Mui and J. W. Modestino, "Performance of DPSK with convolutional encoding on time-varying fading channels," *IEEE Trans. Commun.*, Vol. 25, pp. 1075-1083, Oct. 1977.
- [32] A.N. Netravali and B.G. Haskell, *Digital Pictures: Applications of Communications Theory*. New York: Plenum, 1988.
- [33] J. Ohm, "Three-Dimensional Subband Coding with Motion Compensation," *IEEE Trans. Image Processing*, Vol. 3, No. 5, pp. 559-571, Sept. 1994.
- [34] John G. Proakis, *Digital Communications*. McGraw-Hill, New York, 2nd edition, 1989.
- [35] Abha Singh and V. Michael Bove, "Multidimensional Quantizers for Scalable Video Compression", *IEEE Journal on Selected Areas in Communications*, Vol. 11, No. 1, pp. 36-45, Jan. 1993.
- [36] Robert Stedman, Hamid Gharavi, Lajos Hanzo and Raymond Steele, "Transmission of Subband-Coded Images via Mobile Channels", *IEEE Transactions on Circuits and Systems for Video Technology*, Vol. 3, No. 1, pp. 15-26, Feb. 1993.
- [37] Seymour Stein, "Fading Channel Issues in System Engineering," *IEEE Journal on Selected Areas in Communications*, Vol. 5, No. 2, pp.68-89, February 1987.
- [38] TMN H.263 Codec, Digital Video Coding at Telenor Research, <http://www.nta.no/brukere/DVC/>
- [39] G. Ungerboeck, "Channel Coding with Multilevel/ phase signals", *IEEE Trans. Inform. Theory*, Vol. IT-28, pp. 55-67, Jan.1982.

- [40] G. Ungerboeck, "Trellis-coded Modulation with Redundant Signal Sets. Part I: Introduction; Part II: State of the Art," *IEEE Commun. Mag.*, Vol. 25, No. 2, pp. 5-21, Feb. 1987.
- [41] P.P. Vaidyanathan, *Multirate Systems and Filter Banks*, PTR Prentice Hall, Englewood Cliffs, New Jersey, 1993.
- [42] Lee-Fang Wei, "Coded Modulation with Unequal Error Protection", *IEEE Transactions on Communications*, Vol. 41, No. 10, pp. 1439-1449, Oct. 1993.
- [43] X. Wang, J.Y. Liu, and S.D. Blostein, "Video Image Transmission via Mobile Satellite Channels," *Proc. ICC*, pp. 352-356, June 1995.
- [44] Widrow, B. and M.E.Hoff, Jr., "Adaptive switching circuits," *IRE WESCON Conv. Rec.*, Part 4, pp.96-104, 1960.
- [45] Widrow, B., J.M. McCool and M. Ball, "The complex LMS algorithm", *Proceeding of IEEE*, Vol. 63, pp.719-720, 1975.
- [46] *Wireless personal communications*. Boston: Kluwer Academic Publishers, 1993.
- [47] John W. Woods, *Subband Image Coding*, Kluwer Academic Publishers, 1991.
- [48] William W. Wu, Edward F. Miller, Wilbur L. Pritchard and Raymond L. Pickholtz, "Mobile Satellite Communications", *Proceedings of the IEEE*, Vol. 82, No. 9, pp. 1431-1447. Sept. 1994.
- [49] D. Taubman and A. Zakhor, "Multirate 3-D Subband Coding of Video," *IEEE Trans. Image Processing*, Vol. 3, No. 5, pp. 572-588, Sept. 1994.

Vita

Wendy Xiaohong Wang

EDUCATION

M.Sc. (1993–95), Electrical & Computer Engineering, Queen's University

B.Sc. (1984–88), Electrical Engineering, Shanghai Jiao Tong University

EXPERIENCE

Research Assistant (1993-1995), Electrical & Computer Engineering, Queen's University

Electrical Engineering Instructor (1988-1993), Shanghai Volkswagen Automotive Company Ltd

PUBLICATIONS

Xiaohong Wang, Yong Liu and Steven Blostein, "Video Image Transmission Via Mobile Satellite Channels", *Proc. of IEEE International Conference on Communications*, pp.352-356, June 1995.

Xiaohong Wang and Steven Blostein, "Three Dimensional Subband Video Transmission Through Mobile Satellite Channels", *Proc. of IEEE International Conference on Image Processing*, Oct. 1995. (in press)

Xiaohong Wang and Steven Blostein, "Very Low Bit Rate Video Image Transmission Through Mobile Satellite Channels", *1995 TRIO and ITRC Retreat*.